

**NASA CR 152053
(ASI-TR-76-28)**

N78-13007

(NASA-CR-152053) AERODYNAMIC INTERFERENCE
EFFECTS ON TILTING PROPROPOTOR AIRCRAFT Final
Technical Report, Oct. 1975 - May 1977

(Aerospace Systems, Inc., Burlington, Mass.)

Unclass

141 p HC A07/MF A01

CSCL C1A G3/02 55029

AERODYNAMIC INTERFERENCE EFFECTS ON TILTING PROPROPOTOR AIRCRAFT

FINAL TECHNICAL REPORT

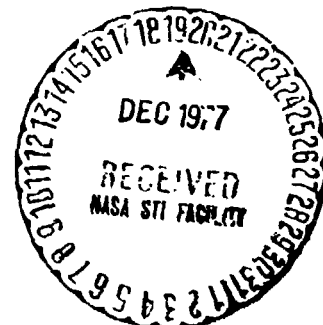
**Paul Soohoo
Luigi Morino
Richard B. Noll
Norman D. Ham**

June 1977

Contract No. NAS 2-8671

for

**Ames Research Center
National Aeronautics and Space Administration
Moffett Field, California 94035**



ASI

AEROSPAC SYSTEMS, INC.

ONE VINE BROOK PARK • BURLINGTON, MASS. 01803 USA

TELEPHONE (617) 272-7517

NASA CR 152053
(ASI-TR-76-28)

AERODYNAMIC INTERFERENCE EFFECTS
ON
TILTING PROPROTOR AIRCRAFT
FINAL TECHNICAL REPORT

by

Paul Soohoo
Luigi Morino
Richard B. Noll
Norman D. Ham

Approved John Zvara
John Zvara
Technical Director

Prepared under
Contract No. NAS 2-8671

for

National Aeronautics and Space Administration
Ames Research Center
Moffett Field, California 94035

June 1977

FOREWORD

This report was prepared by Aerospace Systems, Inc. (ASI), Burlington, Massachusetts, for the National Aeronautics and Space Administration (NASA) under Contract No. NAS 2-8671. The report documents the results of research performed during the period October 1975 to May 1977. The study was sponsored by the Ames Research Center, Moffett Field, California, with Dr. Wayne Johnson serving as Technical Monitor.

The effort was directed by Mr. John Zvara, President and Technical Director of ASI. Mr. Richard B. Noll, Vice President of ASI, served as Project Engineer. Mr. Paul Soohoo of ASI and Dr. Luigi Morino, Director of the Computational Continuum-Mechanics Program at Boston University, were Principal Investigators. Dr. Norman D. Ham, Director of the V/STOL Technology Laboratory at MIT, contributed to the study as Principal Consultant.

SUMMARY

An investigation has been performed to demonstrate the feasibility of the Green's function method to study tilting proprotor aircraft aerodynamics with particular application to the problem of the mutual interference of the wing-fuselage-tail-rotor wake configuration. While the formulation is valid for fully unsteady rotor aerodynamics, this report is mainly concerned with steady-state aerodynamics, which is achieved by replacing the rotor with the actuator disk approximation. The use of an actuator disk analysis introduced a mathematical singularity into the formulation; this problem has been studied and resolved.

The pressure distribution, lift, and pitching moment were obtained for an XV-15 wing-fuselage-tail rotor configuration at various flight conditions. For the flight configurations explored in this investigation, the effects of the rotor wake interference on the XV-15 tilt rotor aircraft yielded a reduction in the total lift and an increase in the nose-down pitching moment.

The present method has potential application in the design of helicopters because it provides an analytical capability that is simple to apply and can be used to investigate fuselage-tail rotor wake interference as well as to explore other rotor design problem areas. The numerical results obtained are of a preliminary nature and were used to identify requirements for further theoretical and experimental research into wing-tail-rotor aerodynamic interference effects on tilting proprotor aircraft.

PRECEDING PAGE BLANK NOT FILLED

PRECEDING PAGE BLANK NOT FILLED

TABLE OF CONTENTS

<u>Section</u>	<u>Page</u>
1 INTRODUCTION	1
2 TILTING PROPROTOR AIRCRAFT BACKGROUND	3
2.1 Aircraft Description	3
2.2 Anticipated Problems Due to Aerodynamic Interference ..	9
3 STATE OF THE ART	13
3.1 Wing-Body Aerodynamic Interference	13
3.2 Tilt Rotor Aircraft Aerodynamic Interference	14
4 APPROACH TO THE PROBLEM	19
4.1 Program SUSSA ACTS	19
4.2 Modifications to Program SUSSA ACTS	20
4.2.1 Actuator Disk	20
4.2.2 Tilt Rotor Aircraft Preprocessor	21
4.2.3 Rotor/Aircraft Wake Geometry	22
5 INCOMPRESSIBLE POTENTIAL AERODYNAMICS FOR WING- FUSELAGE-TAIL-ROTOR WAKE INTERFERENCE	29
5.1 Incompressible Inviscid Flows	29
5.2 Differential Formulation for Incompressible Potential Flows	31
5.3 Perturbation Potential	33
5.4 Green's Formula for Laplace's Equation	34
5.5 Green's Theorem for Incompressible Potential Aerodynamics	37
5.6 Conditions at Infinity	41
6 INCOMPRESSIBLE POTENTIAL AERODYNAMICS FOR COMPLETE CONFIGURATION WITH ACTUATOR DISK	43
6.1 Actuator Disk	43
6.2 Actuator Disk Boundary Conditions	45
6.3 Formulation for Complete Configuration	50

TABLE OF CONTENTS (Continued)

<u>Section</u>		<u>Page</u>
7	NUMERICAL FORMULATION	53
7.1	Approximate Algebraic System	53
7.2	Hyperboloidal Element	55
8	DETERMINATION OF FLIGHT CONDITIONS	59
8.1	Approximate Analysis of the Thrust and Flapping Motion of Rotors with Large Inflow	60
8.2	Selection of Flight Cases for Analysis Including Estimated Values of Collective Pitch and Rotor Incidence for Trim	64
9	RESULTS	73
9.1	Case with No Interference	73
9.1.1	Convergence	73
9.1.2	Lift and Pitching Moment	75
9.2	Interference Effects	76
10	CONCLUSIONS AND RECOMMENDATIONS	95
10.1	Conclusions	95
10.2	Recommendations for Future Research	96
-	REFERENCES	99

Appendices

A	AERODYNAMIC POTENTIAL PROGRAM SUSSA ACTS	A-1
B	INTEGRAL EQUATION FOR ACTUATOR DISK	B-1
B.1	Integral Representation for Actuator Disk	B-1
B.2	Actuator Disk with $\Delta \varphi_B = 0$	B-2
B.3	Actuator Disk with $\Delta \varphi_B \neq 0$	B-6
C	EVALUATION OF THRUST ON THE ROTOR	C-1

LIST OF ILLUSTRATIONS

<u>Figure</u>		<u>Page</u>
1	XV-15 Tilt Rotor Research Aircraft	4
2	Rotor Blade Characteristics for XV-15	8
3	Flaperon Deflection versus Flap Position	9
4	Rotor/Airframe Interference in Forward Flight	11
5	Rotor/Horizontal Stabilizer Wake Effects in Forward Flight	12
6	Two-Vortex Model	23
7	Vortex Cylinder Model	26
8	Geometry for Green's Formula for V_i Internal to Σ	35
9	Geometry for Green's Theorem for Potential Aerodynamics of Incompressible Flows	38
10	Surface Σ_0 for Actuator Disk Analysis. The Surface Surrounds the Actuator Disk, the Central Vortex, and the Shed Tip Vortices	44
11	Boundary Conditions for the Actuator Disk. Σ_D is the Surface Surrounding the Actuator Disk	46
12	Hyperboloidal Element	56
13	Typical Blade Element at Radius, $0.75R$	60
14	Rotor rpm versus Airspeed	65
15	Rotor Attitude versus Airspeed	65
16	Rotor Thrust Coefficient versus Airspeed	66
17	Rotor Collective Pitch versus Airspeed	66
18	Geometry of a Tilt Rotor Aircraft	74
19	Potential Difference, $\Delta\phi$, Wing-Tail Combination, No Rotor, Airspeed = 80 kt, $\alpha = 4.5^\circ$	79
20	Pressure Distribution, Wing-Tail Combination, No Rotor, Airspeed = 80 kt, $\alpha = 4.5^\circ$, Chordwise Direction, Root Chord	81

LIST OF ILLUSTRATIONS (Continued)

Figure		Page
21	Lift Distribution, Wing-Tail Combination, No Rotor, Airspeed = 80 kt, $\alpha = 4.5^\circ$, Chordwise Direction, Root Chord	83
22	Potential Difference, $\Delta \phi$, Wing-Tail-Rotor Configuration, Airspeed = 80 kt, $\alpha = 4.5^\circ$, Nacelle Incidence = 90° , Angular Speed = 565 rpm	84
23	Pressure Distribution, Wing-Tail-Rotor Configuration, Airspeed = 80 kt, $\alpha = 4.5^\circ$, Nacelle Incidence = 90° , Angular Speed = 565 rpm, Chordwise Direction, Root Chord	86
24	Lift Distribution, Wing-Tail-Rotor Configuration, Airspeed = 80 kt, $\alpha = 4.5^\circ$, Nacelle Incidence = 90° , Angular Speed = 565 rpm, Chordwise Direction, Root Chord	88
25	Aerodynamic Coefficients as Function of Number of Elements, Wing-Tail Combination, No Rotor, Airspeed = 80 kt, $\alpha = 4.5^\circ$	89
26	Lift Coefficient on Actuator Disk as Function of Number of Elements, Angular Speed = 600 rpm, Mast Angle = 90°	90
27	Aerodynamic Coefficients as Function of Number of Elements, Wing-Tail-Rotor Configuration, Airspeed = 80 kt, $\alpha = 4.5^\circ$, Nacelle Incidence = 90° , Angular Speed = 565 rpm	91
28	Interference Effects for Conversion Mode, Wing-Tail-Rotor Configuration, Airspeed = 100 kt, Tail Incidence = -1.5° , Nacelle Incidence = 60° , Angular Speed = 565 rpm	92
A-1	Program SUSSA ACTS	A-2
B-1	Geometry for Green's Theorem for Actuator Disk	B-3
B-2	The Geometry for Axisymmetric Actuator Disk Problem	B-7
B-3	Actuator Disk Branch Wake Potential Geometry for Nontrivial Solution	B-9
B-4	Solid Angle	B-11
B-5	Variation of φ_B as Function of θ_1	B-12
C-1	Control Surfaces Σ_D and Σ_R for Momentum Theorem	C-2

ORIGINAL PAGE IS
OF POOR QUALITY

x

LIST OF TABLES

<u>Table</u>		<u>Page</u>
1	Dimensions and General Data for XV-15	5
2	Conversion Characteristics for XV-15	6
3	Dimensions of Movable Aerodynamic Surfaces for XV-15	6
4	Rotor Characteristics for XV-15	8
5	Trim Values of Rotor Attitude and Collective Pitch	71

SYMBOLS

a	blade lift curve slope
\bar{a}_1	base vector defined by Equation (103)
\bar{a}_2	base vector defined by Equation (104)
A, B, C	arbitrary constants
AR	aspect ratio
b	number of rotor blades
b_{hk}	source coefficient defined by Equation (93)
b_t	horizontal tail spar
b_w	wing span
c	blade chord
\bar{c}	mean aerodynamic chord
c_{hk}	doublet coefficient defined by Equation (92)
c_t	horizontal tail chord
c_w	wing chord
C_D	drag coefficient
C_L	$\frac{L}{qS}$; lift coefficient
C_m	pitching moment coefficient
C_{p_l}	coefficient of lower pressure distribution
C_{p_u}	coefficient of upper pressure distribution
C_T	rotor thrust coefficient defined by Equation (9)
C_X	component of thrust coefficient along flight path
C_Z	component of thrust coefficient perpendicular to flight path

ORIGINAL PAGE IS
OF POOR QUALITY

SYMBOLS (Continued)

D	drag force
E_*	domain function defined by Equation (60)
f, g	arbitrary scalar functions
h	rotor attitude
h/D	rotor height-to-diameter ratio
i	rotor incidence angle
$\bar{i}, \bar{j}, \bar{k}$	unit vectors along x, y, z directions, respectively
I_D	doublet integral defined by Equation (100)
I_S	source integral defined by Equation (101)
L	lift
\bar{n}	unit normal to surface Σ
n_B	direction normal to the surface of the blade
\bar{n}_B	unit normal to the blade
n_D	direction normal to the surface of the actuator disk
\bar{n}_D	unit normal to actuator disk
\bar{n}_o	outward normal to surface Σ
N_{elem}	total number of elements
p	pressure
$\bar{p}_0, \bar{p}_1, \bar{p}_2, \bar{p}_3$	parameters describing the geometry of hyperboloidal elements
$\bar{p}_{++}, \bar{p}_{+-}, \bar{p}_{-+}, \bar{p}_{--}$	corner points of hyperboloidal element (see Figure 12)
P	point on surface Σ
P_h	control point on surface Σ
P_k	dummy point on surface Σ

SYMBOLS (Continued)

P_w	point on the wake being convected with velocity \bar{V}_A
P_*	control point in the flow field
q	dynamic pressure
$r = P - P_* $	distance between control point and dummy point
r	radial position along blade element (see Section 8)
R	rotor radius
R_{Σ_2}	radius of spherical surface Σ_2 (see Figure 9)
s_B	direction tangential to the surface of the blade
\bar{s}_B	vector tangential to the surface of the blade
s_D	direction tangential to the surface of the actuator disk
\bar{s}_D	vector tangential to the surface of the actuator disk
S	area of wing
t	time
T	rotor thrust
U	resultant air velocity
U_p	resultant air velocity perpendicular to tip path plane
U_T	resultant air velocity tangent to tip path plane
U_∞	free stream velocity
v	rotor induced velocity (see Equation 106)
\bar{v}	perturbation velocity
v_H	rotor induced velocity on horizontal stabilizer, ft/sec
V	flight velocity

SYMBOLS (Continued)

\bar{V}	velocity vector
\bar{V}'	resultant flow velocity obtained with two-vortex model
V''	mean convection velocity obtained with vortex cylinder model
\bar{V}_A	average value of velocity
\bar{V}_B	velocity of the body
V_i	volume internal to the surface of the body Σ
V_x, V_y, V_z	component of the velocity vector in the x, y, z direction, respectively
w_{hk}	wake coefficient defined by Equation (94)
W	aircraft gross weight
W_h^B	wake coefficient obtained from the branch wake Σ_r'
x	axial coordinate
Δx	length of vortex cylinder generated during one revolution of the rotor, and measured along the axis of the cylinder
y	spanwise coordinate measured from mid-span
α	angle of attack
α_R	rotor attitude
β	blade inflow angle (see Figure 11)
β_o	blade coning angle
$\beta_l^{c_{HP}}$	blade longitudinal flapping angle with respect to hub plane
$\beta_l^{s_{HP}}$	blade lateral flapping angle with respect to hub plane
γ	angle of climb
Γ_o	mid-span value of elliptical circulation distribution

ORIGINAL PAGE IS
OF POOR QUALITY

SYMBOLS (Continued)

δ_{hk}	Kronecker delta = $\begin{cases} 1 & h = k \\ 0 & h \neq k \end{cases}$
δ_3	pitch flap coupling, degree
ϵ	radius of Σ_1 (see Figure 9)
θ	rotor angular position
$\theta_{0.75}$	blade collective pitch at three-quarter radius
θ_{1c}	blade lateral cyclic pitch
θ_{1cHP}	blade lateral cyclic pitch angle with respect to hub plane
θ_{1s}	blade longitudinal cyclic pitch
θ_{1sHP}	blade longitudinal cyclic pitch angle with respect to hub plane
$\theta_{0.75}$	blade pitch at three-quarter radius
λ	inflow ratio
μ	advance ratio
ξ, η	curvilinear coordinates for hyperboloidal element
ρ	air density
σ	solidity of rotor (Equation 109)
Σ	surface surrounding the body and the wake
Σ_B	surface of the body
Σ_D	surface of actuator disk
Σ_h	h^{th} quadrilateral element
Σ_k	k^{th} quadrilateral element
Σ_R	surface of the rotor blades

ORIGINAL PAGE IS
OF POOR QUALITY

SYMBOLS (Concluded)

Σ_W	surface of the wake
Σ_0	surface surrounding the body and rotor blades (Figure 9)
Σ_1	spherical surface of radius ϵ and center P_*
Σ_2	spherical surface of radius R_{Σ_2} and center P_*
Σ_k'	strip of wake element (bounded by two streamlines) emanating from element Σ_k
Σ_R'	wakes of the rotor blades
Σ_T'	surface of the tail wake
Σ_W'	surface of the wing wake
τ	thickness ratio
φ	perturbation potential
φ_{TE}	potential at trailing edge
φ_*	perturbation potential at control point P_*
$\Delta\varphi_B$	value of $\Delta\varphi$ on the branch wake of actuator disk
ϕ	blade inflow angle
Φ	potential = $U_\infty x + \varphi$
ψ	blade azimuth angle
Ψ	downwash on actuator disk
Ω	rotor rotational speed
$\bar{\Omega}$	angular velocity of the rotor
$\bar{\nabla}$	del operator = $\bar{i} \frac{\partial}{\partial x} + \bar{j} \frac{\partial}{\partial y} + \bar{k} \frac{\partial}{\partial z}$

SECTION 1

INTRODUCTION

The XV-15 tilting proprotor (tilt rotor) aircraft is being developed under a joint NASA/Army program to provide flight research and technical data for the design of tilt rotor aircraft for military and civil applications (References 1 and 2). This tilting proprotor research aircraft is characterized by low disk-loading rotors (two 3-bladed, 25-ft diameter rotors for a gross weight of 13,000 lb) mounted at the wing tips, a forward-swept high wing, and twin vertical tails. The XV-15 aircraft offers the hover and low-speed capabilities of a helicopter and the high-speed cruise (300 knots) advantages of fixed-wing aircraft. The proprotors are positioned in a helicopter mode to take off vertically. As forward speed is developed, the rotors are tilted forward progressively (conversion mode) until the high speed cruise mode is achieved. In this aircraft mode, lift is provided by the wings, and the proprotors provide the propulsive thrust.

The large rotors located on the wing tips and tilted at different thrust angles introduce numerous dynamic considerations (e.g., References 3 to 6). In particular, the aerodynamic wake generated by the rotors can envelope the tail surface. Thus, the mutual interference of the rotor, wing, fuselage, tail, and their wakes is potentially of greater importance for this aircraft than for other configurations. Compared to helicopters, the aircraft has larger wing and tail surfaces; compared to propeller airplanes, it has much larger rotors which perform the same function as propellers. The effects of the aerodynamic interference on the stability and control characteristics of the aircraft are expected to be important. Of particular interest is the effect on longitudinal trim of the aircraft, especially through transition and conversion modes.

This report demonstrates the feasibility of a method to study aerodynamic interference effects on aircraft. In particular, the problem of the rotor wake interaction

effects for a tilting proprotor aircraft at various flight conditions is investigated. The results obtained are of a preliminary nature and are used to identify requirements for further theoretical and experimental research into wing-tail-rotor aerodynamic interference effects on tilting proprotor aircraft.

The report begins in Section 2 with a description of the tilt rotor aircraft and a review of problems anticipated because of aerodynamic interference. The state of the art in the prediction and analysis of aerodynamic interference is reviewed briefly in Section 3. The approach to the problem used in this study is discussed in Section 4, along with required modifications to a computer program used in calculating aerodynamic loads. Section 5 presents the potential aerodynamic theory for the mutual interference of a wing-fuselage-tail-rotor wake configuration. In Section 6, the potential aerodynamic theory is modified for the special case of an actuator disk model instead of a finite-blade rotor model. Section 7 gives the numerical formulation used to implement the aerodynamic theory of Sections 5 and 6 into a computer program. The determination of appropriate flight conditions to be used in the investigation is discussed in Section 8. Section 9 presents the computed results and discusses the implications of the calculations. Section 10 provides concluding remarks on the present study, and gives recommendations for future research based on the results of this study. A list of references supporting the various discussions is included, as well as appendices which provide supplementary information on the computer program used during the study and on the actuator disk equation.

SECTION 2

TILTING PROPROTOR AIRCRAFT BACKGROUND

2.1 AIRCRAFT DESCRIPTION

The tilting proprotor aircraft combines in one aircraft the hover efficiency of the helicopter and the high-speed efficiency of the fixed-wing aircraft (References 1, 7, and 8). The NASA/Army tilting proprotor research aircraft program sponsored preliminary design studies (References 9 and 10), which led to the development of a tilt-rotor research aircraft designated as the XV-15.

The XV-15 (Figure 1 and Table 1) is representative of those aircraft which employ the tilt rotor concept. The hover lift and cruise propulsive force is provided by low disk-loading rotors located at each wing tip. The rotor axes rotate from the vertical (or near vertical), the normal position for hover and helicopter flight, to the horizontal for airplane mode flight. Conversion characteristics are given in Table 2. Hover control is provided by rotor generated forces and moments, while airplane mode flight control is obtained primarily by the use of conventional aerodynamic control surfaces (Table 3).

A cross-shafting system connecting the rotors provides several benefits. This system precludes the complete loss of power to either rotor due to a single engine failure, permits power transfer for transient conditions, and provides rotational speed synchronization. Rotor-axis tilt synchronization is achieved by a separate interconnect shaft.

The aircraft is capable of high duration hover (approximately one hour at design gross weight), helicopter mode flight, versatility in performing conversion (steady-state flight is possible at any point in the broad transition corridor), and airplane mode level flight at speeds greater than 300 knots. The low disk-loading rotors

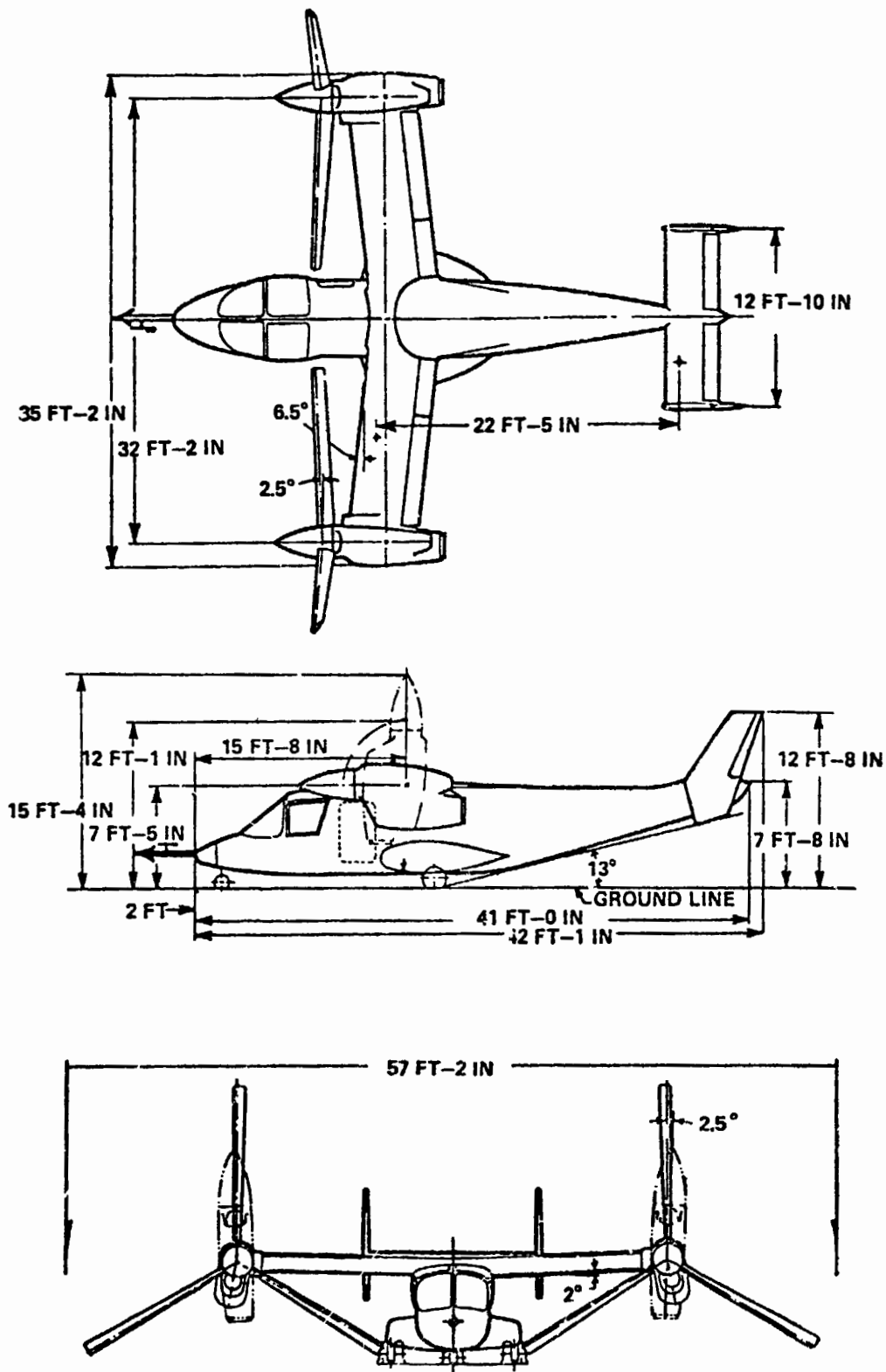


Figure 1. XV-15 Tilt Rotor Research Aircraft.

Table 1. Dimensions and General Data for XV-15.

Description	Wing	Horizontal Tail	Vertical Tail
Area, sq ft	169.0 ^a	50.25	50.5
Span, ft	32.17 ^a	12.83	7.68
Chord, ft	5.25	3.92	4.09/2.40 ^b
\bar{c} , ft ^c	5.25	3.92	3.72 ^d
Aspect ratio	6.12	3.27	2.33
Incidence, degree	3.0	0 to +6 ^e	---
Dihedral, degree	2.0	0	---
Sweep $\frac{c}{4}$, degree	-6.5	0	31.6 ^f
Section (NACA)	64A223 (Mod)	64A015	0009
Tail length, ft	---	22.4	23.2 ^d
a - between rotor centerlines at tilt axis; b - root/tip; c - mean aerodynamic chord (MAC); d - total; e - hinged at 33 percent chord; f - upper.			

can be operated in the autorotation state to reduce descent rate in the event of total power loss. Research operation at the design gross weight allows for a total useful load of over 2900 pounds. At intermediate rotor-axis tilt angles (between 60° and 75°), the aircraft can perform STOL operations at weights above the maximum VTOL gross weight.

The Lycoming LTC1K-4K (a modification of the T53-L-13B) engines and main transmissions are located in wing-tip nacelles to minimize the operational loads on the cross-shaft system and, with the rotors, tilt as a single unit. The use of the free turbine engines permits the reduction of rotor rotational speed for airplane mode flight to improve rotor performance and reduce cruise noise.

Table 2. Conversion Characteristics for XV-15.

Conversion axis:	
Wing chord location, percent	39.0
Forward sweep, degree	5.5
Dihedral, degree	3.0
Angle-to-mast axis, degree	95.5
Angle of outboard tilt-of-mast axis	
Helicopter mode, degree	2.5
Airplane mode, degree	0
Conversion range, degree	0 to 95
Rotor tip clearance (helicopter mode) to:	
Ground, ft	11.5
Wing upper surface, ft	4.8
Rotor tip clearance (airplane mode) to:	
Fuselage, ft	1.0
Wing leading edge, ft	0.47

Table 3. Dimensions of Movable Aerodynamic Surfaces for XV-15.

Description	Flap	Flaperon	Elevator	Rudder
Area aft hinge, sq ft	11.0 ^a	20.2 ^a	13.0	7.5 ^a
Span, ft	4.25 ^b	7.86 ^b	11.0	4.66
Chord aft hinge, percent	0.25	0.25	0.30	0.25
Surface deflection, degree	--- ^c	--- ^c	± 20	± 20
Control travel for total surface deflection, in	----	9.6	9.6	5.0
a - total both panels; b - one side, along hinge; c - see Figure 3.				

The XV-15 research aircraft utilizes 25-ft-diameter gimbal-mounted, stiff-inplane, three-bladed rotors, with elastomeric flapping restraints for increasing helicopter mode control power and damping. Rotor-blade characteristics are shown in Figure 2 and Table 4. Variable rotor-tip speed control is provided to enable research on noise, performance, and hover downwash. The nominal design tip speeds are tabulated as follows:

Condition	Tip Speed, ft/sec	rpm
Hover/Helicopter Mode	740	565
Cruise/Airplane Mode	600	458
Hover Test Overspeed	818	625
Design Limit	865	661

The forward-swept wings provide clearance for 12° of flap deflection which will accommodate gusts and maneuver excursions while operating in the airplane mode. Wing-pylon-rotor stability is accomplished by selecting a stiff wing and pylon-to-wing attachment and minimizing the distance of the rotor hub from the wing. Airplane mode wing-pylon-rotor stability is retained up to airspeeds of 370 knots even with a 20 percent reduction in wing and pylon stiffness.

For hover flight, the wing flaps and flaperons are deflected downward to reduce the wing download and increase hovering efficiency (Figure 3). Hover roll control is provided by differential rotor collective pitch, pitch control by cyclic pitch, and yaw control by differential cyclic pitch. Pilot controls in the helicopter mode are similar to that of a conventional helicopter. A collective stick provides power and collective pitch for height control and a control stick provides longitudinal and lateral control.

ORIGINAL PAGE IS
OF POOR QUALITY

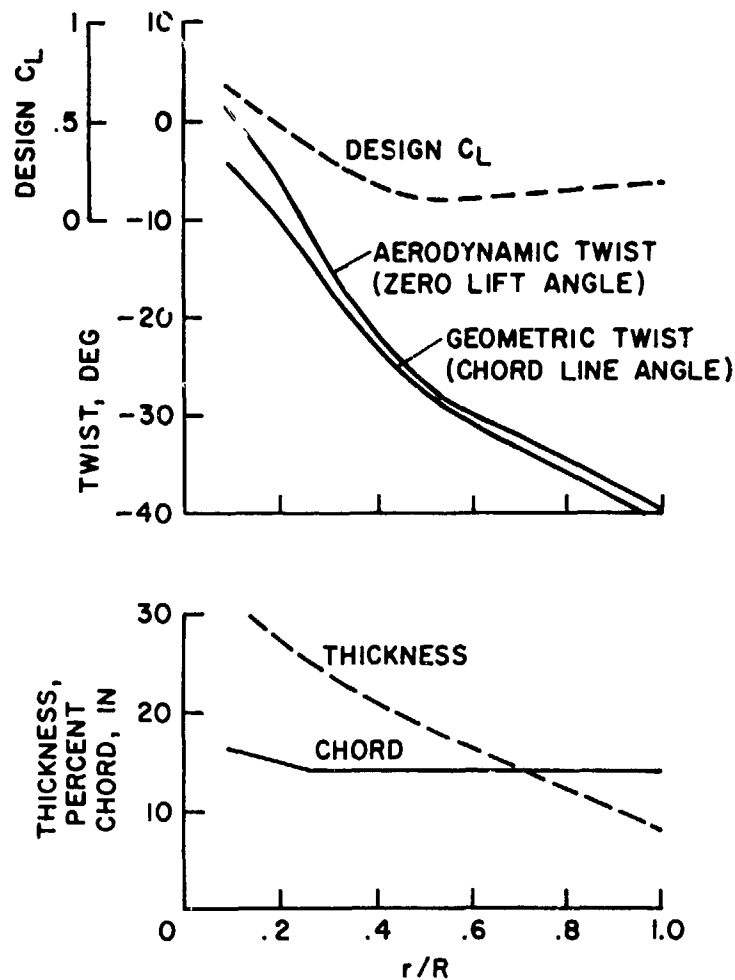


Figure 2. Rotor Blade Characteristics for XV-15.

Table 4. Rotor Characteristics for XV-15.

Number of blades per rotor	3
Diameter, ft	25.0
Disk area per rotor, sq ft	491
Blade chord (see Figure 2), in	14.0
Blade characteristics	See Figure 2
Solidity	0.089
Hub precone angle, degree	2.5
δ_3 , pitch flap coupling, degree	-15.0
Flapping design clearance, degree	± 12
Blade Lock number	3.83

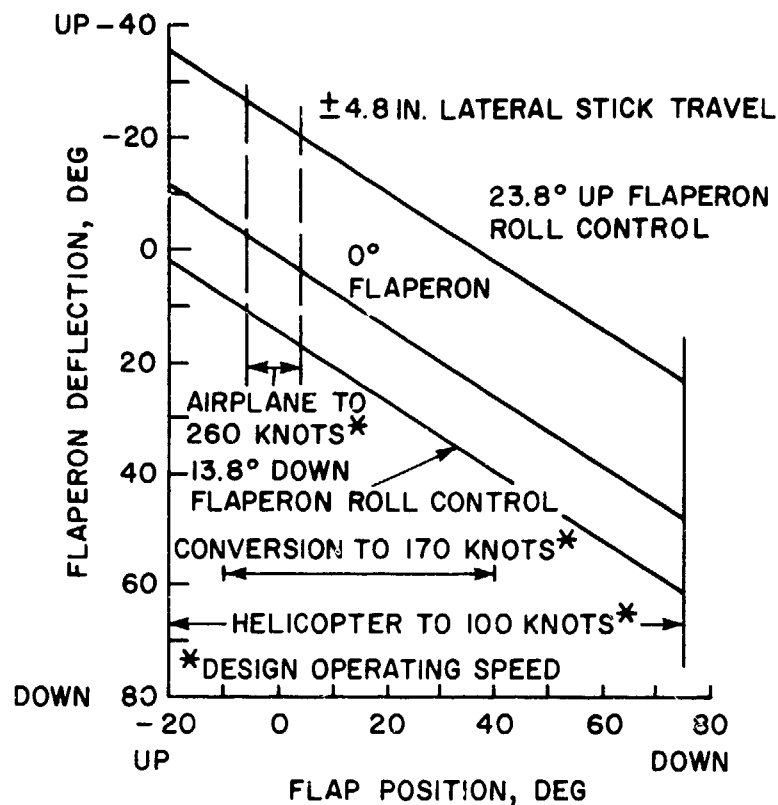


Figure 3. Flaperon Deflection versus Flap Position.

In the airplane mode, conventional airplane stick and rudder pedals are employed, while the collective stick/power lever continues to be used for power management. An H-tail configuration (two vertical stabilizers) has been selected to provide improved airplane directional stability around a zero yaw angle. Control authority for the power lever, blade pitch governor, cyclic, differential cyclic, differential collective, and flap/flaperon relationship are phased with mast angle by mechanical mixing linkages.

2.2 ANTICIPATED PROBLEMS DUE TO AERODYNAMIC INTERFERENCE

The tilting proprotor is a VTOL aircraft with laterally displaced tilting rotors at the tips of small wings, and a conventional tailplane mounted at the rear of

the fuselage for stability and control in translational flight (see Figure 1). The mutual interference of the rotor, wings, fuselage, and tail is likely to have important effects on the stability and control characteristics of this aircraft, including the longitudinal trim during transition and conversion, and the lateral trim in a sideslip or crosswind.

In a previous aircraft of this type, the Bell XV-3, a nose-down pitching tendency was caused by the rotor wake inboard tip vortices passing near the horizontal stabilizer. At low airspeeds, the tip vortices passed below the horizontal stabilizer and induced an increase in the angle of attack. The resulting lift required a small aft stick displacement which reduced the stick displacement gradient in the forward speed range from hover to 40 knots.

Tilt rotor wake effects on the wing and horizontal stabilizer have been measured during a recent one-tenth scale powered-model wind-tunnel test (Reference 11). From this test it was possible to establish these effects during low-speed transition and conversion flight. Wind-tunnel data showing the percent wing lift as a function of airspeed and mast angle are given in Figure 4. Comparison with rotors-off tests indicated that above 40 knots, wing lift is not influenced by the rotor wake.

The tilt rotor wake effects on the horizontal stabilizer were determined from the data summarized in Figure 5. As shown, an upwash exists during low-speed flight. This was found to have a considerable effect on longitudinal trim.

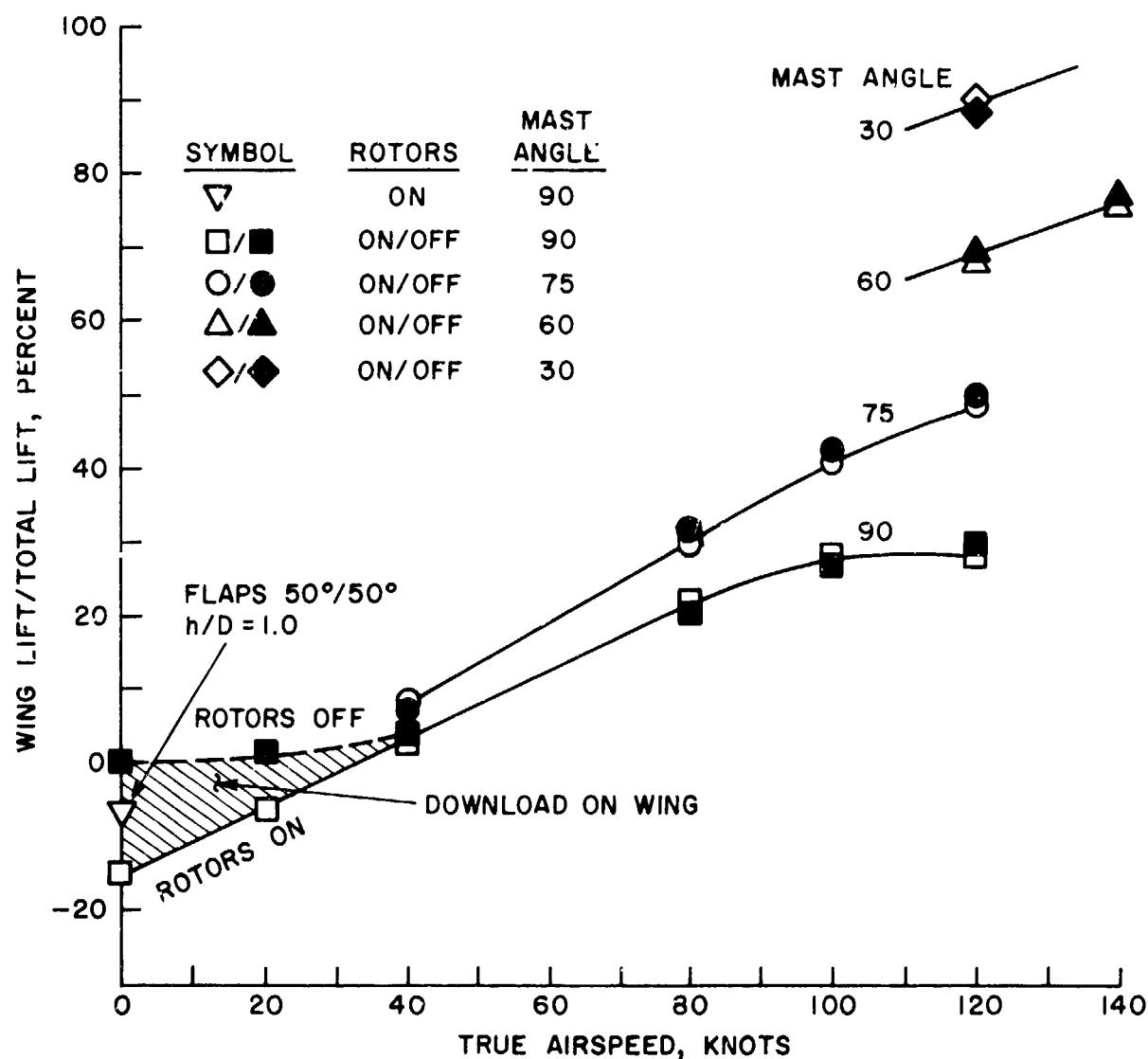


Figure 4. Rotor/Airframe Interference in Forward Flight (Reference 11).

ORIGINAL PAGE IS
OF POOR QUALITY

ORIGINAL PAGE IS
OF POOR QUALITY

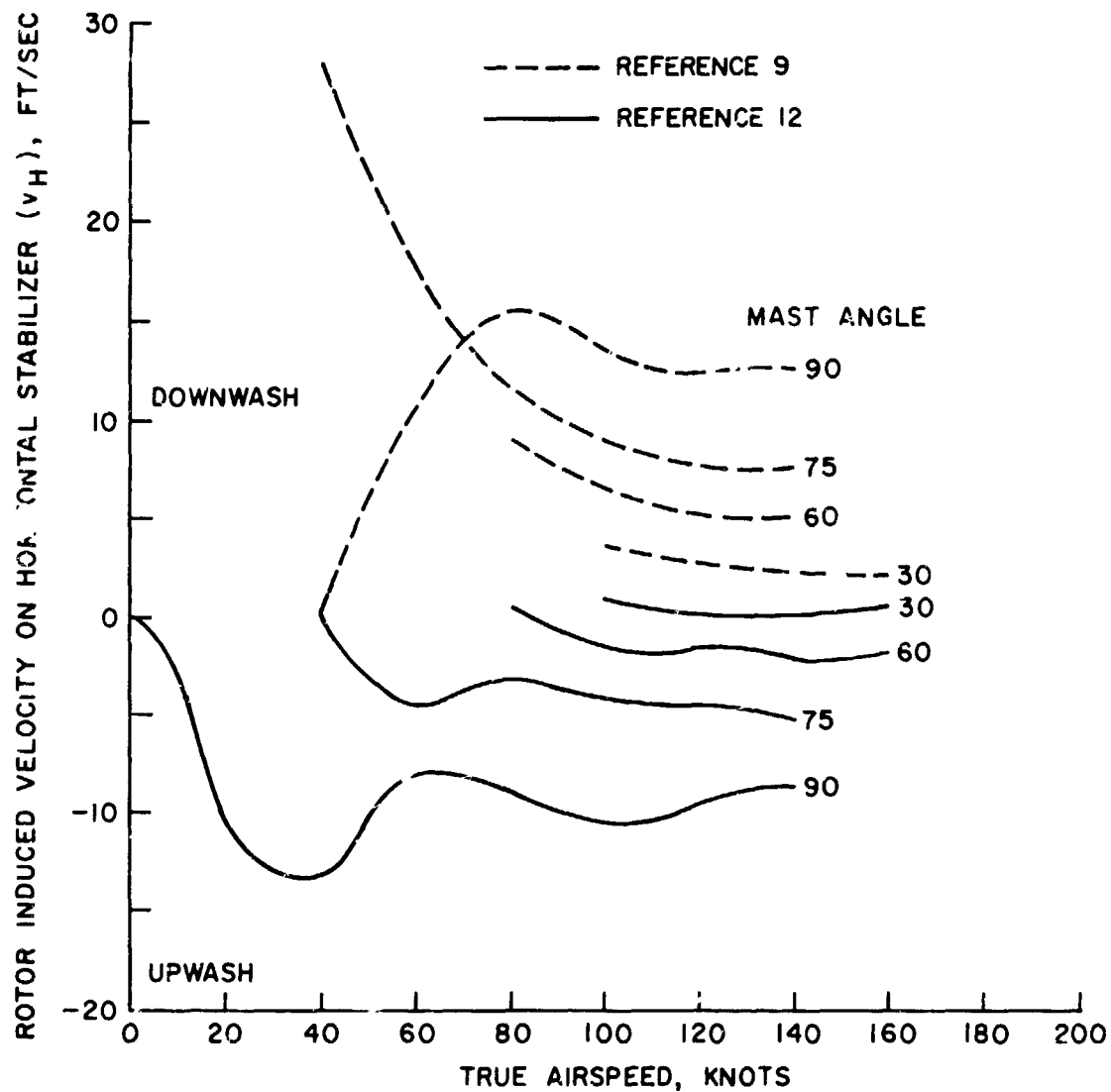


Figure 5. Rotor/Horizontal Stabilizer Wake Effects in Forward Flight (Reference 11).

SECTION 3

STATE OF THE ART

3.1 WING-BODY AERODYNAMIC INTERFERENCE

The classical approach for evaluating the aerodynamic pressure on interfering wings and tails is the lifting surface method (References 13 and 14). Calculations have been normally limited to wings or other lifting surfaces separately, except for a limited number of cases in which the vehicle could be considered as a slender body. However, interaction of the flowfields of wings and the fuselage results in interference effects (Reference 15) which cannot be adequately accounted for when examining the lifting surface and the body separately. The advent of modern high-speed computers has prompted the development of a series of new methods, generally called finite element methods. These methods offer both flexibility and efficiency and can be applied to complex configurations. All the methods are based on potential aerodynamics and consider various distributions of sources, doublets, vortices, pressure panels, etc., on and/or inside the surface of the aircraft.

An early work on the flow field around three-dimensional bodies (Reference 16) uses constant strength source-elements to solve the problem of steady subsonic flow around nonlifting bodies. This method has been extended to lifting bodies (References 17 through 19) by including doublet and vortex panels. Woodward's method (Reference 20) is a different approach which uses lifting surface elements for the representation of the body. For oscillatory subsonic aerodynamics, extensions of the doublet-lattice method (Reference 21) are obtained by either placing unsteady lifting surface elements on the surface of the body or by using the method of images combined with slender body theory (Reference 22). In the supersonic range, complex configurations are analyzed in References 20, 23 and 24. Recently, Woodward's method (Reference 20) has been

extended to provide a unified method for both subsonic and supersonic steady flow (Reference 25). In the wing-body-tail interference methods mentioned above, none is sufficiently general to analyze the interference of complex aircraft configurations in the presence of a rotor, since there exists no frame of reference with respect to which all the surfaces (body and rotor) are fixed.

A general method for steady and unsteady subsonic and supersonic aerodynamics around complex configurations (where the surface is allowed to move with respect to the frame of reference) has recently been developed by Dr. Luigi Morino. Morino's technique (References 26 and 27) is based upon the Green function method for the equation of the aerodynamic potential. The potential is expressed in terms of source distributions with known intensity (obtained from the boundary conditions) and doublet distributions with intensity equal to the unknown value of the potential on the surface. The integral equation is obtained by imposing the continuity of the potential along the normal to the surface; it may be noted that the boundary conditions are automatically satisfied. The application of Morino's method to finite-thickness wings is given in Reference 28, and the general theory for subsonic flow is reviewed in Reference 29. This method is readily applied to supersonic flow and is the only known method for analyzing unsteady supersonic flow around non-zero thickness configurations (Reference 30).

3.2 TILT ROTOR AIRCRAFT AERODYNAMIC INTERFERENCE

There is relatively little information available on aerodynamic interference effects in tilt rotor aircraft. References 31, 32, and 33 describe the results of tests of a powered wind tunnel model. Aerodynamic interference in forward flight was investigated by the observation of flow in the vicinity of the wing and empennage and the measurement

of the effect of interference on the empennage. Smoke injected upstream of the left-hand rotor showed the nature of the rotor-wing aerodynamic interference. Tests of a 1/10-scale model had previously shown that the wing download in hover changes to an upload in forward flight. The wing begins to contribute lift at an airspeed of 35 knots, whereas linearized wake theory would predict the wing to be immersed in the rotor wake at that low an airspeed. Observation of the flow showed that at speeds as low as 20 knots the rotor induced a strong upwash at the wing leading edge and that the rotor wake was completely off the wing at speeds over 30 knots. The nonuniform induced velocity of the rotor appears responsible for the wake moving off the wing at low airspeeds.

As a result of the powered model tests, the following were determined:

- Rotor wake interaction on the wing is nonlinear, varying from downwash on the outboard panels under the rotor to upwash on the inboard panels.
- Rotor wake on the horizontal stabilizer varies from an upwash during low-speed helicopter flight to a downwash during high-speed flight.
- The dynamic pressure at the empennage increases significantly during low-speed flight to nearly double that of free stream.
- The rotor wake across the horizontal stabilizer is nonlinear with sideslip and causes a pitch up with sideslip.
- Directional stability is influenced by the rotor wake interaction on the vertical stabilizer.

The flow patterns in the vicinity of the empennage were studied with the aid of smoke and photographs of a tufted grid. At 30 and 40 knots, the flow patterns became distinct and showed that the rolled-up rotor wake vortices were located directly above the horizontal stabilizer. At these speeds, the rotor wake has the characteristics of the wake of a low aspect ratio wing, with the net effect of an upload at the horizontal stabilizer.

ORIGINAL PAGE IS
OF POOR QUALITY

The tufted grid was not used at airspeeds higher than 40 knots. Smoke patterns at higher speeds showed that the rotor vortices moved downward and outward as speed increased. A net upwash over the span of the horizontal stabilizer was visible at airspeeds between 60 and 100 knots.

When the model was yawed at low speeds, the vortex cores shifted laterally with respect to the fuselage centerline. This shift has two effects on the empennage: (1) it reduces the strength of the rotor-wake-induced lift on the horizontal stabilizer, reducing the upload and producing a nose-up pitching moment; and (2) for yaw angles between 0 and 12 degrees, it reduces directional stability, due to the vortices moving laterally with respect to the vertical fins. At yaw angles greater than 12 degrees, the rotor wake increased the effectiveness of the vertical fins and thereby increased the directional stability over that of the basic airframe.

The interference between the rotor wake and the empennage was extracted from test data under the assumption that the aerodynamic interference is superimposed on the aerodynamic characteristics of the basic airframe. The downwash at the horizontal stabilizer was assumed to be caused by the wing and the rotors, with each acting separately, and with the total downwash being the sum of the respective downwashes. It is recognized that representing the effect of the rotor wake on the horizontal stabilizer in terms of a net upwash or downwash is a gross simplification, but this approach makes the problem tractable for application to the simulation. Representing the actual flow field in the vicinity of the empennage with a rigorous mathematical model is not presently feasible. Additional data on pressure distributions, local flow velocities, etc., would be required for the development of a more rigorous model.

Sideslip was found to reduce the magnitude of the upwash at the horizontal stabilizer. The downwash velocity was determined by assuming the total dynamic

pressure ratio to be equal to its value at zero sideslip. The reduction in upwash velocity causes a nose-up pitching moment when the aircraft is sideslipped.

The effect of rotor wake-airframe-ground aerodynamic interference on XV-15 handling qualities was also evaluated by observing model flying characteristics during semi-freeflight tests and from pilot comments during real time, pilot-in-the-loop, flight simulation.

In the wind tunnel semi-freeflight tests, the model could be trimmed at the lowest speed achievable in the tunnel (approximately 16 knots full scale). In the 16 to 35 knots range, control was difficult but manageable. Above 35 knots, the model became very easy to trim and control, and above 50 knots the model would maintain a trimmed condition "hands off." The model was also flown in sideward and rearward flight at speeds up to 35 knots. In both cases, roll control was difficult but manageable while pitch and yaw control were fairly easy (even in rearward flight). The model was noticeably more stable in descents, including autorotation, than in level flight and climbs. A brief investigation of controllability at nacelle incidence angles of 60° and 30° showed the model to be easy to control about all axes.

Real time, pilot-in-the-loop simulation was conducted on the NASA-Ames Flight Simulator for Advanced Aircraft. The mathematical model included the static instability in roll in hover, the effect of Induced Ground Effect (IGE) operation on rotor performance, the wing download variation with airspeed, and the effect of the rotor's wakes on the horizontal stabilizer and fin.

Although the effects of the interference were not evaluated directly, their influence was noted during the evaluation. Observed effects included:

- Increased workload to control roll when operating IGE. This effect of the static instability in roll was most apparent when taking off or landing.

- Stick position reversal, directional instability, and pitch coupling with sideslip during transition from hover to forward flight.
- Nose down pitching when increasing collective pitch at speeds between 20 and 60 knots.

All of these characteristics were similar to those observed in the scale model semi-freeflight tests.

Reference 34 describes aerodynamic interference effects during low-speed flight close to the ground. Both flying qualities data and flow visualization results are presented and their implication for the design of tilt rotor aircraft is described.

SECTION 4

APPROACH TO THE PROBLEM

Determination of the interference effects of the prop rotor wake on the aircraft stability characteristics requires an appropriate model of the wake in order to analyze the changes in aerodynamic force included on the control surfaces by the wake. Modeling of prop rotor wakes is based on the vortex theory of propellers developed by Goldstein (Reference 35). The vortex theory is a difficult boundary value problem: given a helical vortex sheet, find the vorticity distribution which causes the sheet to translate along its axis without distortion. The shape of the vortex wake is not known in advance. Moreover, the stretching of the pitch of the helix has as much influence on the induced flow as does the strength of the vorticity. The determination of the distortion of a vortex system, given the strength at the trailing edge of the blade, is a formidable task (References 36, 37, and 38). Moreover, the vortex strength depends upon the blade loading, which is also unknown. This problem was treated in Reference 36; however, the computer program developed there was too slow for practical purposes. The approach taken in Reference 38 was to proceed from an assumed vortex wake geometry, including contraction and acceleration effects.

4.1 PROGRAM SUSSA ACTS

The approach of Reference 38 is used in conjunction with the aerodynamic potential analysis technique developed by Morino (see Subsection 3.1). The technique is implemented in a computer program SUSSA ACTS (Steady and Unsteady Subsonic and Supersonic Aerodynamics for Aerospace Complex Transportation Systems), discussed in more detail in Appendix A. In this code the motion of the surface with respect to the frame of reference is assumed to consist of small oscillations with an arbitrary variation in time. The surface of the aircraft and its wake are divided into

small quadrilateral elements which are approximated by a hyperboloidal surface defined by four corner points. In this process, the continuity of the surface is maintained, although discontinuities in the slopes are introduced. The unknown is assumed to be constant within each element and, therefore, the integral equation reduces to a system of linear algebraic equations. The problems best suited to the program are steady and oscillatory subsonic and supersonic (linearized, attached, potential) flows around simple (such as simple wings) and complex configurations (such as combinations of wing, fuselage, tail, and control surfaces). It should be noted, however, that the general formulation includes fully unsteady flow. Therefore, the problem of interference of the aircraft (wing-fuselage-tail) with the rotor is a particular case of the general formulation presented in Reference 26.

4.2 MODIFICATIONS TO PROGRAM SUSSA ACTS

In order to be applicable to the aircraft-rotor interference, Program SUSSA ACTS requires modification in order to allow for the motion of the surface of the rotor, the tilt rotor aircraft geometry, and the wake geometry of the rotor. The approximate nature of the study on interference allows simplifying assumptions to be used for the aerodynamic analysis. It is assumed, therefore, that the number of blades in the rotor approaches infinity, yielding an actuator disk (see Subsection 6.1). For that case, the aerodynamic phenomena become steady, which simplifies the aerodynamic calculations. The modifications made to SUSSA ACTS are discussed briefly in the following sections.

4.2.1 ACTUATOR DISK

The present Program SUSSA ACTS does not automate the geometry of the tilting proprotor aircraft rotor assembly. Hence, a preprocessor, based on data provided, must be developed. Because of the nature of the present study, only the rotor will be

considered, and this is replaced by an actuator disk. The actuator disk is approximated with a thin ellipsoidal configuration. A standard finite element breakup is used to divide this surface into small quadrilateral aerodynamic panels. The preprocessor defines the nodal numbering and its location in the reference cartesian coordinate system.

On the actuator disk, the boundary condition (downwash) must be generated. The downwash ψ on the actuator disk is related to the rotor blade downwash by

$$\psi = (-U_{\infty} \bar{i} + \bar{\Omega} \times \bar{r}) \cdot \bar{n}_B / \cos \alpha + \frac{1}{2} C_T \Omega R \tan \alpha \quad (1)$$

where

α = angle of attack of the blade

\bar{n}_B = normal to the blade

$\bar{\Omega}$ = angular velocity of the rotor

U_{∞} = free stream velocity

C_T = rotor thrust coefficient

R = rotor radius

In obtaining this inflow, the components of the perturbation velocity tangent to the disk are assumed small. Details of this formulation are presented in Subsection 6.2.

4.2.2 TILT ROTOR AIRCRAFT PREPROCESSOR

The original preprocessor of SUSSA ACTS was designed for conventional wing-body-tail configurations. The wing was assumed to be located at mid fuselage, and the profile of the fuselage was assumed to be circular. In addition, the empennage was limited to only one vertical tail. Consequently, the geometry of the nose, fuselage, and empennage was modified appropriately to model the tilt rotor aircraft. These modifications affect the final nodal breakup of the tilt rotor aircraft.

ORIGINAL PAGE IS
OF POOR QUALITY

4.2.3 ROTOR/AIRCRAFT WAKE GEOMETRY

The surface of the wake emanating from the trailing edge of the wing and tail is assumed to be known. These wakes are treated as straight vortex lines from the trailing edges of the wings and tail and parallel to the direction of the flow. The Kutta condition is imposed at the trailing edges.

The wake of the actuator disk (rotor) is composed of infinite vortices emanating from the rim of the disk and one additional vortex emanating from the center of the disk. The control vortex represents the vorticity shed by the blade near the blade root. Details of the wake geometry of the actuator disk are given in Section 6.

- Two-Vortex Model (Helicopter and Initial Conversion Modes)

When the rotor has a small incidence angle with respect to the free stream (less than 30°), the wake rapidly rolls up into two concentrated vortices similar to the tip vortices of a monoplane wing (References 39 and 40).

On this basis, the wake model chosen for the helicopter mode of tilt rotor flight consists of two vortices trailed from the ends of the lateral diameter of the rotor disk, as shown in Figure 6(a). The strength of the vortices is obtained by assuming that the rotor behaves as an elliptical monoplane wing of span $2R$ (the Glauert hypothesis) whose lift, i.e., thrust, T , is given by

$$T = \rho V \int_{-R}^R \Gamma_o \left[1 - \left(\frac{y}{R} \right)^2 \right]^{1/2} dy \quad (2)$$

where

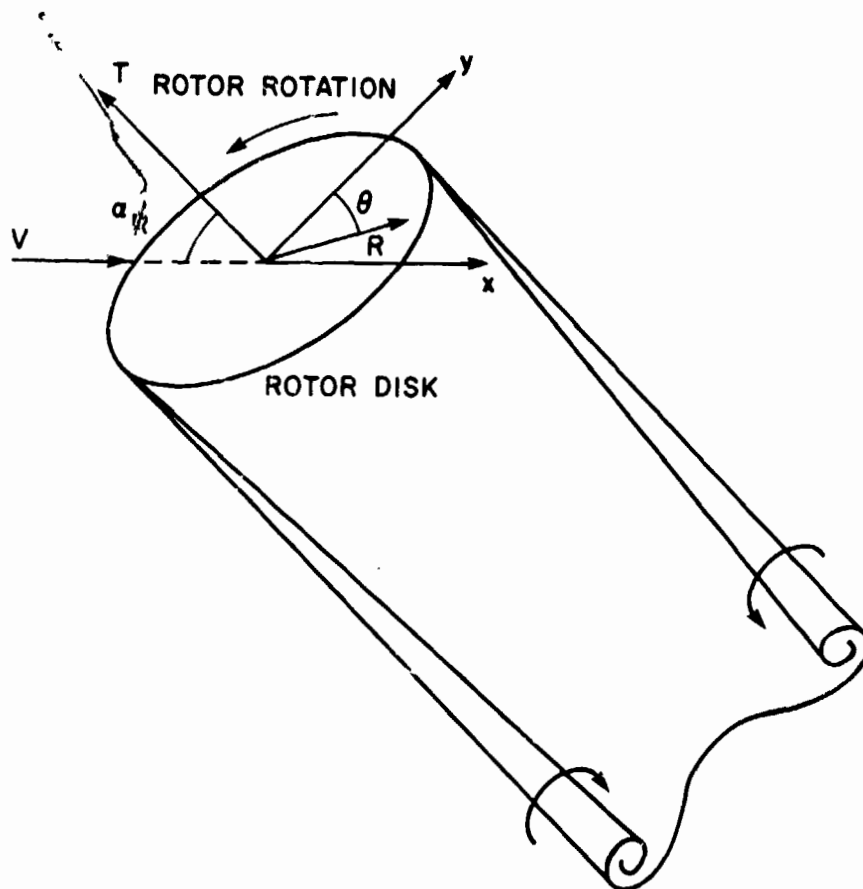
ρ = air density

V = flight velocity

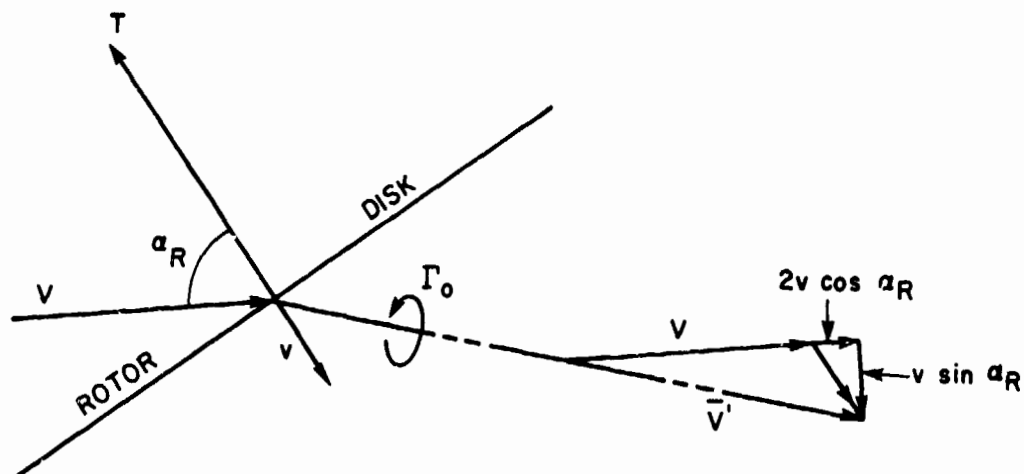
Γ_o = mid-span value of elliptical circulation distribution

y = spanwise coordinate measured from mid-span

R = rotor radius



(a) Wake Geometry



(b) Resultant Flow Velocity

Figure 6. Two-Vortex Model.

ORIGINAL PAGE IS
OF POOR QUALITY

Making the transformation $y = R \cos \theta$, $dy = -R \sin \theta d\theta$, the thrust becomes

$$\begin{aligned} T &= \rho V \Gamma_o R \int_0^\pi \sin^2 \theta d\theta \\ &= \frac{\pi}{2} \rho V \Gamma_o R \end{aligned} \quad (3)$$

Then the strength of the trailing vortices is given by the strength of the mid-span circulation, i.e.,

$$\Gamma_o = \frac{T}{\frac{\pi}{2} \rho V R} \quad (4)$$

In the far wake the two vortices are assumed to be convected downward at one-half the local downwash velocity, due to vortex sheet roll-up effects, as suggested by the results on page 45 of Reference 39. The resultant flow velocity is then given by the vector (see Figure 6(b))

$$\bar{V}' = [(V + 2v \cos \alpha_R), (v \sin \alpha_R)] \quad (5)$$

where, from Reference 41, page 185, the induced velocity, v , is

$$v = \frac{C_T \Omega R}{2 [\mu^2 + \lambda^2]^{1/2}} \quad (6)$$

and

$$\mu = \frac{V \sin \alpha_R}{\Omega R} \quad (7)$$

$$\lambda = \frac{V \cos \alpha_R + v}{\Omega R} \quad (8)$$

$$C_T = \frac{T}{\rho \pi R^2 (\Omega R)^2} \quad (9)$$

This model is assumed to be valid for the following conditions:

$V = 0$ to 130 knots

$\alpha_R = 60$ to 100 degrees

- Vortex Cylinder Model (Final Conversion and Cruise Modes)

When the rotor has a large incidence angle with respect to the free stream (more than 30°), the wake tends to assume the shape of a skewed cylinder of vorticity (Reference 39).

On this basis, the wake model chosen for the final conversion mode of tilt rotor flight consists of a skewed cylindrical surface of vorticity trailed from the edge of the rotor disk, as shown in Figure 7. The steady-state vorticity distribution is obtained from the expression derived in Reference 42 for the bound vortex strength Γ_o of one rotor blade:

$$\Gamma_o = \frac{2T}{\rho \Omega R^2 b} \quad (10)$$

where

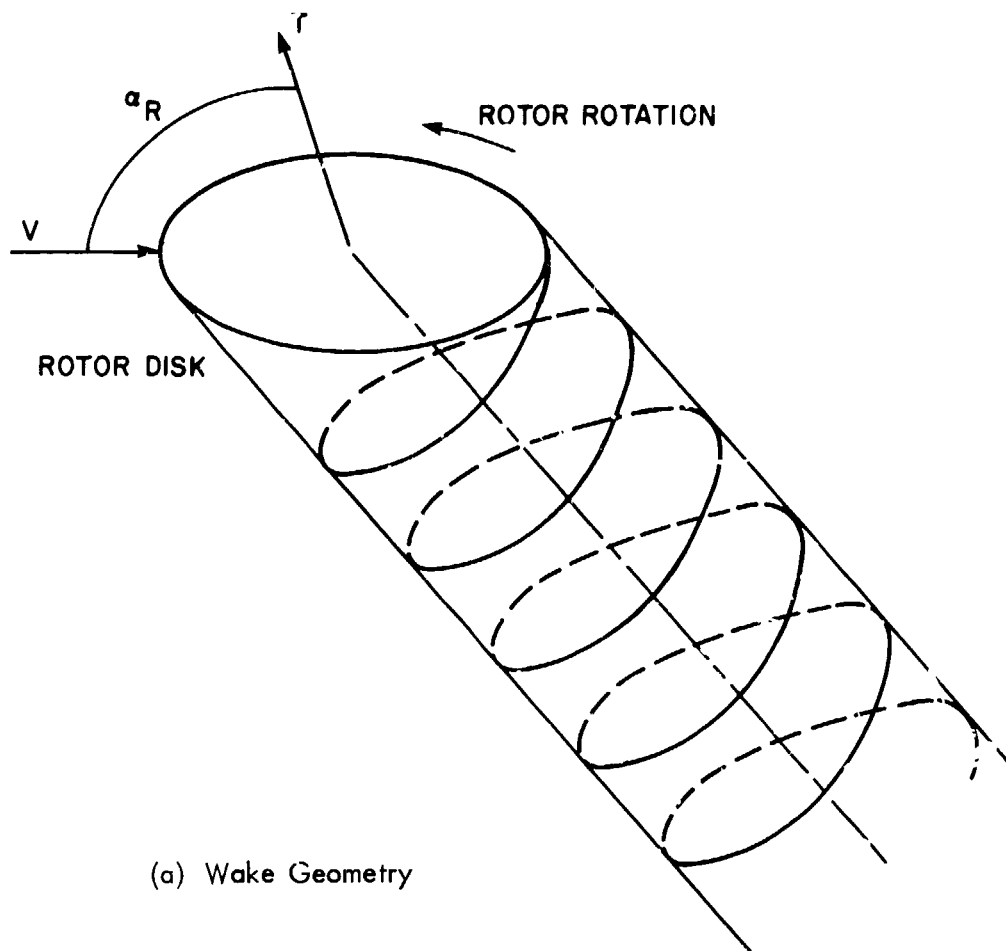
$\Omega =$ rotor rotational speed

$b =$ number of rotor blades

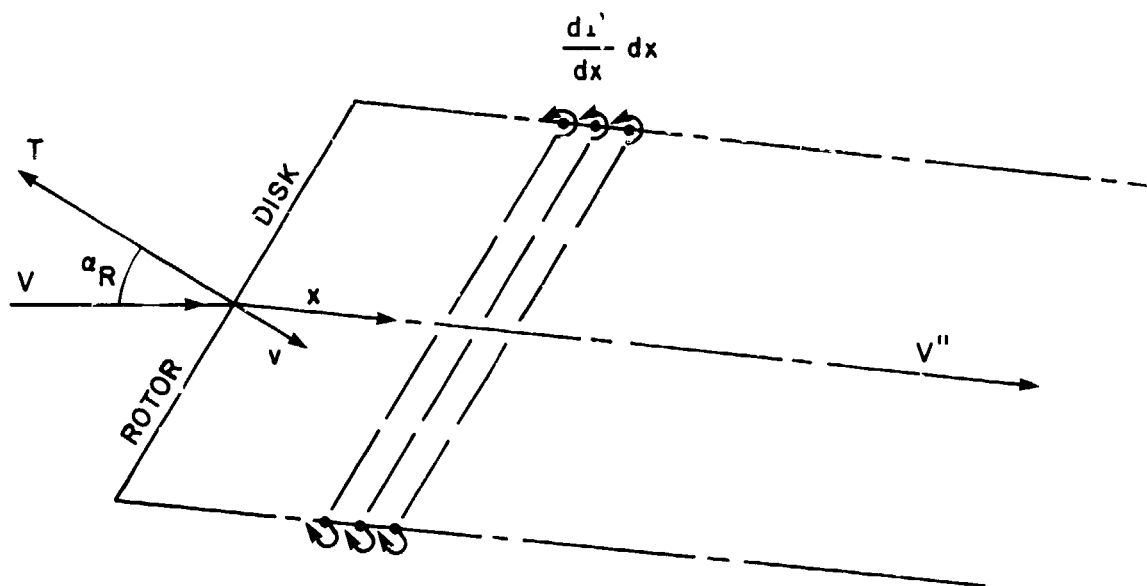
Then the vorticity distribution on the surface of the cylinder is given by

$$\frac{d\Gamma}{dx} \approx \frac{b\Gamma_o}{\Delta x} \quad (11)$$

where $\Delta x =$ length of vortex cylinder generated during one revolution of the rotor, and measured along the axis of the cylinder.



(a) Wake Geometry



(b) Resultant Flow Velocity

Figure 7. Vortex Cylinder Model.

ORIGINAL PAGE IS
OF POOR QUALITY

Also, it is noted that

$$\Delta x = V'' \Delta t \quad (12)$$

where V'' denotes the mean convection velocity of the far wake and $\Delta t = \frac{2\pi}{\Omega}$ for one rotor revolution.

Therefore, Equation (11) becomes

$$\begin{aligned} \frac{d\Gamma}{dx} &= \frac{b\Gamma_o\Omega}{2\pi V''} \\ &= \frac{T}{\rho\pi R^2 V''} \end{aligned} \quad (13)$$

The convection velocity of the portion of the vortex cylinder in the far wake is given by the vector (see Figure 7).

$$V'' = [(V + 2v \cos \alpha_R), (2v \sin \alpha_R)] \quad (14)$$

where v is given by Equation (6).

This model is assumed to be valid for the following conditions:

$$V = 130 \text{ knots to } V_{\max}$$

$$\alpha_R = 0 \text{ to } 60 \text{ degrees}$$

SECTION 5

INCOMPRESSIBLE POTENTIAL AERODYNAMICS FOR WING-FUSELAGE-TAIL-ROTOR WAKE INTERFERENCE

In this section, the general formulation for incompressible potential aerodynamics for separated flows is presented. It may be worth noting that for incompressible fluids potential flows are obtained if the fluid is inviscid and the velocity flow field is irrotational at time $t = 0$. Accordingly, these hypotheses are invoked here. Since the analysis of rotors was not included in previous descriptions of the formulation for SUSSA ACTS (References 43 through 47), a new formulation is presented here, starting from basic principles.

5.1 INCOMPRESSIBLE INVISCID FLOWS

Assuming the fluid to be [1]^{*} inviscid, and [2] incompressible, the motion is governed by the Euler equations

$$\left(\frac{\partial}{\partial t} + \bar{\mathbf{V}} \cdot \bar{\nabla} \right) \bar{\mathbf{V}} = - \frac{1}{\rho} \bar{\nabla} p \quad (15)$$

and the continuity equation (for incompressible fluid)

$$\bar{\nabla} \cdot \bar{\mathbf{V}} = 0 \quad (16)$$

where $\bar{\mathbf{V}}$ is the velocity vector with respect to a prescribed frame of reference, p is the pressure, ρ the (constant) density, t the time, whereas

$$\bar{\nabla} = \bar{\mathbf{i}} \frac{\partial}{\partial x} + \bar{\mathbf{j}} \frac{\partial}{\partial y} + \bar{\mathbf{k}} \frac{\partial}{\partial z} \quad (17)$$

is the del operator. Equations (15) and (16) form a system of four partial differential equations for four unknowns V_x , V_y , V_z , and p .

^{*}Numbers in brackets indicate new hypotheses introduced in the formulation.

ORIGINAL PAGE IS
OF POOR QUALITY

In order to complete the formulation of the problem, the boundary conditions at infinity on the body and on the wake must be obtained. Here it will be assumed that [3] the unperturbed flow consists of uniform translation, say in the x-axis direction. Hence, the boundary condition at infinity may be written as

$$\bar{V} = U_{\infty} \bar{i} \quad (18)$$

In particular $U_{\infty} = 0$ for helicopters in hover.

On the body it is assumed that [4] the surface of the body is impermeable, i.e., the normal components of the velocity, \bar{V} , of the fluid, and of the velocity, \bar{V}_B , of the body coincide on a point, P , on the surface, Σ_B , of the body:

$$(\bar{V} - \bar{V}_B) \cdot \bar{n} = 0 \quad (\text{for } P \text{ on } \Sigma_B) \quad (19)$$

where \bar{n} is the normal to Σ_B at P .

Next consider the boundary condition on the wake for lifting bodies. Here it is assumed that [5] the body has certain separation lines (in particular sharp trailing edges) and that the velocity flow field has surfaces of discontinuity (wakes) emanating from these separation lines (or trailing edges). Indicating with 1 and 2 the two sides of the wake, let \bar{n} be the outward normal on side 1 and let

$$\Delta f = f_1 - f_2 \quad (20)$$

indicate the discontinuity of any functions, f , across the wake surface. (For the classical wing-wake, 1 and 2 correspond to upper and lower sides, respectively; \bar{n} is the upper normal and $\Delta f = f_{\text{upper}} - f_{\text{lower}}$). The boundary condition on the wake-surface, Σ_W , is that there is no pressure discontinuity on a point, P , on the wake

$$\Delta p = 0 \quad (\text{for } P \text{ on } \Sigma_W) \quad (21)$$

This condition can be expressed more conveniently in terms of the velocity discontinuity; however, this requires the introduction of the concept of Lamb surfaces.

These surfaces may be avoided in the case of potential flow and, therefore, the boundary condition is given here for potential flows only.

Equations (15), (16), (18), (19), and (21) completely define the problem in terms of four partial differential equations for four unknowns V_x , V_y , V_z and p , with the corresponding boundary conditions.

5.2 DIFFERENTIAL FORMULATION FOR INCOMPRESSIBLE POTENTIAL FLOWS

In the preceding section, the flow was assumed to be [1] incompressible, and [2] inviscid. Next, assume [6] the flow to be initially irrotational: then the flow remains irrotational at all times and, therefore, there exists a potential function, Φ , such that

$$\bar{V} = \bar{\nabla} \Phi \quad (22)$$

In this case, Equation (15) may be integrated to yield Bernoulli's theorem*

$$\frac{\partial \Phi}{\partial t} + \frac{1}{2} |\bar{\nabla} \Phi|^2 + \frac{p}{\rho} = \frac{1}{2} U_{\infty}^2 + \frac{p_{\infty}}{\rho} \quad (23)$$

The constant on the right hand side is obtained from the conditions at infinity, Equation (18).

Furthermore, Equation (16) may be rewritten as

$$\nabla^2 \Phi = 0 \quad (24)$$

*The x-derivative of Equation (23) yields

$$\begin{aligned} \frac{\partial}{\partial x} \left(\frac{\partial \Phi}{\partial t} + \frac{1}{2} |\bar{\nabla} \Phi|^2 + \frac{p}{\rho} \right) &= \frac{\partial}{\partial t} \left[\frac{\partial \Phi}{\partial x} + \frac{\partial \Phi}{\partial x} \frac{\partial^2 \Phi}{\partial x^2} + \frac{\partial \Phi}{\partial y} \frac{\partial^2 \Phi}{\partial x \partial y} \right. \\ &\quad \left. + \frac{\partial \Phi}{\partial z} \frac{\partial^2 \Phi}{\partial x \partial z} + \frac{1}{\rho} \frac{\partial p}{\partial x} \right] = \left(\frac{\partial}{\partial t} + \bar{V} \cdot \bar{\nabla} \right) V_x + \frac{1}{\rho} \frac{\partial p}{\partial x} = 0 \end{aligned}$$

in agreement with the first component of Equation (15).

where ∇^2 is the Laplacian operator.

Similarly, Equation (18) is equivalent to

$$\Phi = U_{\infty} x \quad (\text{for } P \text{ at } \infty) \quad (25)$$

while Equation (19) may be rewritten as

$$\frac{\partial \Phi}{\partial n} = \bar{V}_B \cdot \bar{n} \quad (26)$$

Next consider the boundary condition on the wake, Equation (21). Combining Equations (21) and (23) yields

$$\frac{\partial}{\partial t} (\Phi_1 - \Phi_2) + \frac{1}{2} (\bar{V}\Phi_1 \cdot \bar{V}\Phi_1 - \bar{V}\Phi_2 \cdot \bar{V}\Phi_2) = 0 \quad (27)$$

or

$$\left(\frac{\partial}{\partial t} + \bar{V}_A \cdot \bar{V} \right) \Delta \Phi = 0 \quad (28)$$

where

$$\Delta \Phi = \Phi_1 - \Phi_2 \quad (29)$$

whereas

$$\bar{V}_A = \frac{1}{2} (\bar{V}\Phi_1 + \bar{V}\Phi_2) = \frac{1}{2} (\bar{V}_1 + \bar{V}_2) \quad (30)$$

is the average value of the velocity: this average value may be attributed to the point, P_w , on the wake. Equation (28) may thus be interpreted as

$$\Delta \Phi (P_w) = \text{constant in time} \quad (31)$$

where P_w is the physical point of the wake being convected with velocity \bar{V}_A . Note that Equation (28) implies that the wake is tangent to \bar{V}_A . In particular, in the steady state,

the wake is composed of the streamlines of the points P_w emanating from the trailing edges or other separation lines. Equation (24) is a partial differential equation for Φ with boundary conditions given by Equations (25), (26), and (28). Once Φ is known the velocity is given by Equation (22) while the pressure is obtained from Equation (23). It may be worth noting that the potential aerodynamic formulation considered in this section is considerably simpler than the formulation based upon physical variables (\vec{V} and p) since the former gives one linear partial differential equation instead of four nonlinear ones.

5.3 PERTURBATION POTENTIAL

In order to use the Green theorem approach, it is convenient to have homogeneous boundary conditions at infinity. This can be accomplished by introducing the perturbation potential φ , related to the potential Φ by

$$\Phi = U_{\infty} x + \varphi \quad (32)$$

Then, Equation (24) yields

$$\nabla^2 \varphi = 0 \quad (33)$$

while the condition at infinity, Equation (25), becomes homogeneous

$$\varphi = 0 \quad (\text{for } P \text{ at } \infty) \quad (34)$$

On the other hand, combining Equations (26) and (32), the boundary condition on the body is now given by

$$\frac{\partial \varphi}{\partial n} = (-U_{\infty} \vec{i} + \vec{V}_B) \cdot \vec{n} \quad (35)$$

whereas, on the wake (see Equations (28) and (31))

$$\left(\frac{\partial}{\partial t} + \vec{V}_A \cdot \vec{\nabla} \right) \Delta \varphi = 0 \quad (36)$$

ORIGINAL PAGE IS
OF POOR QUALITY

or

$$\Delta \varphi (P_w) = \text{constant in time} \quad (37)$$

Furthermore, once φ is known, the perturbation velocity

$$\bar{v} = \bar{\nabla} \varphi \quad (38)$$

may be evaluated and then the velocity is given by

$$\bar{V} = U_{\infty} \bar{i} + \bar{v} \quad (39)$$

Accordingly, the Bernoulli theorem may be rewritten as

$$\frac{\partial \varphi}{\partial t} + U_{\infty} \frac{\partial \varphi}{\partial x} + \frac{1}{2} |\bar{\nabla} \varphi|^2 + \frac{p}{\rho} = \frac{p_{\infty}}{\rho} \quad (40)$$

It may be worth noting that the above equations could be obtained in a slightly different way, i.e., by assuming the frame of reference connected with the undisturbed air: the velocity of the body in such a frame of reference would be given by $-U_{\infty} \bar{i} + \bar{V}_B$, in agreement with Equation (35).

5.4 GREEN'S FORMULA FOR LAPLACE'S EQUATION

Consider two arbitrary functions f and g and note that

$$\begin{aligned} \bar{\nabla} \cdot (f \bar{\nabla} g) &= \bar{\nabla} f \cdot \bar{\nabla} g + f \nabla^2 g \\ \bar{\nabla} \cdot (g \bar{\nabla} f) &= \bar{\nabla} g \cdot \bar{\nabla} f + g \nabla^2 f \end{aligned} \quad (41)$$

or

$$\bar{\nabla} \cdot (f \bar{\nabla} g - g \bar{\nabla} f) = f \nabla^2 g - g \nabla^2 f \quad (42)$$

According to the Gauss theorem, for any arbitrary vector \bar{a} ,

$$\iiint_{V_i} \bar{\nabla} \cdot \bar{a} dV_i = \oint_{\Sigma} \bar{a} \cdot \bar{n} d\Sigma \quad (43)$$

where Σ surrounds V_i and \bar{n} is the inward directed normal (Figure 8). Combining Equations (42) and (43) yields

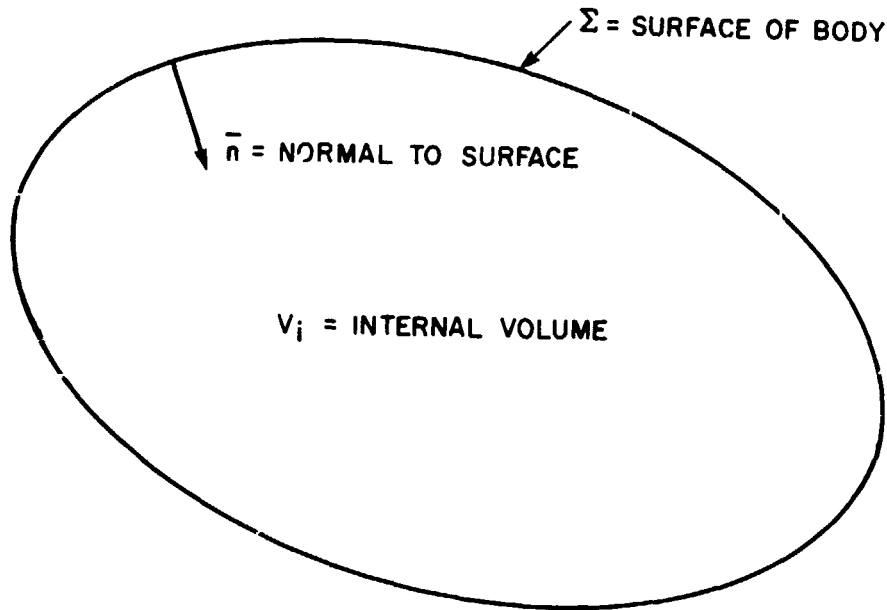


Figure 8. Geometry for Green's Formula for V_i Internal to Σ .

$$\begin{aligned} \iiint_{V_i} (f \nabla^2 g - g \nabla^2 f) dV &= \oint_{\Sigma} (f \bar{\nabla} g - g \bar{\nabla} f) \cdot \bar{n} d\Sigma \\ &= \oint_{\Sigma} \left(f \frac{\partial g}{\partial n} - g \frac{\partial f}{\partial n} \right) d\Sigma \end{aligned} \quad (44)$$

Next assume that both f and g satisfy the Laplace equation, i.e.,

$$\nabla^2 f = \nabla^2 g = 0 \quad (\text{in } V_i) \quad (45)$$

Then Equation (44) yields

ORIGINAL PAGE IS
OF POOR QUALITY

$$\oiint_{\Sigma} \left(f \frac{\partial g}{\partial n} - g \frac{\partial f}{\partial n} \right) d\Sigma = 0 \quad (46)$$

which is the desired Green's formula for the Laplace equation.

Next choose the function g to be the simplest function which satisfies the Laplace equation: if g is only a function of the distance, r , from a specified point, P_* , then the only such function that satisfies the Laplace equation is

$$g = \frac{A}{r} + B \quad (47)$$

where

$$r = |P - P_*| \quad (48)$$

Note that P_* must be outside the volume, V_i ; otherwise Equation (45) is not satisfied at P_* . Note also that the value of B does not affect Equation (46) under the condition

$$\oiint_{\Sigma} \frac{\partial f}{\partial n} d\Sigma = 0 \quad (49)$$

which is obtained from Equation (46) with $g = 1$. Therefore, the convenient value $B = 0$ is used here. For this case the function g represents a source. It is convenient to choose A such that g represents a unit source; that is, a source with flux equal to one. This is obtained with $A = -1/4\pi$, i.e.,*

*For, in this case, the flux through a spherical surface of radius R , is given by

$$\iint_{\Sigma} \vec{v} \cdot \vec{n} d\Sigma = \iint_{\Sigma} \frac{\partial g}{\partial r} \bigg|_{r=R} d\Sigma = \frac{1}{4\pi R^2} \cdot 4\pi R^2 = 1$$

$$g = - \frac{1}{4\pi r} \quad (50)$$

Combining Equations (46) and (50) one obtains the desired Green formula for the Laplace equation

$$\oint_{\Sigma} \left[f \frac{\partial}{\partial n} \left(\frac{-1}{4\pi r} \right) - \frac{\partial f}{\partial n} \left(\frac{-1}{4\pi r} \right) \right] d\Sigma = 0 \quad (51)$$

5.5 GREEN'S THEOREM FOR INCOMPRESSIBLE POTENTIAL AERODYNAMICS

In order to obtain the Green theorem for incompressible aerodynamics (Laplace's equation for the exterior problem, i.e., for V_i outside the surface Σ_0), it is convenient to consider the surface Σ composed of three branches as indicated in Figure 9. Note that the inward normal for V_i is outward to Σ_0 . Σ_1 is a spherical surface of radius ϵ and center P_* , while Σ_2 is a spherical surface of radius R_{Σ_2} and center P_* .

Then Equation (51), for $f = \varphi$, reduces to

$$\oint_{\Sigma_0 + \Sigma_1 + \Sigma_2} \left[\varphi \frac{\partial}{\partial n} \left(\frac{-1}{4\pi r} \right) - \frac{\partial \varphi}{\partial n} \left(\frac{-1}{4\pi r} \right) \right] d\Sigma = 0 \quad (52)$$

Note that as the radius ϵ of Σ_1 goes to zero

ORIGINAL PAGE 15
OF POOR QUALITY

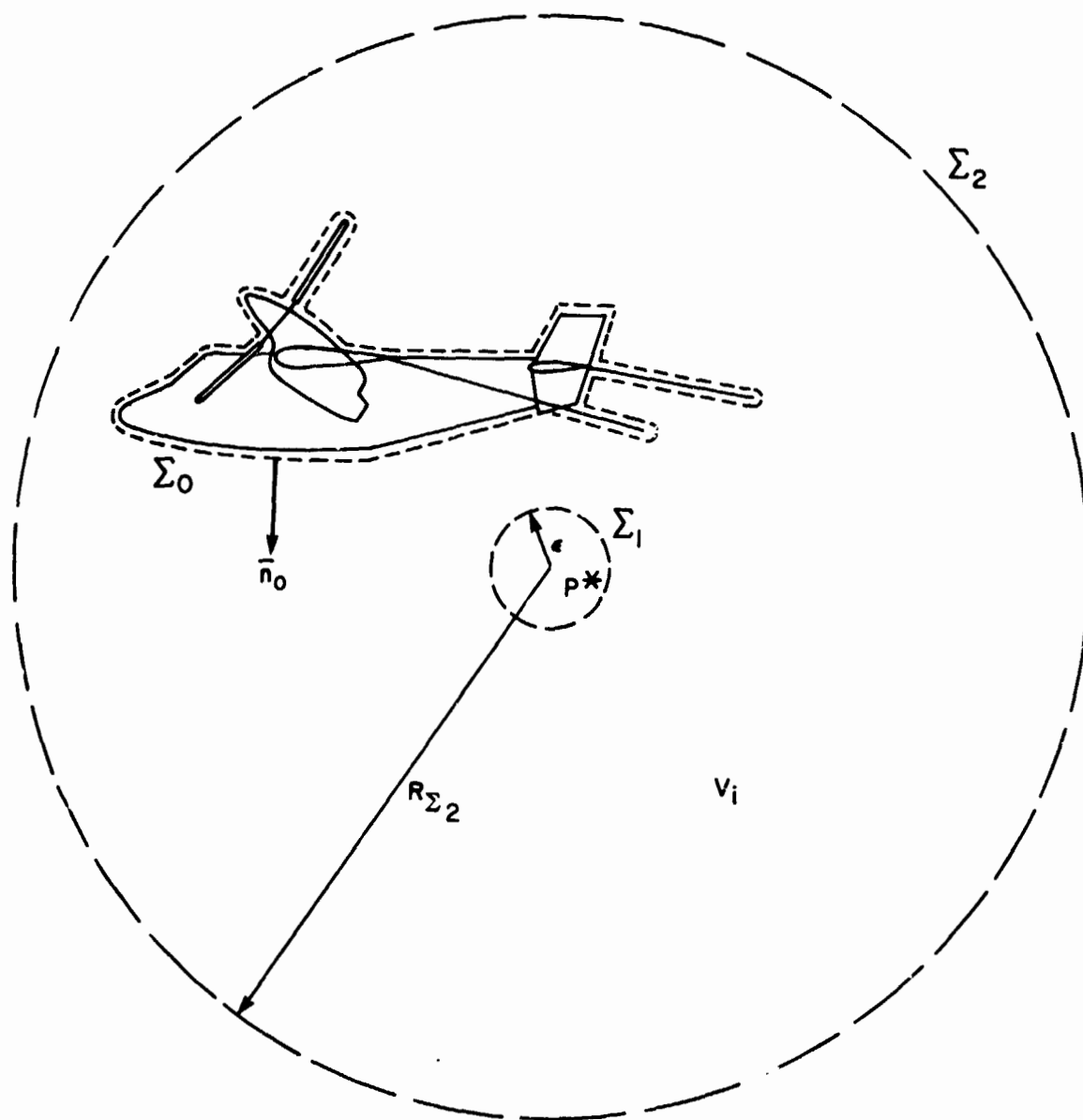


Figure 9. Geometry for Green's Theorem for Potential Aerodynamics of Incompressible Flows.

$$\begin{aligned}
& \lim_{\epsilon \rightarrow 0} \oint_{\Sigma_1} \left[\varphi \frac{\partial}{\partial n} \left(\frac{-1}{4\pi r} \right) - \frac{\partial \varphi}{\partial n} \left(\frac{-1}{4\pi r} \right) \right] d\Sigma \\
&= \lim_{\epsilon \rightarrow 0} \left[\varphi_* \oint_{\Sigma_1} \frac{\partial}{\partial r} \left(\frac{-1}{4\pi r} \right) d\Sigma - \left(\frac{\partial \varphi}{\partial n} \right)_* \oint_{\Sigma_1} \frac{-1}{4\pi r} d\Sigma \right] \\
&= \lim_{\epsilon \rightarrow 0} \left[\varphi_* \frac{1}{4\pi \epsilon^2} \oint_{\Sigma_1} d\Sigma + \left(\frac{\partial \varphi}{\partial n} \right)_* \frac{i}{4\pi \epsilon} \oint_{\Sigma_1} d\Sigma \right] \\
&= \lim_{\epsilon \rightarrow 0} \left[\varphi_* + \left(\frac{\partial \varphi}{\partial n} \right)_* \epsilon \right] = \varphi_* \tag{53}
\end{aligned}$$

whereas, as the radius R_{Σ_2} goes to infinity

$$\begin{aligned}
& \lim_{R_{\Sigma_2} \rightarrow \infty} \oint_{\Sigma_2} \left[\varphi \frac{\partial}{\partial n} \left(\frac{-1}{4\pi r} \right) - \frac{\partial \varphi}{\partial n} \left(\frac{-1}{4\pi r} \right) \right] d\Sigma \\
&= \lim_{R_{\Sigma_2} \rightarrow \infty} \left[\varphi_{\infty} + \left(\frac{\partial \varphi}{\partial n} \right)_{\infty} R_* \right] \\
&= 0 \tag{54}
\end{aligned}$$

under the conditions[†]

$$\lim_{R_{\Sigma_2} \rightarrow \infty} \varphi = 0 \tag{55}$$

[†]It is verified a posteriori (Equations (67) and (68)) that these conditions are satisfied.

ORIGINAL PAGE IS
OF POOR QUALITY

$$\lim_{R_{\Sigma_2} \rightarrow \infty} \frac{\partial \varphi}{\partial n} R_{\Sigma_2} = 0 \quad (56)$$

Therefore, as ϵ tends to zero and R_{Σ_2} tends to infinity, Equation (52), according to Equations (53) and (54), yields

$$\varphi_* = \oint_{\Sigma_0} \left[\frac{\partial \varphi}{\partial n} \left(\frac{-1}{4\pi r} \right) - \varphi \frac{\partial}{\partial n} \left(\frac{-1}{4\pi r} \right) \right] d\Sigma_0 \quad (57)$$

It may be worth noting that if the point P_* is inside Σ_0 , then there is no need for the surface Σ_1 and, therefore, in this case Equation (52) yields simply

$$0 = \oint_{\Sigma_0} \left[\frac{\partial \varphi}{\partial n} \left(\frac{-1}{4\pi r} \right) - \varphi \frac{\partial}{\partial n} \left(\frac{-1}{4\pi r} \right) \right] d\Sigma_0 \quad (58)$$

Equations (57) and (58) may be combined by writing

$$E_* \varphi = \oint_{\Sigma_0} \left[\frac{\partial \varphi}{\partial n} \left(\frac{-1}{4\pi r} \right) - \varphi \frac{\partial}{\partial n} \left(\frac{-1}{4\pi r} \right) \right] d\Sigma_0 \quad (59)$$

$$E_* = E(P_*) = \begin{cases} 1 & (P_* \text{ outside } \Sigma_0) \\ 0 & (P_* \text{ inside } \Sigma_0) \end{cases} \quad (60)$$

Next let Σ_0 be identified with the surface surrounding the fuselage, rotor and wakes emanating from the trailing edge of wing, tail and rotor blades. Then Equation (59) may be rewritten as[†]

$$\begin{aligned} 4\pi E_* \varphi_* = & - \oint_{\Sigma_B + \Sigma_R} \left[\frac{\partial \varphi}{\partial n} \frac{1}{r} - \varphi \frac{\partial}{\partial n} \left(\frac{1}{r} \right) \right] d\Sigma \\ & + \iint_{E'_W + \Sigma'_T + \Sigma'_R} \Delta \varphi \frac{\partial}{\partial n} \left(\frac{1}{r} \right) d\Sigma \end{aligned} \quad (61)$$

[†]Note that the wake surfaces Σ'_W , Σ'_T and Σ'_R are open surfaces. The source integrals on the wake surfaces are identically equal to zero since the values of $\partial \varphi / \partial n$ on the opposite sides of these surfaces are equal to zero.

where Σ_B is the (closed) surface of the body (wing-fuselage-tail), Σ_R is the (closed) surface of the rotor blades, Σ'_W is the (open) surface of the wing wake, Σ'_T is the (open) surface of the tail wake and Σ'_R represents the wakes of the rotor blades. Furthermore (see Equation (20)),

$$\Delta \varphi = \varphi_1 - \varphi_2 \quad (62)$$

while \bar{n} is the normal on the side 1 of the wake. Note that $\Delta \varphi$ is known from Equation (37).

In addition if P_* is on $\Sigma_B + \Sigma_R$ then as shown in Appendix C of Reference 45, $E_* = 1/2$. Thus Equation (59) may be rewritten as

$$E_* = E(P_*) = \begin{cases} 1 & (P_* \text{ outside } \Sigma_B + \Sigma_R) \\ 1/2 & (P_* \text{ on } \Sigma_B + \Sigma_R) \\ 0 & (P_* \text{ inside } \Sigma_B + \Sigma_R) \end{cases} \quad (63)$$

Note that on Σ_B and Σ_R , $\partial \varphi / \partial n$ is prescribed by the boundary conditions, Equation (35).

Thus, for P_* on Σ , Equation (59) is an integral equation relating φ to the prescribed $\partial \varphi / \partial n$. This equation is used to analyze the potential flow for interaction of fuselage and rotor.

5.6 CONDITIONS AT INFINITY

In this section Equations (55) and (56) are verified. Note that R_{Σ_2} goes to infinity, Equation (57) yields

$$\begin{aligned} \lim_{R_{\Sigma_2} \rightarrow \infty} \varphi_* &= \lim_{R_{\Sigma_2} \rightarrow \infty} \oint_{\Sigma_0} \left[\frac{\partial \varphi}{\partial n} \left(\frac{-1}{4\pi r} \right) - \varphi \frac{\partial}{\partial n} \left(\frac{-1}{4\pi r} \right) \right] d\Sigma \\ &= \lim_{R_{\Sigma_2} \rightarrow \infty} \left[\frac{1}{4\pi r} \oint_{\Sigma_0} \frac{\partial \varphi}{\partial n} d\Sigma - \frac{1}{4\pi r^2} \oint_{\Sigma_0} \varphi \frac{\bar{r} \cdot \bar{n}}{r} d\Sigma \right] \\ &= 0 \end{aligned} \quad (64)$$

ORIGINAL PAGE OF
OF POOR QUALITY

since the flux through Σ_0 is equal to zero, i.e.,

$$\oiint \frac{\partial \varphi}{\partial n} d\Sigma = 0 \quad (65)$$

while

$$\lim_{R_{\Sigma_2} \rightarrow \infty} \oiint \varphi \frac{\vec{r} \cdot \vec{n}}{r} d\Sigma = \text{finite} \quad (66)$$

Equation (61) implies

$$\varphi = \frac{C}{r^2} + O(r^{-3}) \quad \text{at } \infty \quad (67)$$

and

$$\frac{\partial \varphi}{\partial n} = \frac{D}{r^3} + O(r^{-4}) \quad \text{at } \infty \quad (68)$$

in agreement with Equation (56).

SECTION 6

INCOMPRESSIBLE POTENTIAL AERODYNAMICS FOR COMPLETE CONFIGURATION WITH ACTUATOR DISK

The formulation presented in the preceding section is general and may be applied, in particular, to rotors. It may be noted, however, that the rotor-fuselage interaction is an unsteady periodic phenomenon. Periodicity is obtained when the rotor moves through an angle equal to 2π divided by the number of blades, b . If b goes to infinity, the phenomenon becomes steady. Therefore, given the preliminary nature of the present analysis, it is convenient to consider the limit of the rotor fuselage analysis as the number of blades goes to infinity. The model representing an infinite-blade rotor is called an actuator disk. The modifications necessary to extend the formulation to include actuator disks are presented in this section. For simplicity an actuator disk by itself is considered first. The extension to the complete configuration is considered in Subsection 6.3.

6.1 ACTUATOR DISK

Consider a rotor composed of b blades. Let b go to infinity, while the chord of the blades goes to zero. As the aspect ratio of each blade goes to infinity, the vorticity shed by each blade is more and more concentrated near the root and the tip of the blade. In the limit, only tip vortices and one central vortex exists. Therefore, the actuator disk may be represented as a series of infinite blades with a wake composed of infinite vortices emanating from the tip of the blade and one additional vortex emanating from the center of the disk. Thus, the flow field is potential outside the surface Σ_0 shown in Figure 10. Therefore, Equation (59) is applicable in this case, and yields

$$4\pi E_{**}\varphi_* = - \oint_{\Sigma_D} \left[\frac{\partial \varphi}{\partial n} \left(\frac{1}{r} \right) - \varphi \frac{\partial}{\partial n} \left(\frac{1}{r} \right) \right] d\Sigma \\ + \oint_{\Sigma_D + \Sigma_B'} \Delta \varphi \frac{\partial}{\partial n} \left(\frac{1}{r} \right) d\Sigma \quad (69)$$

ORIGINAL PAGE IS
OF POOR QUALITY

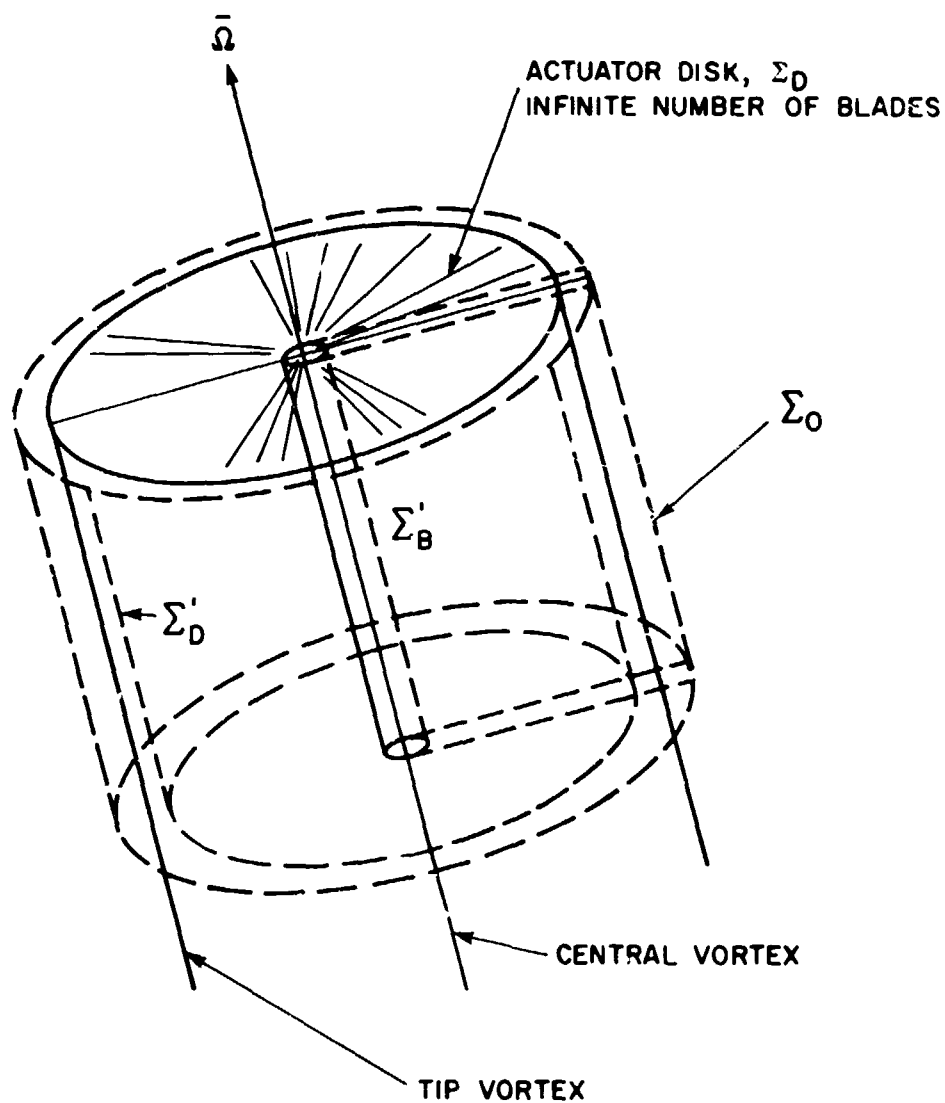


Figure 10. Surface Σ_0 for Actuator Disk Analysis. The Surface Surrounds the Actuator Disk, the Central Vortex and the Shed Tip Vortices.

where Σ_D is a (closed) surface surrounding the blades of the rotor and representing the actuator disk, while Σ_D' is the surface of the disk wake emanating from the circle described by the rotor-blade tips and Σ_B' is a branch surface connecting the central vortex to Σ_D' . It may be worth noting that Equation (69) is formally equal to Equation (61). Therefore, the method presented in the preceding section is applicable to actuator disks as well. The two differences are that $\partial\varphi/\partial n$ cannot be obtained from the usual boundary conditions on the surface of the body and that $\Delta\varphi$ on Σ_B' cannot be determined. This last point is examined in Appendix B. The new boundary conditions for actuator disk aerodynamics are presented in the next subsection.

6.2 ACTUATOR DISK BOUNDARY CONDITIONS

The boundary condition on the rotor blade according to Equation (35) with

$$\bar{V}_B = \bar{\Omega} \times \bar{r} \quad (70)$$

is

$$\frac{\partial\varphi}{\partial n_B} = (-U_\infty \bar{i} + \bar{\Omega} \times \bar{r}) \cdot \bar{n}_B \quad (71)$$

where \bar{n}_B is the normal to the blade. On the other hand, the boundary conditions used on the surface of the actuator disk are expressed in terms of the normal wash, $\partial\varphi/\partial n_D$, on the surface of the disk (see Figure 11). Therefore, the relationship between $\partial\varphi/\partial n_B$ and $\partial\varphi/\partial n_D$ is necessary and is obtained here. Let \bar{s}_B and \bar{s}_D be the directions of the components of the velocity tangential to the surface of the blade and the disk, respectively. Then

$$\begin{aligned} \bar{\nabla}\varphi &= \frac{\partial\varphi}{\partial n_B} \bar{n}_B + \frac{\partial\varphi}{\partial s_B} \bar{s}_B \\ &= \frac{\partial\varphi}{\partial n_D} \bar{n}_D + \frac{\partial\varphi}{\partial s_D} \bar{s}_D \end{aligned} \quad (72)$$

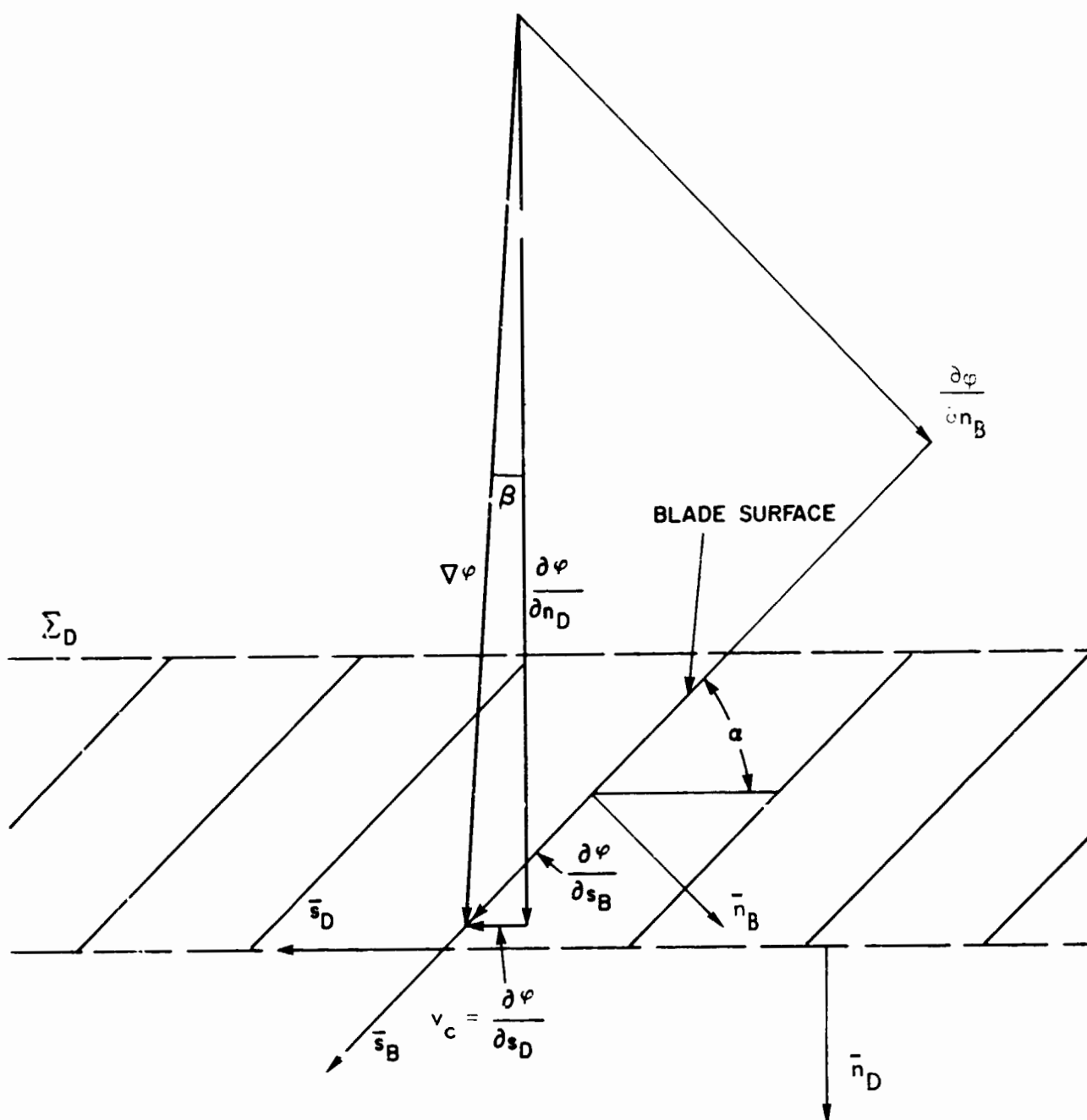


Figure 11. Boundary Conditions for the Actuator Disk. Σ_D is the Surface Surrounding the Actuator Disk.

Note that

$$\frac{\partial \varphi}{\partial n_D} = \bar{\nabla} \varphi \cdot \bar{n}_D = \frac{\partial \varphi}{\partial n_B} \bar{n}_B \cdot \bar{n}_D + \frac{\partial \varphi}{\partial s_B} \bar{s}_B \cdot \bar{n}_D \quad (73)$$

and

$$\frac{\partial \varphi}{\partial s_D} = \bar{\nabla} \varphi \cdot \bar{s}_D = \frac{\partial \varphi}{\partial n_B} \bar{n}_B \cdot \bar{s}_D + \frac{\partial \varphi}{\partial s_B} \bar{s}_B \cdot \bar{s}_D \quad (74)$$

Eliminating $\partial \varphi / \partial s_B$ between Equations (73) and (74) yields

$$\begin{aligned} \frac{\partial \varphi}{\partial n_D} &= \frac{\partial \varphi}{\partial n_B} \frac{(\bar{n}_B \cdot \bar{n}_D)(\bar{s}_B \cdot \bar{s}_D) - (\bar{n}_B \cdot \bar{s}_D)(\bar{n}_D \cdot \bar{s}_B)}{\bar{s}_B \cdot \bar{s}_D} + \frac{\bar{s}_B \cdot \bar{n}_D}{\bar{s}_B \cdot \bar{s}_D} \frac{\partial \varphi}{\partial s_D} \\ &= \frac{\bar{n}_B \times \bar{s}_B \cdot \bar{n}_D \times \bar{s}_D}{\bar{s}_B \cdot \bar{s}_D} \frac{\partial \varphi}{\partial n_B} + \frac{\bar{s}_B \cdot \bar{n}_D}{\bar{s}_B \cdot \bar{s}_D} \frac{\partial \varphi}{\partial s_D} \end{aligned} \quad (75)$$

Next note that

$$\frac{\partial \varphi}{\partial s_D} / \frac{\partial \varphi}{\partial n_D} = \tan \theta \quad (76)$$

where θ is the angle between $\bar{\nabla} \varphi$ and \bar{n}_D . Therefore Equation (75) may be rewritten as

$$\frac{\partial \varphi}{\partial n_D} \left(1 - \frac{\bar{s}_B \cdot \bar{n}_D}{\bar{s}_B \cdot \bar{s}_D} \tan \theta \right) = \frac{\bar{n}_B \times \bar{s}_B \cdot \bar{n}_D \times \bar{s}_D}{\bar{s}_B \cdot \bar{s}_D} \frac{\partial \varphi}{\partial n_B} \quad (77)$$

which is the desired relationship between $\frac{\partial \varphi}{\partial n_D}$ (necessary for the solution of the problem) and $\frac{\partial \varphi}{\partial n_B}$ (known from the boundary conditions on the blade, Equation (71)).

ORIGINAL PAGE IS
OF POOR QUALITY

Next consider a simpler expression for Equation (77): note that usually the radial component of $\nabla\phi$ is negligible. Then the configuration on a cylindrical surface is represented in Figure 11. In this case

$$\begin{aligned}\bar{n}_B \times \bar{s}_B \cdot \bar{n}_D \times \bar{s}_D &= 1 \\ \bar{s}_B \cdot \bar{s}_D &= \cos \alpha\end{aligned}\tag{78}$$

$$\bar{s}_B \cdot \bar{n}_D = \sin \alpha$$

and Equation (77) reduces to

$$\frac{\partial \phi}{\partial n_D} = \frac{1}{\cos \alpha} \frac{1}{1 - \tan \alpha \tan \beta} \frac{\partial \phi}{\partial n_B}\tag{79}$$

where α is the angle of the blade section for a given angular position.*

The boundary condition on the actuator disk can be written in terms of rotor parameters. It is shown in Figure 11 that

$$\tan \beta = \frac{v_c}{\frac{\partial \phi}{\partial n_D}}\tag{80}$$

with v_c denoting the circumferential velocity component. The closed line integral of the velocity vector for the actuator disk yields an additional relationship (assuming N_c to be independent of the circumferential location).

$$\Delta \phi_B = \oint \bar{v} \cdot d\bar{s} = 2\pi R v_c\tag{81}$$

*It is emphasized that different values of ϕ in the boundary condition do not affect the lift (thrust) on the rotor, although the flow through the disk is changed. The lift (thrust) on the rotor is dependent upon the value of $\Delta \phi_B$, i.e., the discontinuity of the branch wake.

where $\Delta\varphi_B$ represents the circumferential discontinuity on the branch wake. Combining the above two equations yields

$$\tan \beta = \frac{\Delta\varphi_B}{2\pi R} \frac{1}{\frac{\partial\varphi}{\partial n_D}} \quad (82)$$

Hence, Equation (79) can be reduced to

$$\frac{\partial\varphi}{\partial n_D} = \frac{1}{\cos \alpha} \frac{\partial\varphi}{\partial n_B} + \frac{\Delta\varphi_B}{2\pi R} \tan \alpha \quad (83)$$

Under the assumptions used in Appendix C, the discontinuity, $\Delta\varphi_B$, is proportional to the thrust, T (see Equation C-16).

$$\Delta\varphi_B = \frac{T}{\frac{1}{2} \rho \Omega R^2} \quad (84)$$

Therefore, the actuator disk boundary condition becomes

$$\frac{\partial\varphi}{\partial n_D} = \frac{1}{\cos \alpha} \frac{\partial\varphi}{\partial n_B} + \frac{T}{\pi \rho \Omega R^3} \tan \alpha \quad (85)$$

or (see Equation C-17)

$$\frac{\partial\varphi}{\partial n_D} = \frac{1}{\cos \alpha} \frac{\partial\varphi}{\partial n_B} - \frac{1}{2} C_T \Omega R \tan \alpha \quad (86)$$

This is the desired expression which relates the boundary condition on the actuator disk to the rotor thrust and the downwash on the rotor blades.

Using classical blade element theory (Reference 41), the thrust coefficient (for rotor with large inflow) can be obtained in terms of specific rotor parameters. The exact relationship is given in Equation (108). In obtaining this expression, the profile drag is neglected, the angle of attack of the blade element is represented by its sine, and the pitch of a twisted blade is approximated by its value at three-quarter radius.

6.3 FORMULATION FOR COMPLETE CONFIGURATION

Consider a surface, Σ , surrounding the aircraft and its wakes as well as the actuator disk and its wake. Outside the surface Σ the flow is potential and, therefore, Equation (61) may be applied, with the surfaces of the disk Σ_D , and of its wake, Σ_D' replacing the surfaces of the rotor, Σ_R and its wake, Σ_R' . Therefore, Equation (61) may be rewritten as

$$4\pi E_* \varphi_* = \oint_{\Sigma_B + \Sigma_D} \left[\frac{\partial \varphi}{\partial n} \frac{1}{r} - \varphi \frac{\partial}{\partial n} \left(\frac{1}{r} \right) \right] d\Sigma + \iint_{\Sigma_W' + \Sigma_T' + \Sigma_D' + \Sigma_B'} \Delta \varphi \frac{\partial}{\partial n} \left(\frac{1}{r} \right) d\Sigma \quad (87)$$

The value of E_* is given by the equivalent of Equation (63), i.e.,

$$E_* = E(P_*) = \begin{cases} 1 & \text{for } P_* \text{ outside } \Sigma_B + \Sigma_D \\ 1/2 & \text{for } P_* \text{ on } \Sigma_B + \Sigma_D \\ 0 & \text{for } P_* \text{ inside } \Sigma_B + \Sigma_D \end{cases} \quad (88)$$

Note that on Σ_B , $\partial\varphi/\partial n$ is prescribed by Equation (35), whereas on Σ_D , $\partial\varphi/\partial n = \partial\varphi/\partial n_D$ is given by Equation (79) with $\partial\varphi/\partial n_B$ given by Equation (71). Note also, that with the introduction of the steady state approximation accomplished through the use of the actuator disk, Equation (37) simplifies considerably to yield

$$\Delta\varphi(P_w) = \text{constant along streamlines} \quad (89)$$

In addition, the geometry of the wake may be estimated as illustrated in Subsection 4.2.3. Therefore, on $\Sigma_B + \Sigma_D$, Equation (87) is an integral equation relating the unknown values of φ on the surfaces Σ_B and Σ_D to the corresponding value of the known normal derivative $\partial\varphi/\partial n$ (normal wash). The numerical solution of the integral equation is considered in Section 7.

SECTION 7

NUMERICAL FORMULATION

The ground formulation for incompressible potential aerodynamics was presented in Section 5. While the formulation is valid for fully unsteady aerodynamics, considerable computer time saving is obtained by the use of steady-state aerodynamics, which is achieved by replacing the rotor with an actuator disk (Subsection 6.1). The integral equation for the complete configuration is given in Subsection 6.3. The numerical formulation for the solution of the integral equation is outlined in this section.

The surfaces of the aircraft, the actuator disk, and their wakes are divided into small quadrilateral elements. Each element is replaced by a hyperboloidal surface defined by the four corner points of the element. In this process, the continuity of the surface is maintained. The unknown is assumed to be constant within each element and, therefore, the integral equation is approximated by a system of algebraic equations.

7.1 APPROXIMATE ALGEBRAIC SYSTEM

The results of Section 6 may be summarized by saying that the problem of incompressible potential aerodynamics for the complete actuator disk-aircraft configuration is governed by the integral equation obtained by combining Equations (87) and (88) on the body surface to obtain

$$\begin{aligned}
 2\pi\varphi_* = & - \iint_{\Sigma_B + \Sigma_D} \left[\frac{\partial\varphi}{\partial n} \left(\frac{1}{r} \right) - \varphi \frac{\partial}{\partial n} \left(\frac{1}{r} \right) \right] d\Sigma \\
 & + \iint_{E'_W + \Sigma'_T + \Sigma'_D + \Sigma'_B} \Delta\varphi \frac{\partial}{\partial n} \left(\frac{1}{r} \right) d\Sigma
 \end{aligned} \tag{90}$$

PRECEDING PAGE BLANK NOT REPRODUCED

In order to obtain an approximate solution for the integral equation, the surfaces Σ_B , Σ_D , Σ_W , Σ_T , and Σ_D' are divided into small quadrilateral elements, Σ_k . The values of φ and $\partial\varphi/\partial n$ are assumed to be constant within each element. The collocation method is then used, that is, Equation (90) is satisfied at the centroids, P_h , of the element, Σ_h . This yields

$$[\delta_{hk} - c_{hk} - w_{hk}] \{\varphi_k\} = [b_{hk}] \left\{ \left(\frac{\partial\varphi}{\partial n} \right)_k \right\} + \Delta\varphi_B W_h^B \quad (91)$$

where δ_{hk} is the Kronecker delta,

$$c_{hk} = \left[\frac{1}{2\pi} \iint_{\Sigma_k} \frac{\partial}{\partial n} \left(\frac{1}{r} \right) d\Sigma_k \right]_{P_* = P_h} \quad (92)$$

$$b_{hk} = \left[- \frac{1}{2\pi} \iint_{\Sigma_k} \frac{1}{r} d\Sigma_k \right]_{P_* = P_h} \quad (93)$$

In addition, $w_{hk} = 0$ for the elements not in contact with the trailing edge, while for the elements in contact with the trailing edge,

$$w_{hk} = \left[\pm \frac{1}{2\pi} \iint_{\Sigma_k'} \frac{\partial}{\partial n} \left(\frac{1}{r} \right) d\Sigma_k' \right]_{P_* = P_h} \quad (94)$$

where Σ_k' is the strip of the wake (bounded by two streamlines) emanating from the element Σ_k . The upper (lower) sign must be used for the upper (lower) side of the wake. (In deriving Equation (91), the value of φ_{TE} is approximated with the value of φ at the centroid of the elements adjacent to the trailing edge. This is reasonable in view of the Kutta condition.) Finally, $\Delta\varphi_B W_h^B$ with

$$w_h^B = \left[\frac{1}{2\pi} \iint_{\Sigma_B'} \frac{\partial}{\partial n} \left(\frac{1}{r} \right) d\Sigma_B' \right]_{P_* = P_h} \quad (95)$$

is the contribution of the branch wake. Note that $\Delta\varphi = \Delta\varphi_B$ is constant on the branch wake and, therefore, there is no need to divide Σ_B' into small elements. Note that $\Delta\varphi_B$ cannot be determined (see Appendix B), but has to be prescribed. Therefore, it is left on the right-hand side of Equation (91).

As shown in Appendix B, Equation (91) has the determinant equal to zero; to be more precise, one equation is a linear construction of the other. Therefore, in order to find the solution, one equation is dropped and one unknown is set equal to zero. Then, Equation (91) can be solved numerically to yield the remaining values of the unknowns, φ_k . In all the results presented here, the pressure is obtained from the Bernoulli theorem, Equation (40).

7.2 HYPERBOLOIDAL ELEMENT

The surface elements Σ_k are approximated by a hyperbolic paraboloid (hyperboloidal element, Figure 12)

$$\bar{p} = \bar{p}_0 + \xi \bar{p}_1 + \eta \bar{p}_2 + \xi \eta \bar{p}_3 \quad (96)$$

where \bar{p}_i are obtained in terms of the locations of the four corner points as

$$\begin{Bmatrix} \bar{p}_0 \\ \bar{p}_1 \\ \bar{p}_2 \\ \bar{p}_3 \end{Bmatrix} = \frac{1}{4} \begin{bmatrix} 1 & 1 & 1 & 1 \\ 1 & 1 & -1 & -1 \\ 1 & -1 & 1 & -1 \\ 1 & -1 & -1 & 1 \end{bmatrix} \begin{Bmatrix} \bar{p}_{++} \\ \bar{p}_{+-} \\ \bar{p}_{-+} \\ \bar{p}_{--} \end{Bmatrix} \quad (97)$$

ORIGINAL PAGE IS
OF POOR QUALITY

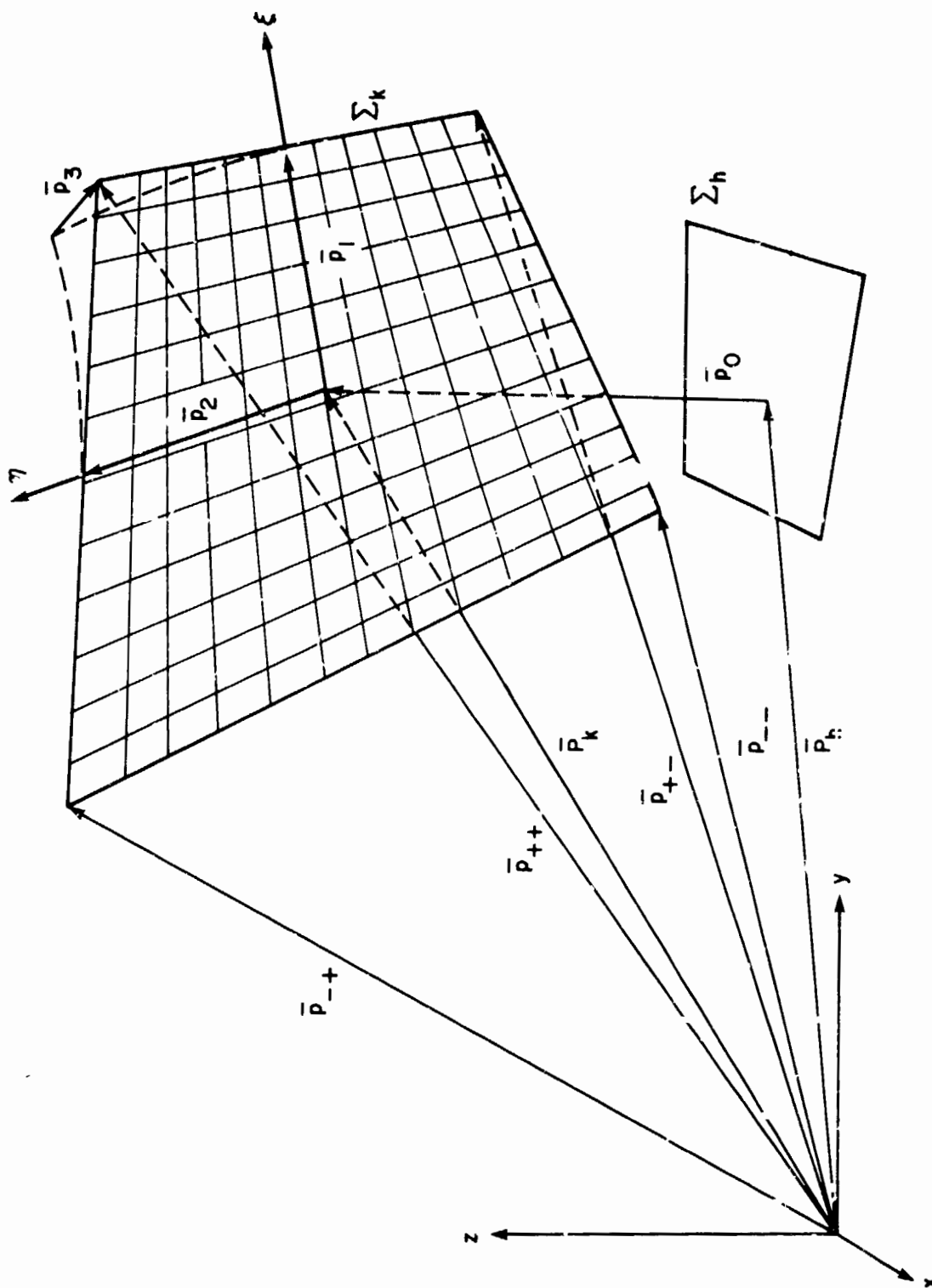


Figure 12. Hyperboloidal Element.

Note that quadrilateral hyperboloidal elements can be combined to yield a closed surface. Using these elements, the coefficients c_{hk} and b_{hk} can be evaluated analytically, as

$$c_{hk} = I_D(1, 1) - I_D(1, -1) - I_D(-1, 1) + I_D(-1, -1) \quad (98)$$

$$b_{hk} = I_S(1, 1) - I_S(1, -1) - I_S(-1, 1) + I_S(-1, -1) \quad (99)$$

with [using $-\pi/2 \leq \tan_p^{-1}(\cdot) \leq \pi/2$]

$$I_D(\xi, \eta) = (1/2\pi) \tan_p^{-1} \left((\bar{r} \times \bar{a}_1 \cdot \bar{r} \times \bar{a}_2) / (|\bar{r}| |\bar{r} \cdot \bar{a}_1 \times \bar{a}_2|) \right) \quad (100)$$

and (neglecting $\partial \bar{n} / \partial \xi$ and $\partial \bar{n} / \partial \eta$)

$$\begin{aligned} I_S(\xi, \eta) = & -\frac{1}{2\pi} \left\{ -\bar{r} \times \bar{a}_1 \cdot \bar{n} \frac{1}{|\bar{a}_1|} \sinh^{-1} \left(\frac{\bar{r} \cdot \bar{a}_1}{|\bar{r} \times \bar{a}_1|} \right) \right. \\ & + \bar{r} \times \bar{a}_2 \cdot \bar{n} \frac{1}{|\bar{a}_2|} \sinh^{-1} \left(\frac{\bar{r} \cdot \bar{a}_2}{|\bar{r} \times \bar{a}_2|} \right) \\ & \left. + \bar{r} \cdot \bar{p} \tan_p^{-1} \left(\frac{\bar{r} \times \bar{a}_1 \cdot \bar{r} \times \bar{a}_2}{|\bar{r}| |\bar{r} \cdot \bar{a}_1 \times \bar{a}_2|} \right) \right\} \quad (101) \end{aligned}$$

where

$$\bar{r}(\xi, \eta) = \bar{p} - \bar{p}_h = \bar{p}_0 + \xi \bar{p}_1 + \eta \bar{p}_2 + \xi \eta \bar{p}_3 - \bar{p}_h \quad (102)$$

$$\bar{a}_1(\xi, \eta) = \partial \bar{r} / \partial \xi = \bar{p}_1 + \eta \bar{p}_3 \quad (103)$$

$$\bar{a}_2(\xi, \eta) = \partial \bar{r} / \partial \eta = \bar{p}_2 + \xi \bar{p}_3 \quad (104)$$

$$\bar{n}(\xi, \eta) = (\bar{a}_1 \times \bar{a}_2) / |\bar{a}_1 \times \bar{a}_2| \quad (105)$$

similar expressions are used for w_{hk} .

ORIGINAL PAGE IS
OF POOR QUALITY

SECTION 8

DETERMINATION OF FLIGHT CONDITIONS

The effects of the aerodynamic interference of the rotor wake and the aircraft on the stability and control characteristics of the tilt rotor aircraft are expected to be important. In particular, the effect on the longitudinal trim of the aircraft, especially through the transition and conversion modes, may be significant. In the trim condition, the total longitudinal forces and moments acting on the aircraft must be in equilibrium, that is, they must sum to zero. For a given mast angle, flap setting, and stabilizer incidence, the aircraft is trimmed by appropriate displacement of the longitudinal and collective pitch controls.

Because of the complexity of the forces and moments on proprotor aircraft, an iterative solution is usually required, in which the displacements of the controls required for trim are first estimated, and then incrementally changed to achieve force and moment equilibrium of the aircraft within some acceptable range, say ± 50 lb or ft-lb from zero. However, for the purpose of the present study, an alternate method of determining the trim conditions in the presence of aerodynamic interference was selected. This method was based on incremental changes from a standard case in order to estimate the values of collective pitch and rotor incidence for other flight cases of particular interest. The standard case was based on wind tunnel data of a tilt rotor aircraft in the trimmed condition.

Estimates of collective pitch and rotor incidence under various conditions of weight, altitude and flight path angle are made through an incremental analysis based on this standard case (Subsection 8.2). This involves calculating the increments in vehicle drag and rotor thrust coefficient based on an assumed vehicle drag polar, and the rotor blade model. The rotor blade model is based on the application of classical

RECEDING PAGE BLANK HAVE BEEN

blade element theory to compute the thrust and flapping motion of a rotor with large inflow (Subsection 8.1).

8.1 APPROXIMATE ANALYSIS OF THE THRUST AND FLAPPING MOTION OF ROTORS WITH LARGE INFLOW

Applying classical blade element theory to the section of rotor blade shown in Figure 13, neglecting the effect of profile drag, and assuming that the angle of attack of the blade element can be represented by its sine, and that the pitch of a

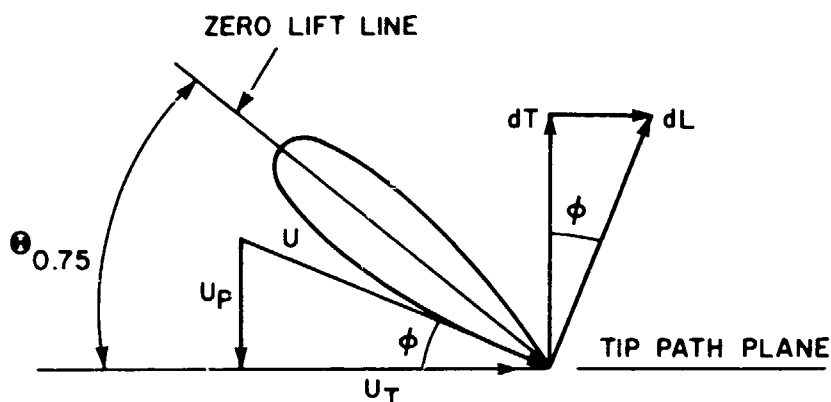


Figure 13. Typical Blade Element at Radius, $0.75R$.

twisted blade can be represented by its value at three-quarter radius, the rotor thrust perpendicular to the tip path plane can be expressed as:

$$T = \frac{b}{2\pi} \int_0^{2\pi} \int_0^R \frac{\rho}{2} U^2 a c \sin [\theta_{0.75} - \phi] \cos \phi dr d\psi \quad (106)$$

where

b = number of blades

ρ = air density

U = resultant air velocity = $[U_P^2 + U_T^2]^{1/2}$

$U_P = \lambda \Omega R + \mu \Omega R \beta_0 \cos \psi$

$U_T = \Omega r + \mu \Omega R \sin \psi$

$$\lambda = \text{inflow ratio} = \frac{U_{\infty} \sin i + v}{\Omega R}$$

$$\mu = \text{advance ratio} = \frac{U_{\infty} \cos i}{\Omega R}$$

i = rotor incidence angle

$$v = \text{rotor induced velocity (assumed constant)} = \frac{C_T}{2 [\mu^2 + \lambda^2]^{1/2}}$$

$$C_T = \text{rotor thrust coefficient} = \frac{T}{\rho \pi R^2 (\Omega R)^2}$$

Ω = rotor rotational speed

R = rotor radius

β_o = blade coning angle

r = radius to blade element

a = blade lift curve slope

c = blade chord, assumed constant

$\Theta_{0.75}$ = blade pitch at three-quarter radius

$$= \Theta_{0.75} + \theta_{1c} \cos \psi + \theta_{1s} \sin \psi$$

$\Theta_{0.75}$ = blade collective pitch at three-quarter radius

θ_{1c} = blade lateral cyclic pitch

θ_{1s} = blade longitudinal cyclic pitch

ψ = blade azimuth angle

$$\phi = \text{blade inflow angle} = \sin^{-1} \frac{U_P}{U} \text{ or } \cos^{-1} \frac{U_T}{U}$$

Expanding and substituting for $\cos \phi$ and $\sin \phi$,

$$T = \frac{b}{2\pi} \int_0^{2\pi} \int_0^R \frac{\rho}{2} ac \left[U_T^2 \sin \Theta_{0.75} - U_P U_T \cos \Theta_{0.75} \right] dr d\psi \quad (107)$$

Nondimensionalizing the thrust expression by $\rho \pi R^2 (\Omega R)^2$, and integrating, the thrust coefficient is obtained:

$$C_T = \frac{\sigma a}{2} \left[\frac{\sin \theta_{0.75}}{3} \left(1 + \frac{3}{2} \mu^2 \right) + \frac{\mu \theta_{1s}}{2} (\cos \theta_{0.75} + \lambda \sin \theta_{0.75}) - \frac{\lambda}{2} \cos \theta_{0.75} \right] \quad (108)$$

where the solidity, σ , of a rotor is defined as the ratio of the total blade area to the rotor disk area. For rectangular blades,

$$\sigma = \frac{bcR}{\pi R^2} = \frac{bc}{\pi R} \quad (109)$$

All quantities are referred to the tip path plane.

Applying blade element theory in the same manner as for thrust, and assuming negligible spring restraint about the flapping hinge, the equation for equilibrium of a single blade about the flapping hinge is

$$I_1 \Omega^2 \beta_o = \int_0^R \frac{\rho}{2} U^2 a \left[U_T^2 \sin \theta_{0.75} - U_p U_T \cos \theta_{0.75} \right] dr \quad (110)$$

where I_1 = blade moment of inertia about flapping hinge.

Nondimensionalizing the flapping expression by $I_1 \Omega^2$, integrating, and equating like harmonics, the equilibrium blade coning angle and cyclic pitch with respect to the tip path plane are obtained:

$$\beta_o = \frac{\gamma}{2} \left[\frac{\sin \theta_{0.75}}{4} (1 + \mu^2) + \frac{\mu \theta_{1s}}{3} \left(\cos \theta_{0.75} + \frac{3}{4} \lambda \sin \theta_{0.75} \right) - \frac{\lambda}{3} \cos \theta_{0.75} \right] \quad (111)$$

$$\theta_{1c} = \frac{4/3 \mu \beta_o}{1 + \frac{1}{2} \mu^2 + \frac{4}{3} \lambda \tan \theta_{0.75}} \quad (112)$$

$$\theta_{1s} = \frac{-\frac{8}{3} \mu \left[\tan \theta_{0.75} - \frac{3}{4} \lambda \right]}{1 + \frac{3}{2} \mu^2 + \frac{4}{3} \lambda \tan \theta_{0.75}} \quad (113)$$

In determining the equilibrium of the aircraft as a whole, it is necessary to determine the flapping of the blades with respect to the hub plane. It can be shown by an analysis similar to that described above, that the following relationships exist:

$$\theta_{1c_{HP}} - \frac{1}{1 + \frac{\frac{4}{3} \lambda \tan \theta_{0.75}}{1 + \frac{1}{2} \mu^2}} \beta_{1s_{HP}} = \theta_{1c} \quad (114)$$

$$\theta_{1s_{HP}} + \frac{1}{1 + \frac{\frac{4}{3} \lambda \tan \theta_{0.75}}{1 + \frac{3}{2} \mu^2}} \beta_{1c_{HP}} = \theta_{1s} \quad (115)$$

where

$\beta_{1s_{HP}}$ = blade lateral flapping angle with respect to hub plane

$\theta_{1c_{HP}}$ = blade lateral cyclic pitch angle with respect to hub plane

$\beta_{1c_{HP}}$ = blade longitudinal flapping angle with respect to hub plane

$\theta_{1s_{HP}}$ = blade longitudinal cyclic pitch angle with respect to hub plane

and all other quantities are referred to the tip path plane.

ORIGINAL PAGE IS
OF POOR QUALITY

8.2 SELECTION OF FLIGHT CASES FOR ANALYSIS INCLUDING ESTIMATED VALUES OF COLLECTIVE PITCH AND ROTOR INCIDENCE FOR TRIM

In studying aerodynamic interference effects on tilt rotor aircraft, it is first necessary to establish trim conditions for the various flight cases of interest. Parameters to be varied are gross weight, altitude, climb angle, and center-of-gravity position.

During flight, a typical proprotor aircraft has three distinctly different modes of operation:

- Helicopter mode.
- Conversion mode.
- Cruise mode.

Each of these modes requires a different configuration of the aircraft, i.e., a different range of mast angles for the rotors. Of particular interest is the conversion mode, since the most significant interference between the rotor wakes and the horizontal tailplane occurs during this mode.

A typical flight profile for a typical tilt rotor aircraft, the NASA/Army/Bell XV-15, is shown in Figure 19 of Reference 48 for the standard case of 13,000 lb gross weight, trimmed level flight at sea level, and aft center of gravity. Figures 14, 15, 16, and 17 show the variation of rotor speed, rotor attitude, rotor thrust coefficient, and blade collective pitch with forward speed for this standard case as given in the reference. Note that rotor incidence is related to rotor attitude by the relation

$$i = \frac{\pi}{2} - \alpha_R \quad (116)$$

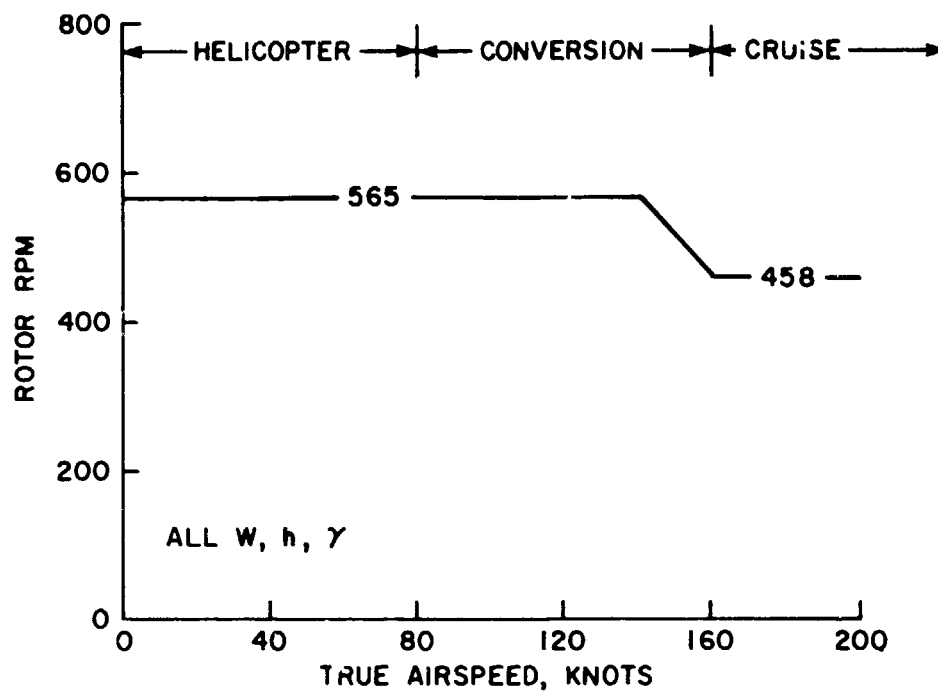


Figure 14. Rotor rpm versus Airspeed.

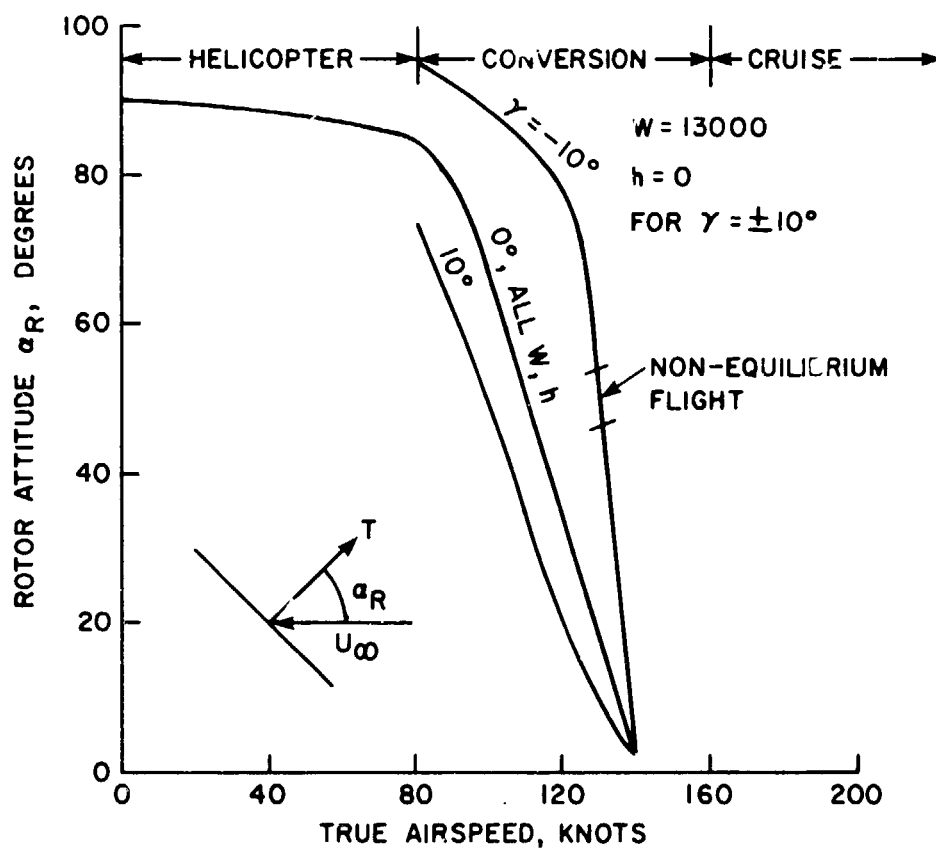


Figure 15. Rotor Attitude versus Airspeed.

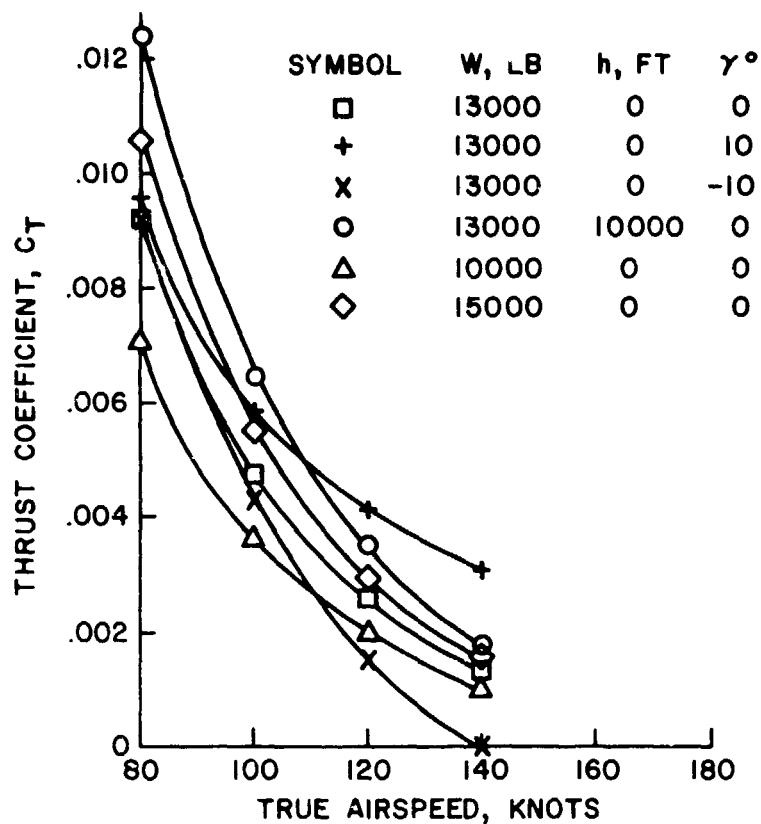


Figure 16. Rotor Thrust Coefficient versus Airspeed.

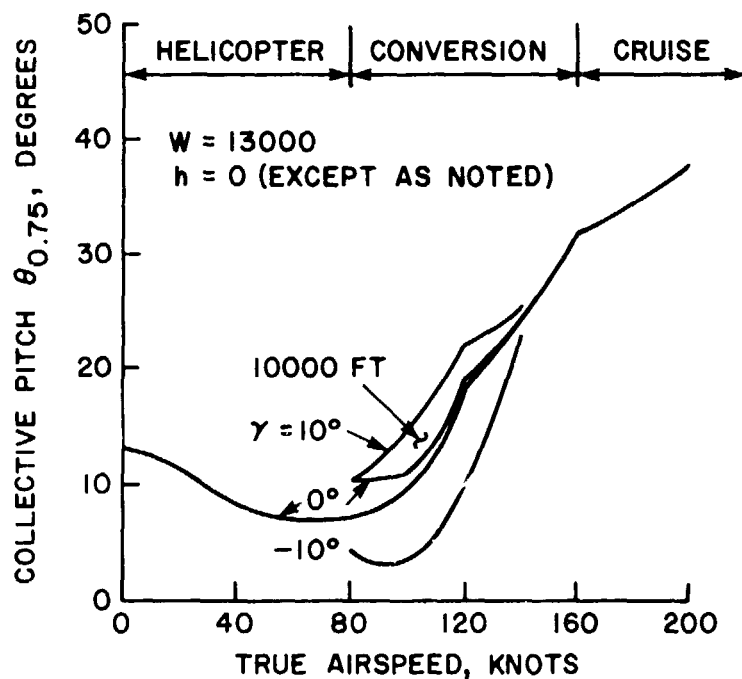


Figure 17. Rotor Collective Pitch versus Airspeed.

It is desired to estimate the values of collective pitch and rotor incidence for other flight cases of particular interest in the study of aerodynamic interference effects. This can be done on an incremental basis with respect to the standard case.

Consider the effect of varying gross weight, altitude, and climb angle on rotor attitude and collective pitch:

- Gross Weight

During conversion in the standard flight case, it is assumed that the aircraft is operated near its maximum lift-drag ratio and with a lift coefficient near unity. These conditions imply a drag polar of the form

$$C_D = a (1 + C_L^2) \quad (117)$$

Now consider the change of drag coefficient resulting from the change of lift required by a change in gross weight:

$$\begin{aligned} C_D + \Delta C_D &= a \left[1 + (C_L + \Delta C_L)^2 \right] \\ &= a \left[1 + (C_L^2 + 2C_L \Delta C_L + \Delta C_L^2) \right] \end{aligned} \quad (118)$$

$$\approx a(1 + C_L^2) + 2aC_L \Delta C_L$$

$$\therefore \Delta C_D \approx 2aC_L \Delta C_L \quad (119)$$

$$\frac{\Delta C_D}{C_D} \approx \frac{2C_L^2}{1 + C_L^2} \frac{\Delta C_L}{C_L} \quad (120)$$

It is seen that for original lift coefficients close to unity, the percent change in drag coefficient is nearly equal to the percent change in lift coefficient. Therefore, to maintain equilibrium along the flight path, only a change in thrust, i.e., collective pitch, is required. No change in rotor attitude is necessary.

The required change in thrust coefficient is

$$\Delta C_T = C_T \left(\frac{W_2}{W_1} - 1 \right) \quad (121)$$

- Altitude

Consider the change of drag coefficient resulting from the change of lift coefficient required by a change in altitude, i.e., air density. As for changes in gross weight, the percent change in drag is nearly equal to the percent change in lift. Therefore, only a change in thrust, i.e., collective pitch, is required:

$$\Delta C_T = C_T \left(\frac{\rho_1}{\rho_2} - 1 \right) \quad (122)$$

- Climb Angle

During climb or descent at angle γ to the horizontal, there is an incremental drag force given by

$$\Delta D = W \sin \gamma \quad (123)$$

where

W = aircraft gross weight

γ = angle of climb (+) or descent (-)

Since there is only a negligible change in lift required during climb, a change in rotor attitude is required to maintain equilibrium along the flight path. In addition, a change in thrust, i.e., collective pitch, is required.

Consider the requirements for equilibrium along the flight path. The incremental component of thrust coefficient along the flight path is given by

$$\Delta C_X = (C_T + \Delta C_T) \cos (\alpha_R - \Delta \alpha_R) - C_T \cos \alpha_R \quad (124)$$

The corresponding incremental component of thrust coefficient perpendicular to the flight path is given by

$$\Delta C_Z = (C_T + \Delta C_T) \sin (\alpha_R - \Delta \alpha_R) - C_T \sin \alpha_R \quad (125)$$

Since the change in C_Z is negligible, set $\Delta C_Z = 0$:

$$\therefore C_T + \Delta C_T = \frac{C_T \sin \alpha_R}{\sin (\alpha_R - \Delta \alpha_R)} \quad (126)$$

$$\Delta C_T = C_T \left[\frac{\sin \alpha_R}{\sin (\alpha_R - \Delta \alpha_R)} - 1 \right] \quad (127)$$

Substituting into the expression for ΔC_X :

$$C_X = C_T \frac{\sin \alpha_R}{\tan (\alpha_R - \Delta \alpha_R)} - C_T \cos \alpha_R \quad (128)$$

$$\therefore \tan (\alpha_R - \Delta \alpha_R) = \frac{\sin \alpha_R}{\frac{C_X}{C_T} + \cos \alpha_R} \quad (129)$$

ORIGINAL PAGE IS
OF POOR QUALITY

where

$$\Delta C_X = \frac{W \sin \gamma}{\rho \pi R^2 (\Omega R)^2} \quad (130)$$

Equation (129) can be solved for $(\alpha_R - \Delta \alpha_R)$ and then Equation (126) yields ΔC_T .

The change in collective pitch $\Delta \theta_{0.75}$ required by a change in thrust coefficient ΔC_T can be obtained from the thrust expression (Equation (108)).

$$\begin{aligned} C_T = \frac{\sigma a}{2} & \left[\frac{\sin \theta_{0.75}}{3} \left(1 + \frac{3}{2} \mu^2 \right) \right. \\ & + \frac{1}{2} \mu \theta_{1s} (\cos \theta_{0.75} + \lambda \sin \theta_{0.75}) \\ & \left. - \frac{\lambda}{2} \cos \theta_{0.75} \right] \end{aligned} \quad (131)$$

Setting $C_T = C_T + \Delta C_T$ and $\theta_{0.75} = \theta_{0.75} + \Delta \theta_{0.75}$, and assuming small $\Delta \theta_{0.75}$, the incremental thrust coefficient is

$$\begin{aligned} \Delta C_T \approx \frac{\sigma a}{2} & \left[\frac{\cos \theta_{0.75}}{3} \left(1 + \frac{3}{2} \mu^2 \right) \right. \\ & \left. + \frac{\sin \theta_{0.75}}{2} \lambda \right] \Delta \theta_{0.75} - \frac{\sigma a}{4} \Delta \lambda \cos \theta_{0.75} \end{aligned} \quad (132)$$

and the required relation between ΔC_T and $\Delta \theta_{0.75}$ is obtained.

Equations (121), (122), (127), and (129) were applied to the calculation of the required thrust coefficients and rotor attitudes in the following equilibrium flight conditions:

- $W = 10,000, 13,000$ and $15,000$ lb, $\gamma = 0^\circ$, $h = 0$ ft
- $W = 13,000$ lb, $\gamma = 0^\circ$, $h = 10,000$ ft
- $W = 13,000$ lb, $\gamma = \pm 10^\circ$, $h = 0$

The results are shown in Figure 15 and 16.

Equation (132) was used to calculate the required values of collective pitch for the various flight conditions. Results were shown in Figure 17 and in Table 5 below:

Table 5. Trim Values of Rotor Attitude and Collective Pitch.

W (lb)	γ (deg)	h (ft)	V (kt)	α_R (deg)	δ (deg)
13000	0	0	80	84.4	7.35
			100	66.3	9.57
			120	35.6	18.2
			140	1.8	24.2
13000	10	0	80	73.9	10.4
			100	49.7	14.9
			120	21.2	22.0
			140	1.8	25.5
13000	-10	0	80	95.3	4.53
			100	88.2	3.15
			120	78.1	10.0
			140	1.8	23.0
13000	0	10000	80	84.4	10.1
			100	66.3	10.9
			120	35.6	18.9
			140	1.8	24.6

ORIGINAL PAGE IS
OF POOR QUALITY

SECTION 9

RESULTS

The formulation presented in Sections 6 and 7 was incorporated into a computer program to investigate the aerodynamic effects of tilt rotor aircraft. In particular, the problem of the rotor wake interaction effects for the XV-15 aircraft at various flight conditions was studied. Typical numerical results, showing the feasibility of the present method, are discussed in this section.

The geometry of the tilt rotor aircraft used is shown in Figure 18. Due to the preliminary nature of this study, the aerodynamic interference effects on the horizontal tail are assumed to be caused principally by the rotor wake, with nacelle aerodynamics contributions being of a secondary nature. Therefore, the geometry of the engine nacelles has been omitted as seen in Figure 18. Moreover, an infinite-blade rotor, i.e., actuator disk, is used.

To study the convergence of the numerical method, the case of the tilt-rotor aircraft without the aerodynamic interference effects on the tail was investigated. Specifically, a wing-tail configuration and an actuator disk were treated separately and then combined for analysis at the hover condition. Also, the problem with interference effects was demonstrated for one flight condition in the conversion mode.

9.1 CASE WITH NO INTERFERENCE

Convergence studies were conducted to identify the approximate number of aerodynamic elements required. In addition, the overall vehicle lift and pitching moment coefficients were obtained.

9.1.1 CONVERGENCE

The results of a convergence study on a wing-tail configuration at an angle of attack of 4.5° and airspeed of 80 knots without rotors are given in Figures 19, 20,

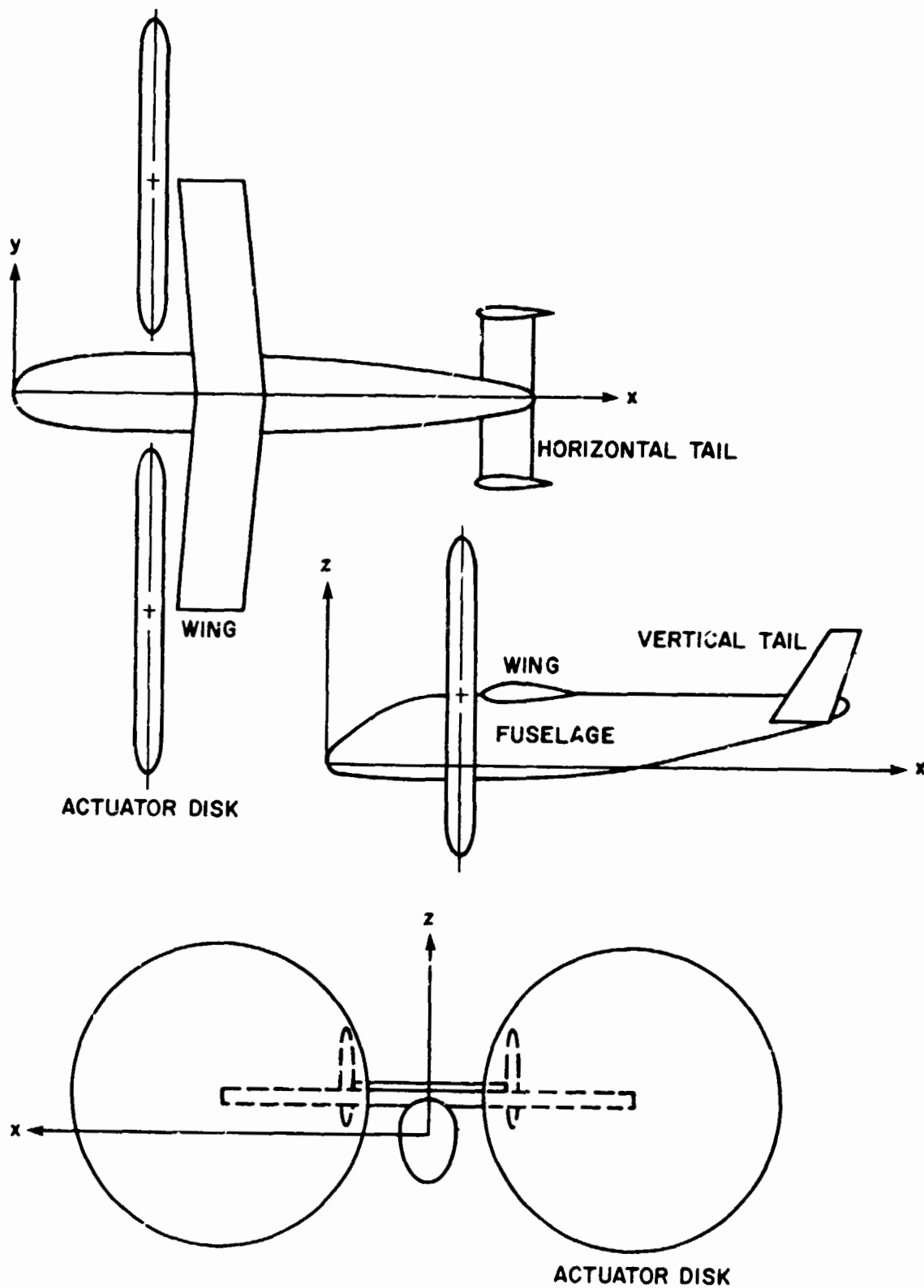


Figure 18. Geometry of a Tilt Rotor Aircraft.

ORIGINAL PAGE IS
OF POOR QUALITY

and 21. Since only longitudinal stability was considered, aircraft symmetry between the left and right sides was used. Hence, the number of elements chosen for the right-hand side of the aircraft was:

Description		Number of Elements		
Run	Symbol	Wing	Tail	Total
1	△	32	32	64
2	○	72	72	144
3	◇	98	98	196

The variation of the potential difference $\Delta \phi$ on the wing and tail sections of the tilting proprotor research aircraft at the root chord section ($2v/b = 0$) and the trailing edge ($x/c = 1$) is presented in Figure 19. In addition, the corresponding upper and lower pressure distributions as well as the lift distributions along the wing and tail root chords are shown in Figures 20 and 21, respectively. Because of the effect of the wing wake on the horizontal tail when the wing and tail are nearly coplanar, the pressure and the lift on the tail converged slowly. For this wing-tail configuration, 196 finite elements were determined to be sufficient for convergence.

A convergence study was also performed for a single actuator disk. Results for 70, 96, and 126 elements indicated that convergence was achieved for the actuator disk model with 70 elements. To avoid possible inaccuracies in the total tilt rotor aircraft problem, 96 elements were chosen for the actuator disk representation.

Results for the total vehicle problem, i.e., the wing-tail configuration with actuator disk models, are presented in Figures 22, 23, and 24. For the purpose of this study, the fuselage was assumed to contribute insignificantly to the aircraft lift and pitching moment and, therefore, it can be neglected. Similarly, the contribution of the vertical tail to the longitudinal dynamics can also be neglected. To preclude interference effects on the horizontal tail, the case of the aircraft at hover condition, that is, with

the nacelle incidence at 90° , was considered. The number of aerodynamic elements used in the study is summarized as follows:

Description		Number of Elements			
Run	Symbol	Wing	Tail	Actuator Disk	Total
1	\triangle	32	32	32	96
2	\bigcirc	50	50	96	196
3	\diamond	70	70	96	236

The potential difference, $\Delta \phi$, and pressures on the upper and lower surfaces of the wing and tail are given in Figures 22 and 23. Again, the results show that the convergence of the pressure distribution on the tail section is slow and this is due to the presence of the wing wake on the tail. In addition, the corresponding lift distribution on the wing and tail is presented in Figure 24.

9.1.2 LIFT AND PITCHING MOMENT

Comparison of the lift distributions in Figures 21 and 24 shows that the presence of the rotor produces an increase in the wing lift and a decrease in the tail lift distribution. The wing-tail configuration without prop rotor at an angle of attack of 4.5° and airspeed of 80 knots was found to yield very little lift as shown in Figure 25(a). Also, a negative pitching moment (nose down) was obtained for this configuration (Figure 25(b)). In evaluating the pitching moment about the aircraft center-of-gravity position, some basic assumptions were used which affect the accuracy of the results. The thrust vector was assumed to act through the center of gravity. In addition, only the lift and induced drag on the wing and tail were used to determine the value of the pitching moment; that is, viscous drag (drag due to skin friction) was not included in the analysis. This value can be obtained from wind tunnel tests of a tilting prop rotor research aircraft, and must be included if true trim conditions are to be calculated.

The lift coefficient for an actuator disk in hover with angular speed of 600 rpm is shown in Figure 26. The case of an actuator disk with no central core vortex, i.e., $\Delta\varphi_B = 0$, is indicated by the square symbols. This represents the presence of the vorticity shed by the rotor blades near the tip of each blade, that is, the rim wake of an actuator disk. As expected from discussion in Section 6, the results show that no lift was obtained. In order to produce lift on the actuator disk, the formulation must include a central vortex, i.e., $\Delta\varphi_B \neq 0$, and this is treated in Subsection 6.1. For this case, the vorticity shed by each blade near the blade root as well as the tip was considered. To be exact, the wake is composed of infinite vortices emanating from the tip of the blade and one additional vortex emanating from the center of the disk. The results for this case are denoted by circles in Figure 26. Furthermore, no pitching moments about the actuator disk were obtained for the hover case.

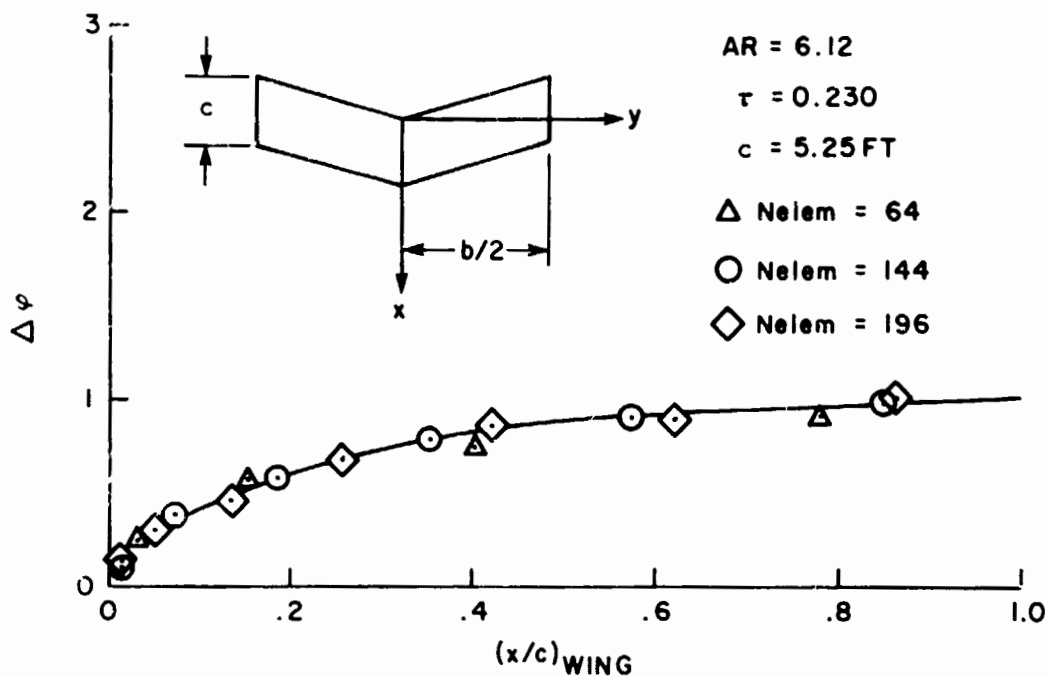
Next, the problem of the wing-tail-rotor configuration with nacelle incidence at 90° was treated. The total lift and pitching moment around the aircraft center of gravity are presented in Figure 27. For this flight configuration, the presence of the additional central vortex on the actuator disk yielded greater lift and larger nose-down pitching moment on the tilting proprotor aircraft. Again, it is emphasized that the viscous drag of the aircraft was not used in the computation.

9.2 INTERFERENCE EFFECTS

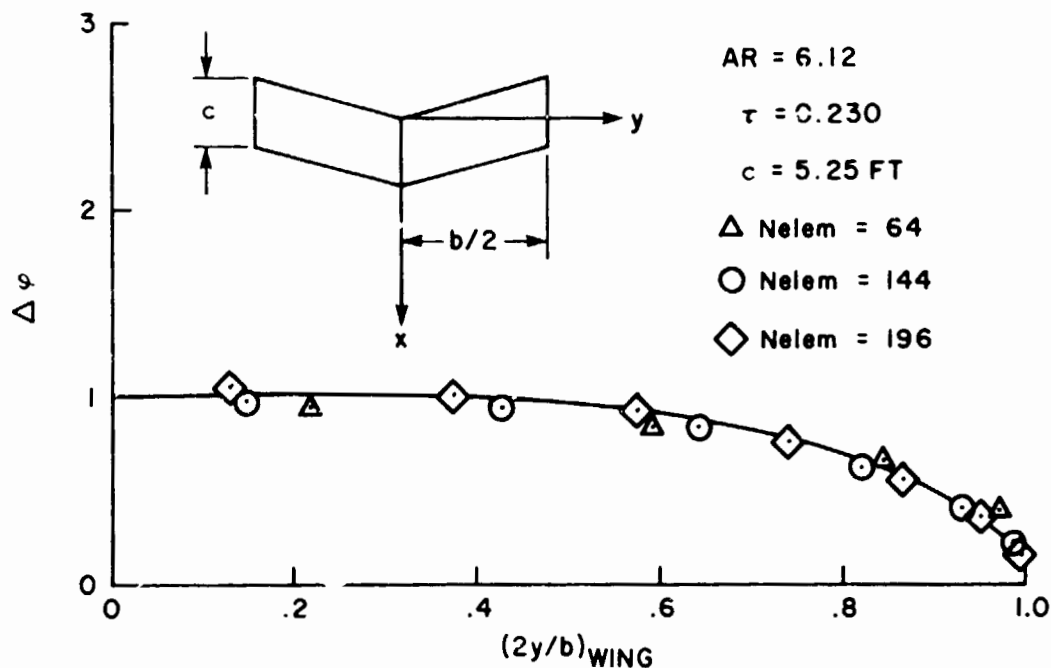
A study of the interference effects was conducted for the tilt rotor aircraft in the conversion mode of flight with nacelle incidence set at 60° , airspeed of 100 knots, rotor angular speed of 565 rpm, and a tail incidence of -1.5° . For this flight condition, the horizontal tail was imbedded in the rotor wake. The variation with angle of attack of the total vertical forces on the aircraft is given in Figure 28(a). Vertical equilibrium is achieved when the sum of the vertical forces is zero.

For this configuration, vertical equilibrium was obtained with an angle of attack setting at 2.3° . In addition, the analysis of this same problem without the implementation of the additional central vortex on the actuator disk yielded the required angle of attack setting to be about 2° .

The effect of rotor wake interference on the tilting prop rotor aircraft at this flight configuration is presented in Figures 28(b) and (c). These results are for the aircraft in the untrimmed condition and represent the change in the lift and pitching moments of the aircraft with interference effects relative to the aircraft with no rotor wake interference effects. As seen in Figure 28(b), the total aircraft lift coefficient was significantly decreased by the presence of interference effects. The reduction in lift was less for the actuator disk with a central core vortex ($C_T = .0064$). The total aircraft pitching moment in the nose down direction was significantly increased by the interference effects (Figure 28(c)). As seen in the figure, the addition of the central vortex on the actuator disk yielded a small difference in the overall pitching moment for this flight condition.



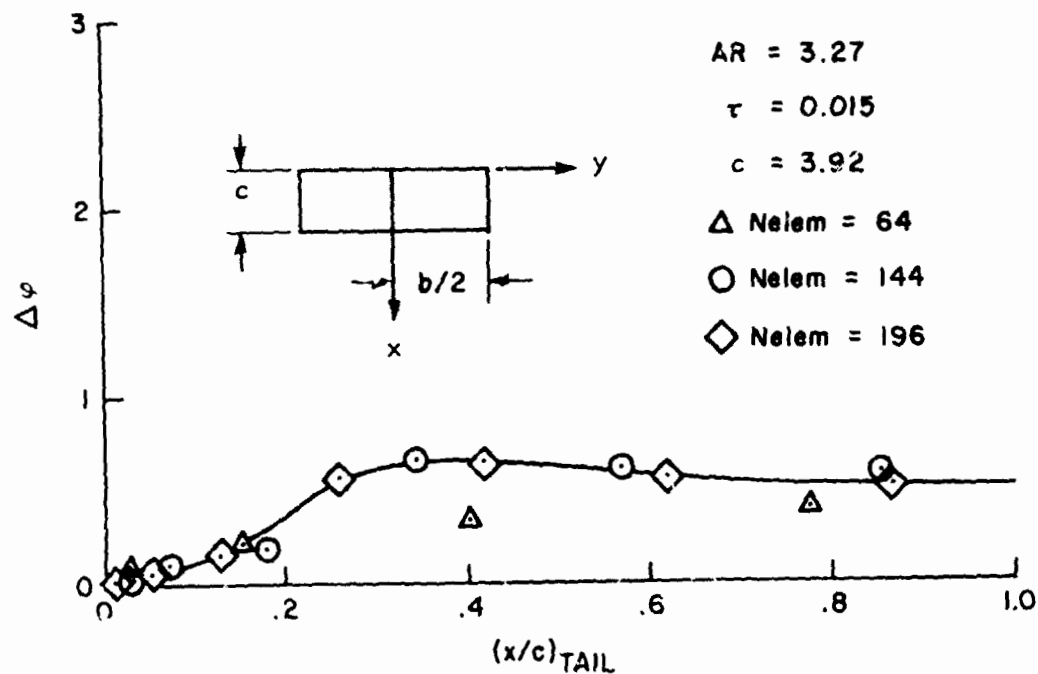
(a) Wing, Chordwise Direction, Root Chord



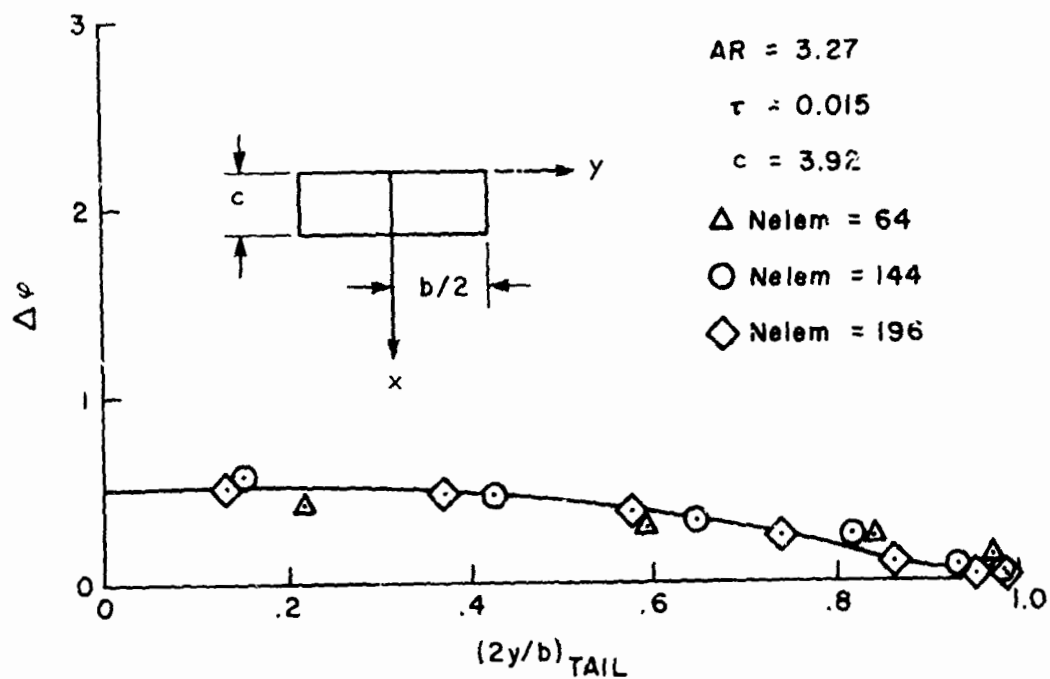
(b) Wing, Spanwise Direction, Trailing Edge

Figure 19. Potential Difference, $\Delta \phi$, Wing-Tail Combination,
 No Rotor, Airspeed = 80 kts, $\alpha = 4.5^\circ$.

ORIGINAL PAGE IS
 OF POOR QUALITY

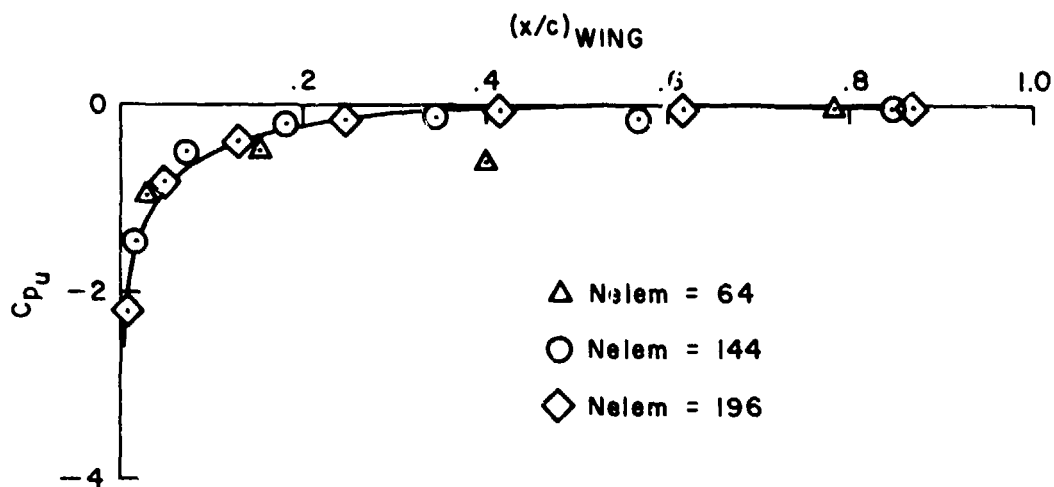


(c) Tail, Chordwise Direction, Root Chord

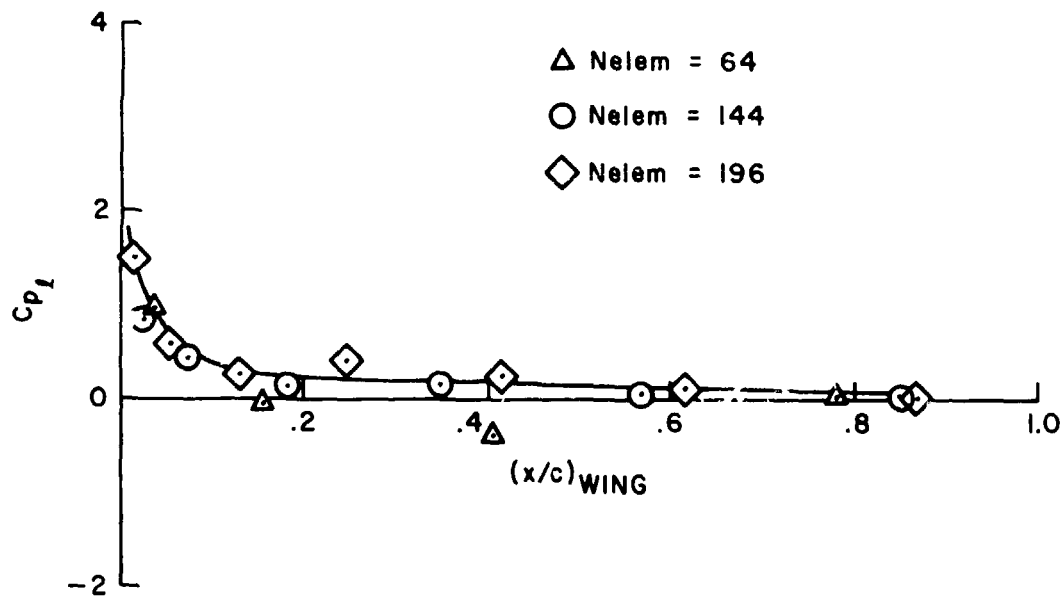


(d) Tail, Spanwise Direction, Trailing Edge

Figure 19. Potential Difference, $\Delta\phi$, Wing-Tail Combination, No Rotor, Airspeed = 80 kt, $\alpha = 4.5^\circ$. (Concluded)



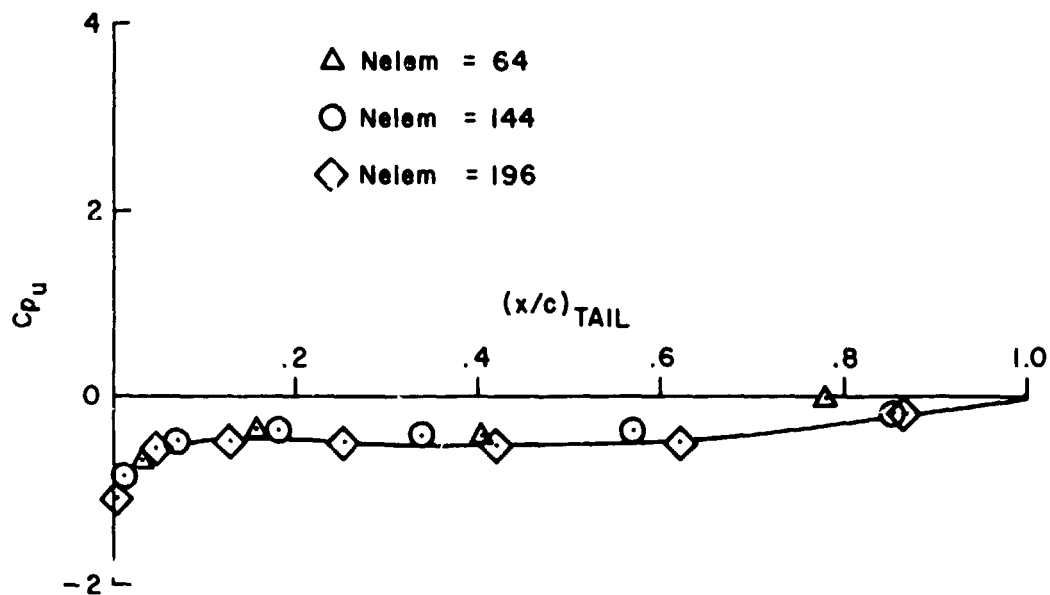
(a) Wing, Upper Surface



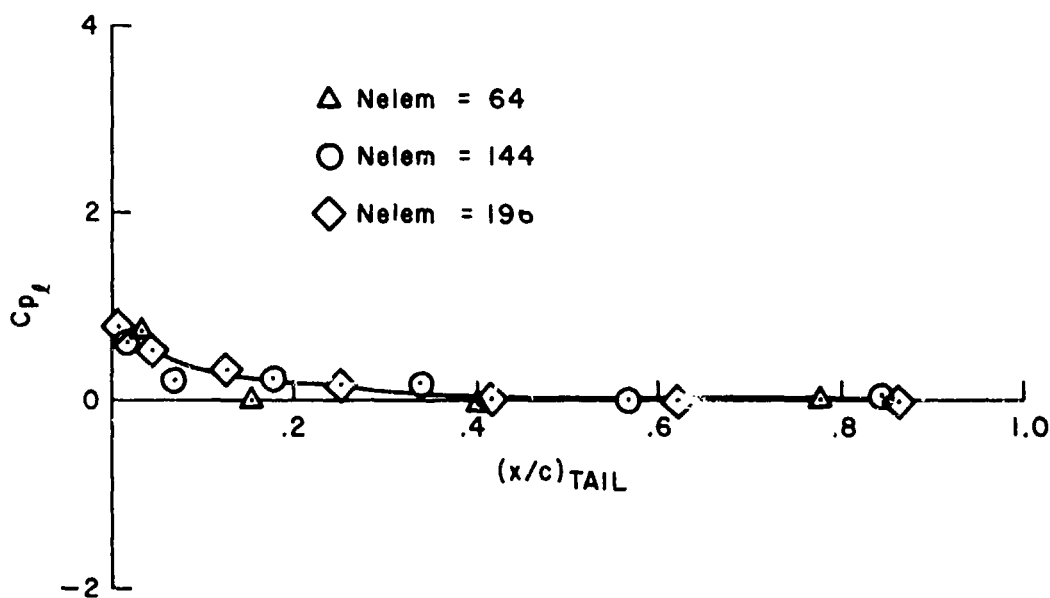
(b) Wing, Lower Surface

Figure 20. Pressure Distribution, Wing-Tail Combination,
No Rotor, Airspeed = 80 kt, $\alpha = 4.5^\circ$,
Chordwise Direction, Root Chord.

ORIGINAL PAGE IS
OF POOR QUALITY

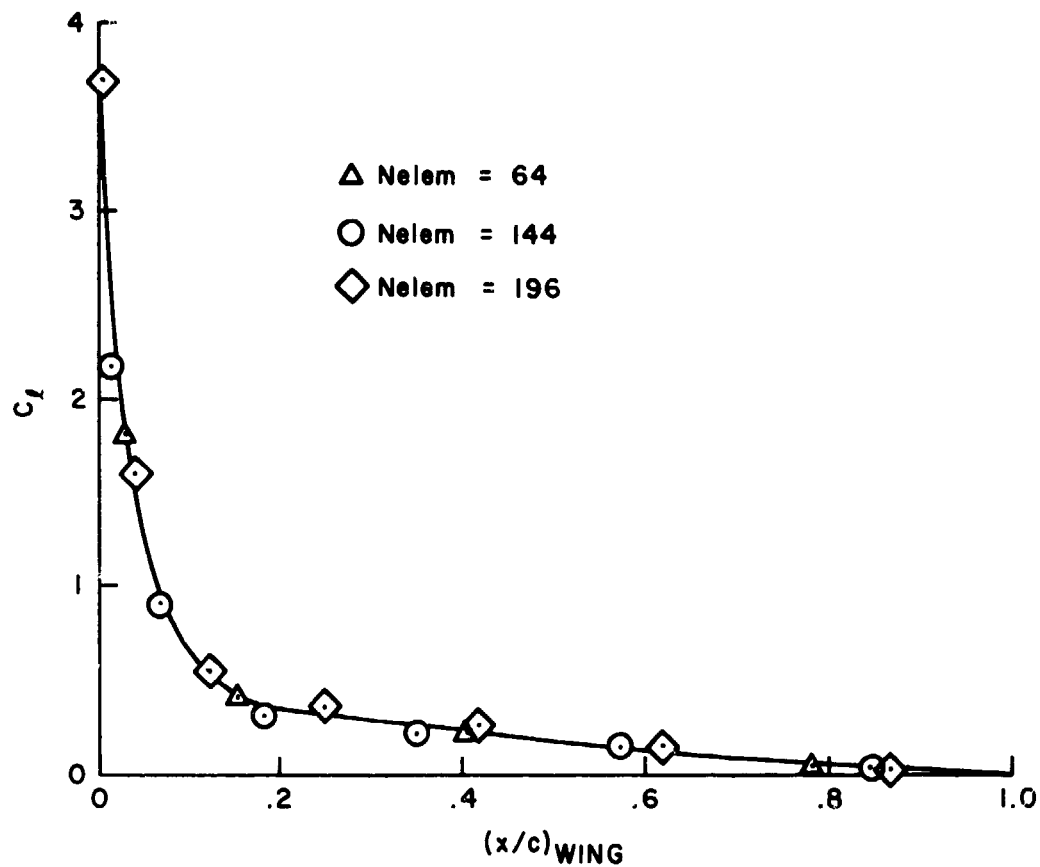


(c) Tail, Upper Surface

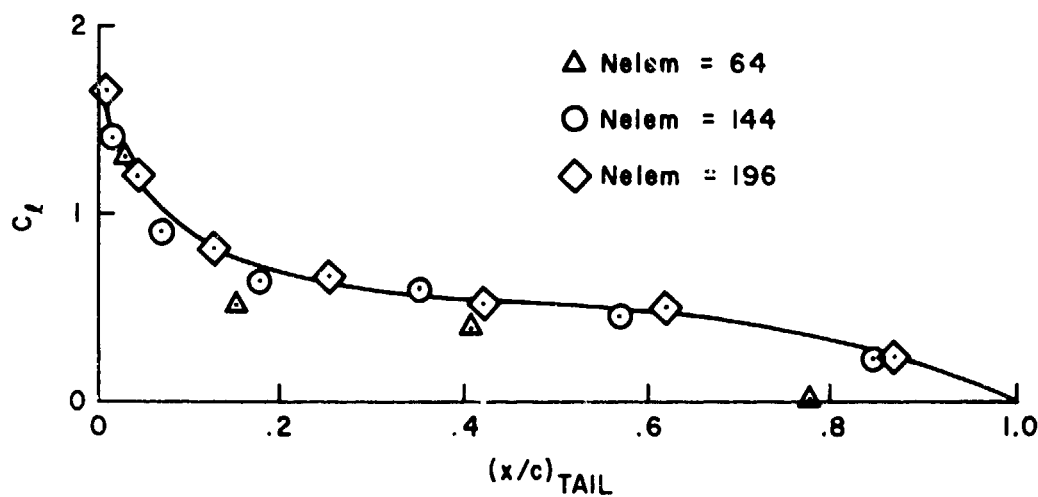


(d) Tail, Lower Surface

Figure 20. Pressure Distribution, Wing-Tail Combination,
No Rotor, Airspeed = 80 kt, $\alpha = 4.5^\circ$,
Chordwise Direction, Root Chord. (Concluded)



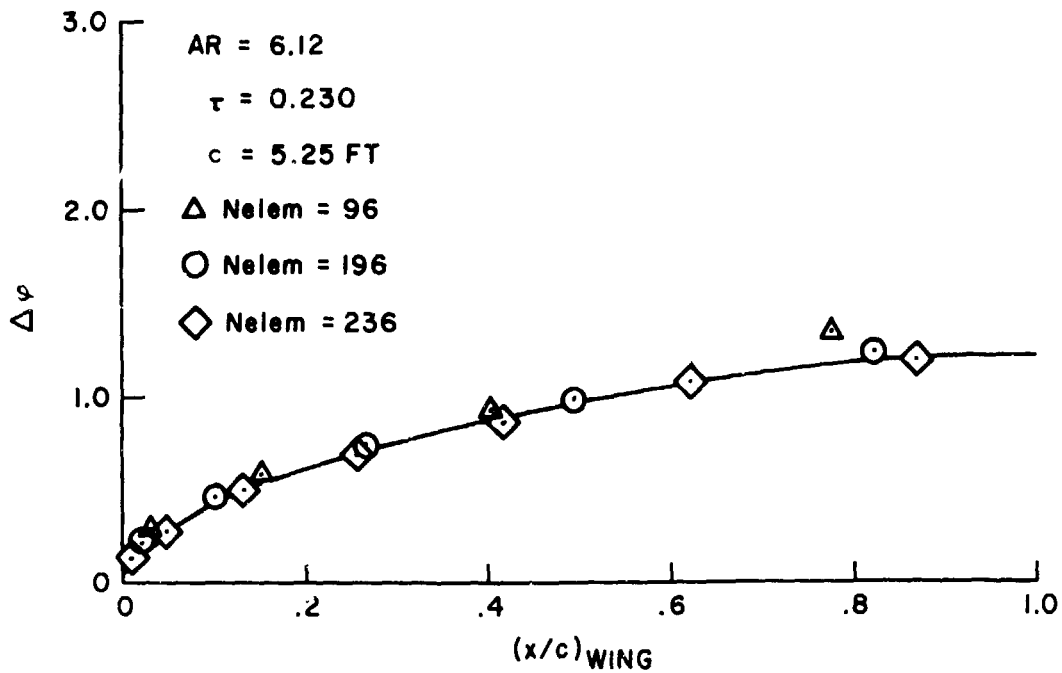
(a) Wing



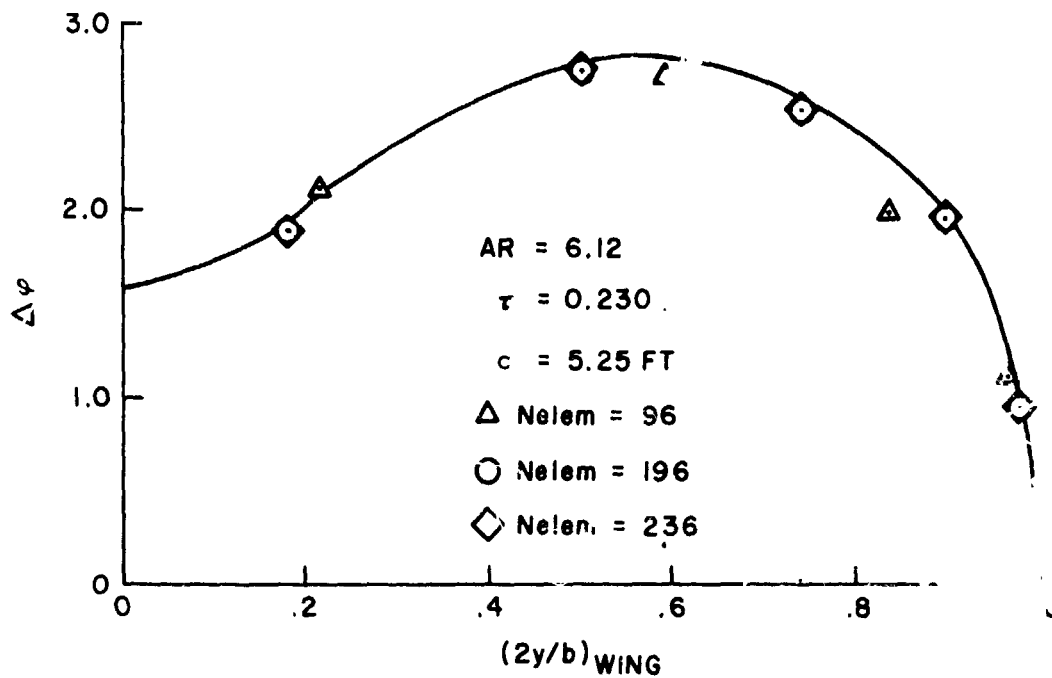
(b) Tail

Figure 21. Lift Distribution, Wing-Tail Combination, No Rotor, Airspeed = 80 kt, $\alpha = 4.5^\circ$, Chordwise Direction, Root Chord.

ORIGINAL PAGE IS
OF POOR QUALITY

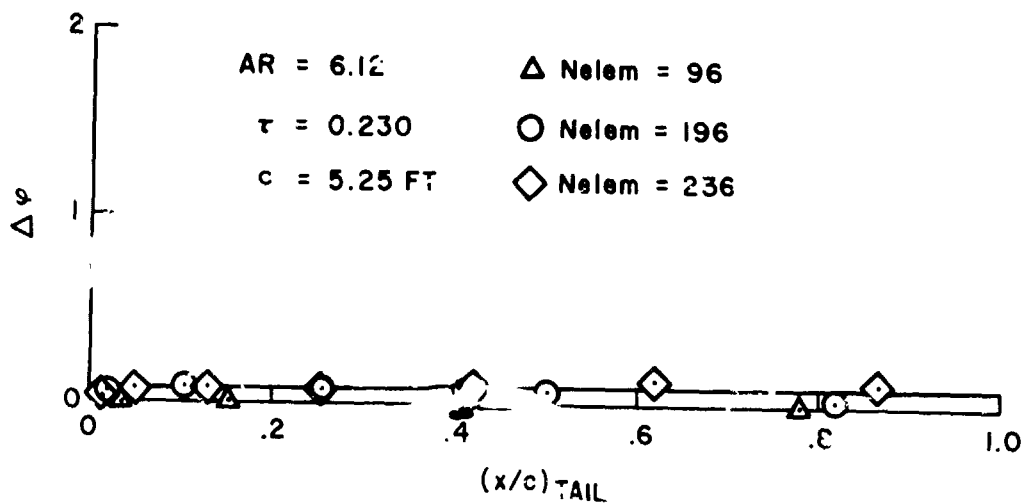


(a) Wing, Chordwise Direction, Root Chord

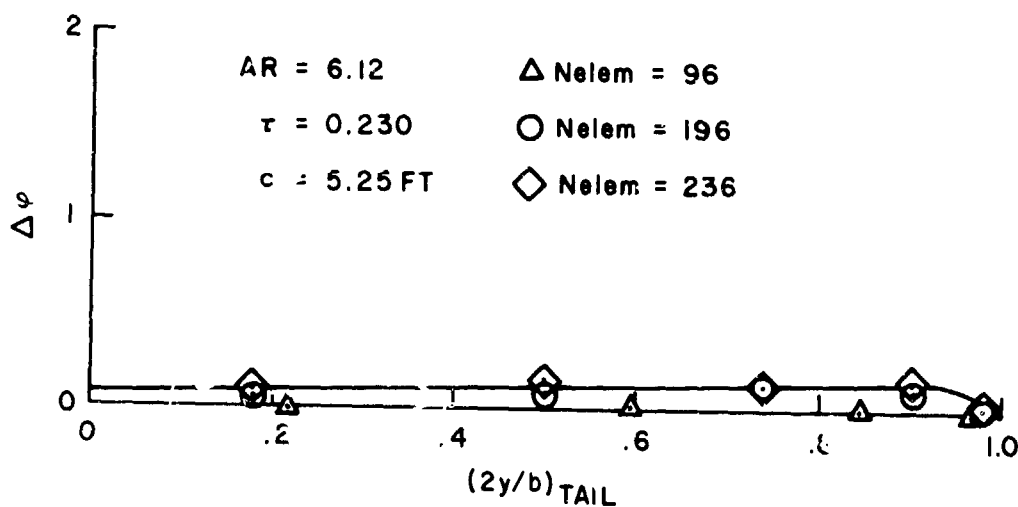


(b) Wing, Spanwise Direction, Trailing Edge

Figure 22. Potential Difference, $\Delta \phi$, Wing-Tail-Rotor Configuration, Airspeed = 80 kt, $\alpha = 4.5^\circ$, Nacelle Incidence = 90° , Angular Speed = 565 rpm.

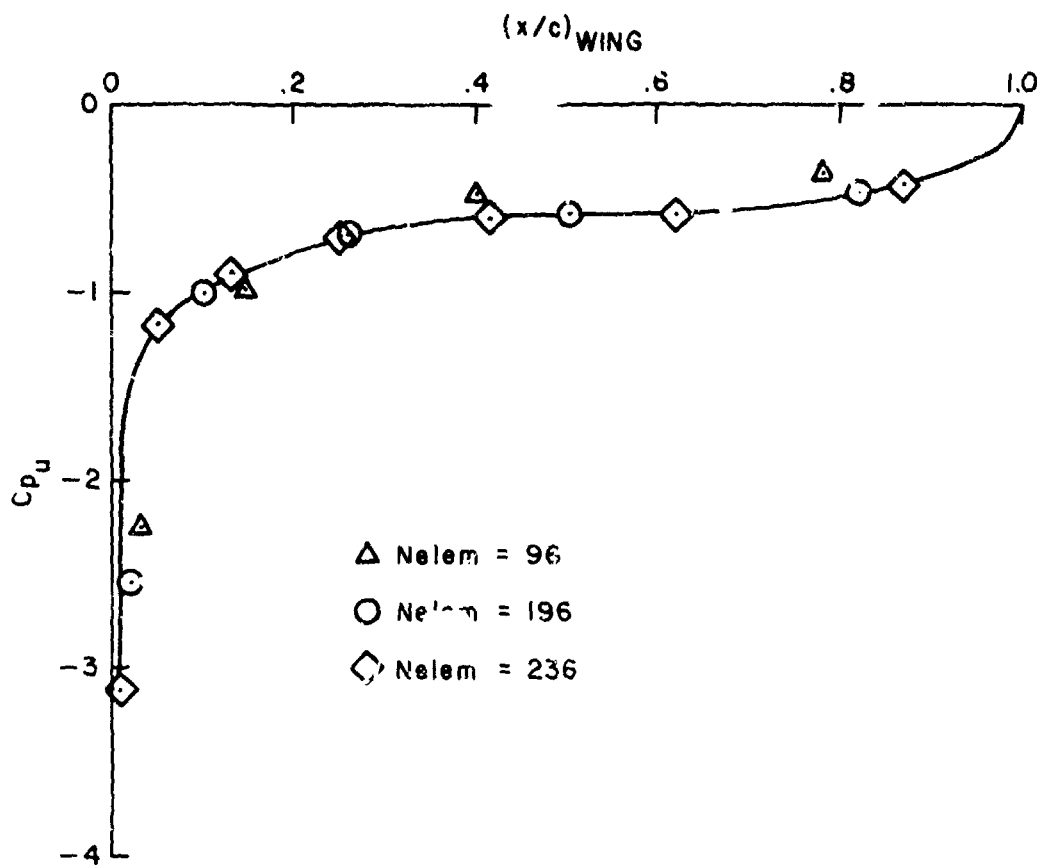


(c) Tail, Chordwise Direction, Root Chord

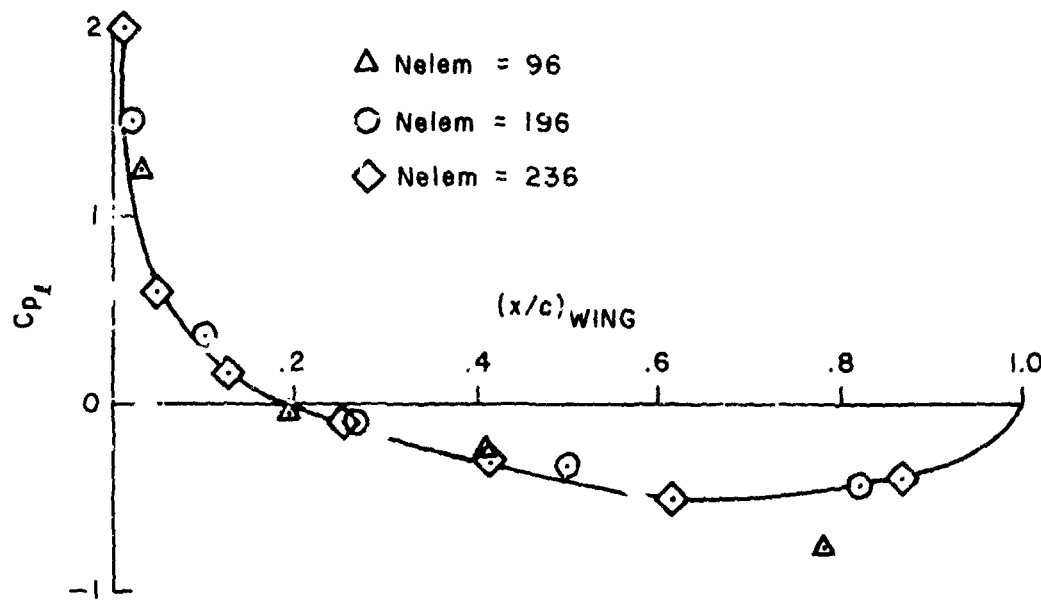


(d) Tail, Spanwise Direction, Trailing Edge

Figure 22. Potential Difference, $\Delta\phi$, Wing-Tail-Rotor Configuration,
 Airspeed = 80 kt, $\alpha = 4.5^\circ$, Nacelle Incidence = 90° ,
 Angular Speed = 565 rpm. (Concluded)

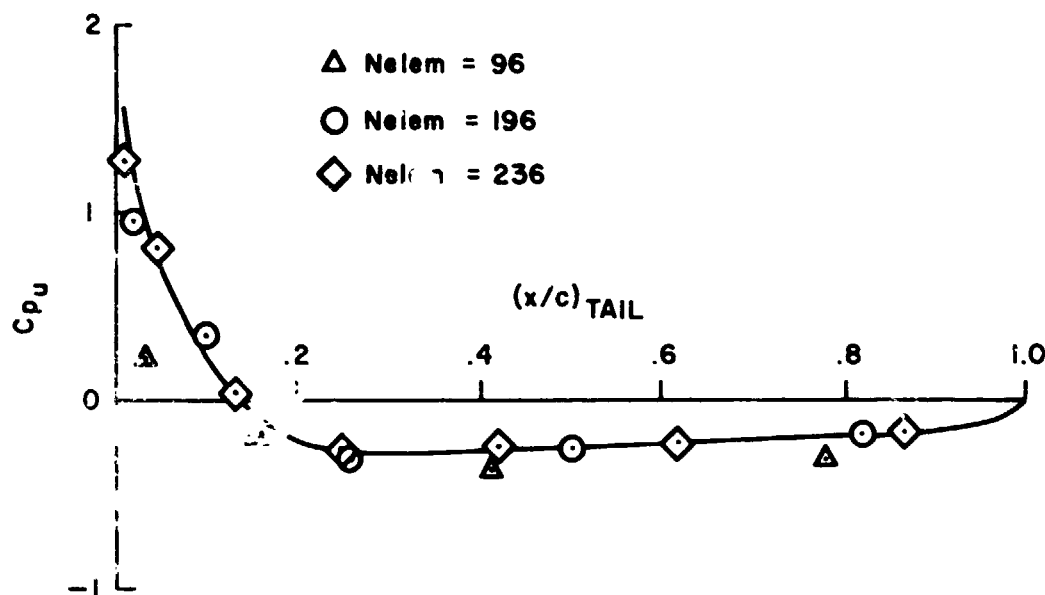


(a) Wing, Upper Surface

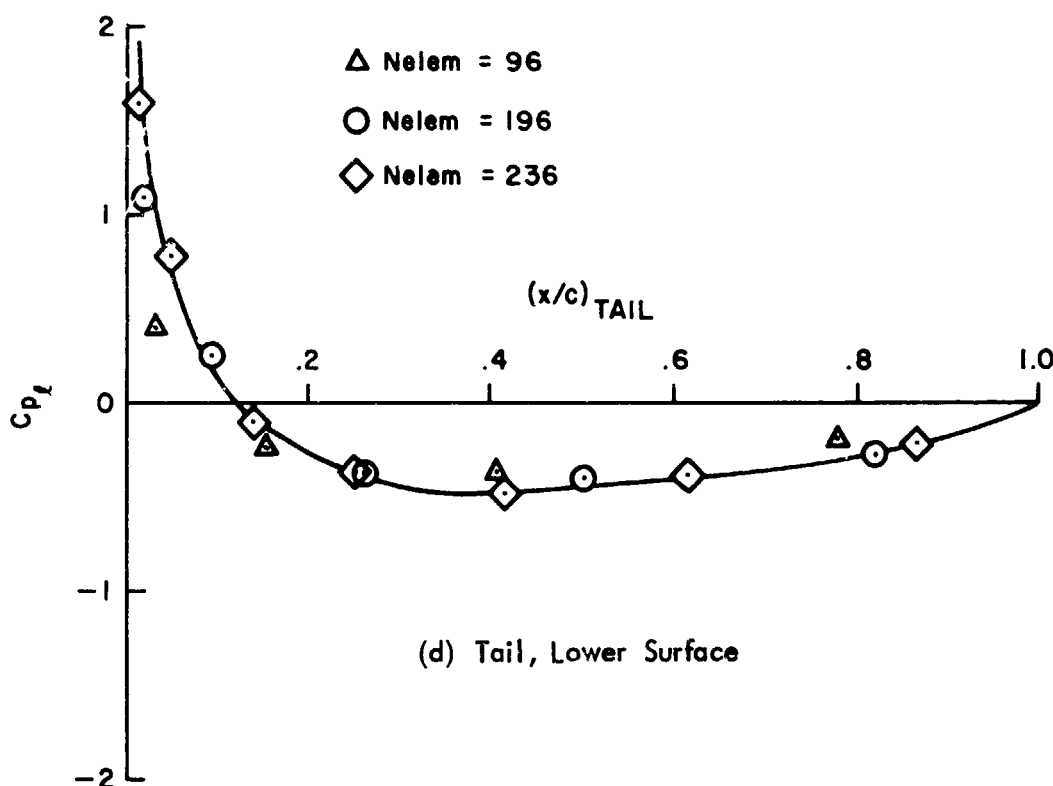


(b) Wing, Lower Surface

Figure 23. Pressure Distribution, Wing-Tail-Rotor Configuration. Airspeed = 80 kt, $\alpha = 4.5^\circ$, Nacelle Incidence = 90° , Angular Speed = 565 rpm, Chordwise Direction, Root Chord.



(c) Tail, Upper Surface



(d) Tail, Lower Surface

Figure 23. Pressure Distribution, Wing-Tail-Rotor Configuration, Airspeed = 80 kt, $\alpha = 4.5^\circ$, Nacelle Incidence = 90° , Angular Speed = 565 rpm, Chordwise Direction, Root Chord. (Conclude

ORIGINAL PAGE IS
OF POOR QUALITY

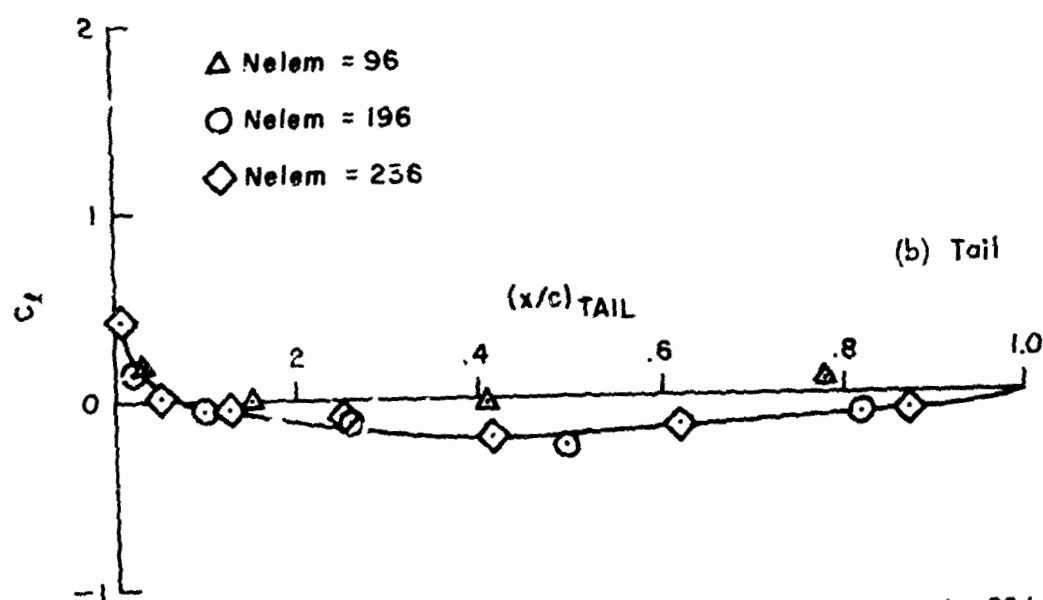
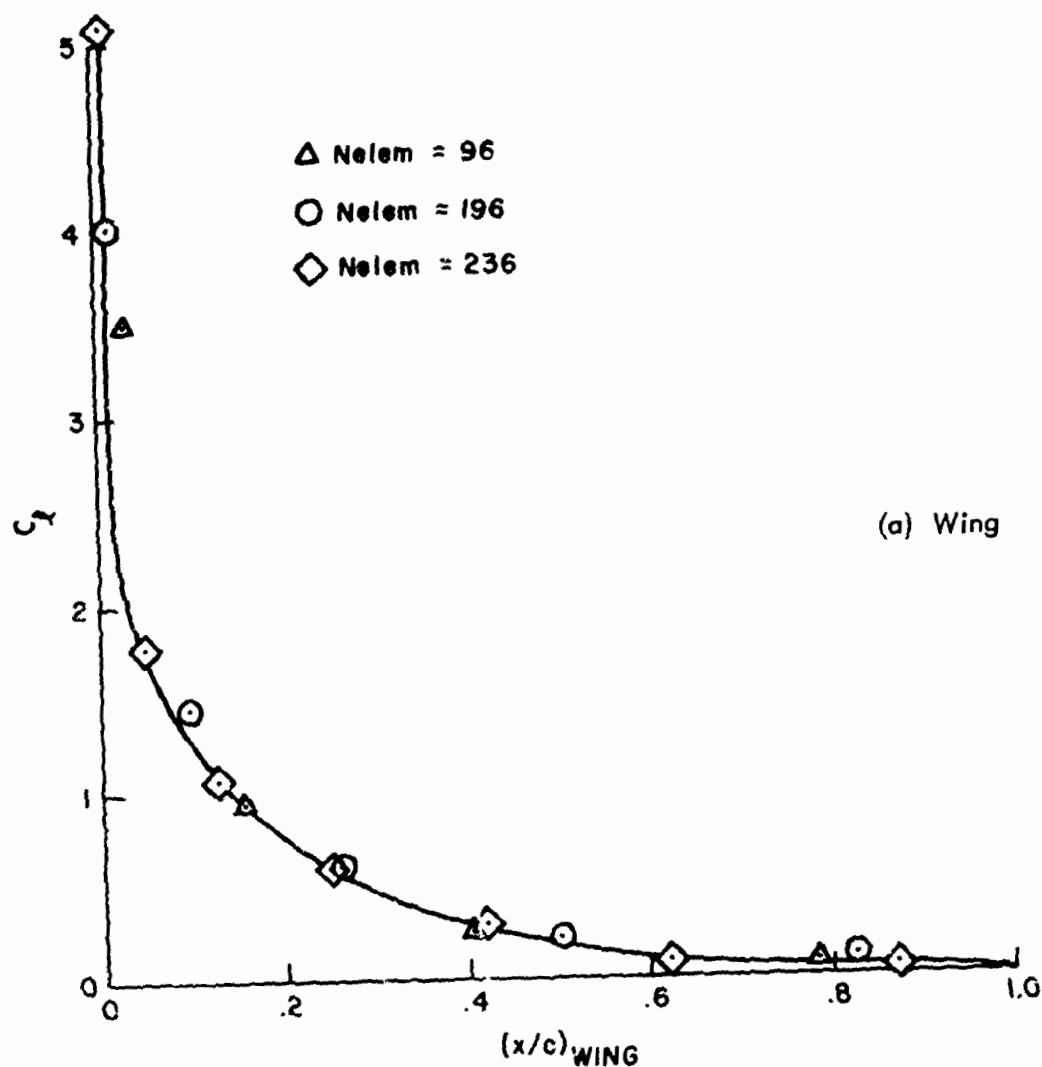
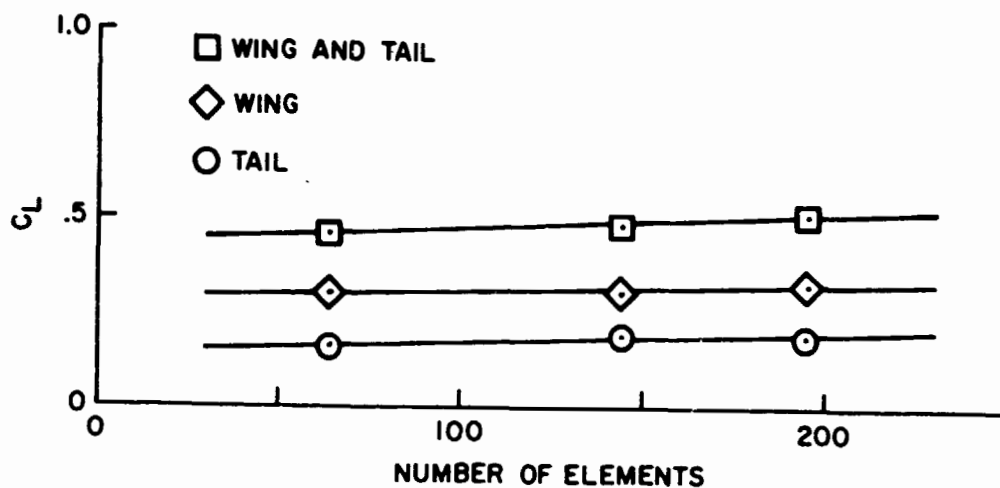
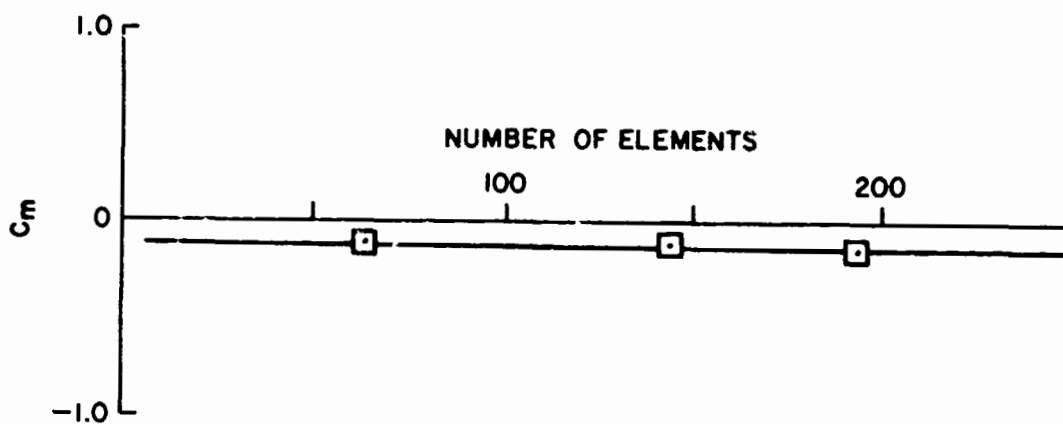


Figure 24. Lift Distribution. Wing-Tail-Rotor Configuration, Airspeed = 80 kt, $\alpha = 4.5^\circ$, Nacelle Incidence = 90° , Angular Speed = 565 rpm, Chordwise Direction, Root Chord.



(a) Lift Coefficient



(b) Pitching Moment Coefficient

Figure 25. Aerodynamic Coefficients as Function of Number of Elements, Wing-Tail Combination, No Rotor, Airspeed = 80 kt, $\alpha = 4.5^\circ$.

ORIGINAL PAGE IS
OF POOR QUALITY

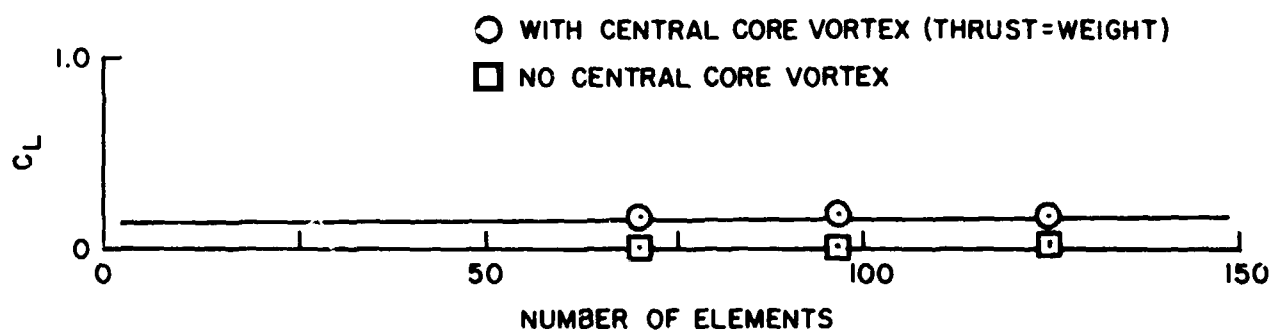
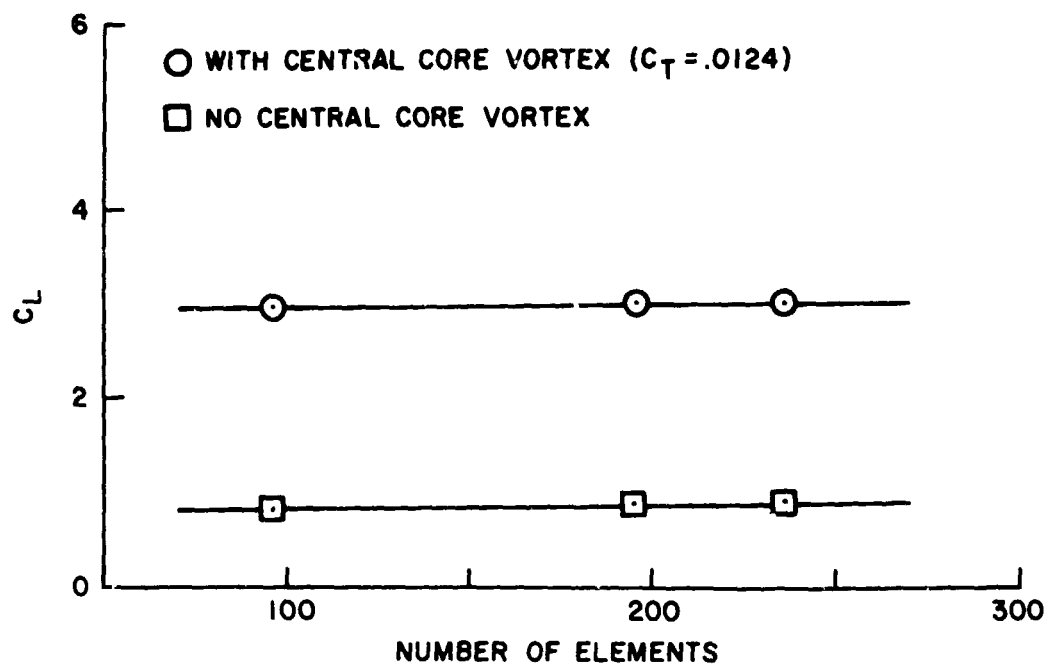
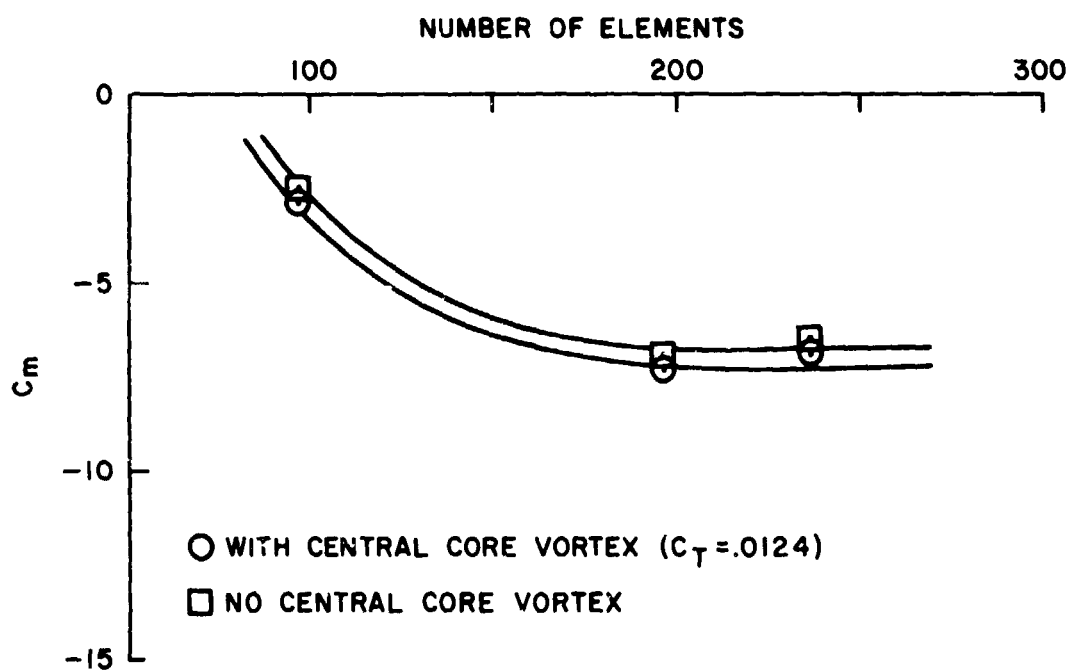


Figure 26. Lift Coefficient on Actuator Disk as Function of Number of Elements, Angular Speed = 600 rpm, Mast Angle = 90°.



(a) Lift Coefficient



(b) Pitching Moment Coefficient

Figure 27. Aerodynamic Coefficients as Function of Number of Elements, Wing-Tail-Rotor Configuration, Airspeed = 80 kt, $\alpha = 4.5^\circ$, Nacelle Incidence = 90° , Angular Speed = 565 rpm.

ORIGINAL PAGE IS
OF POOR QUALITY

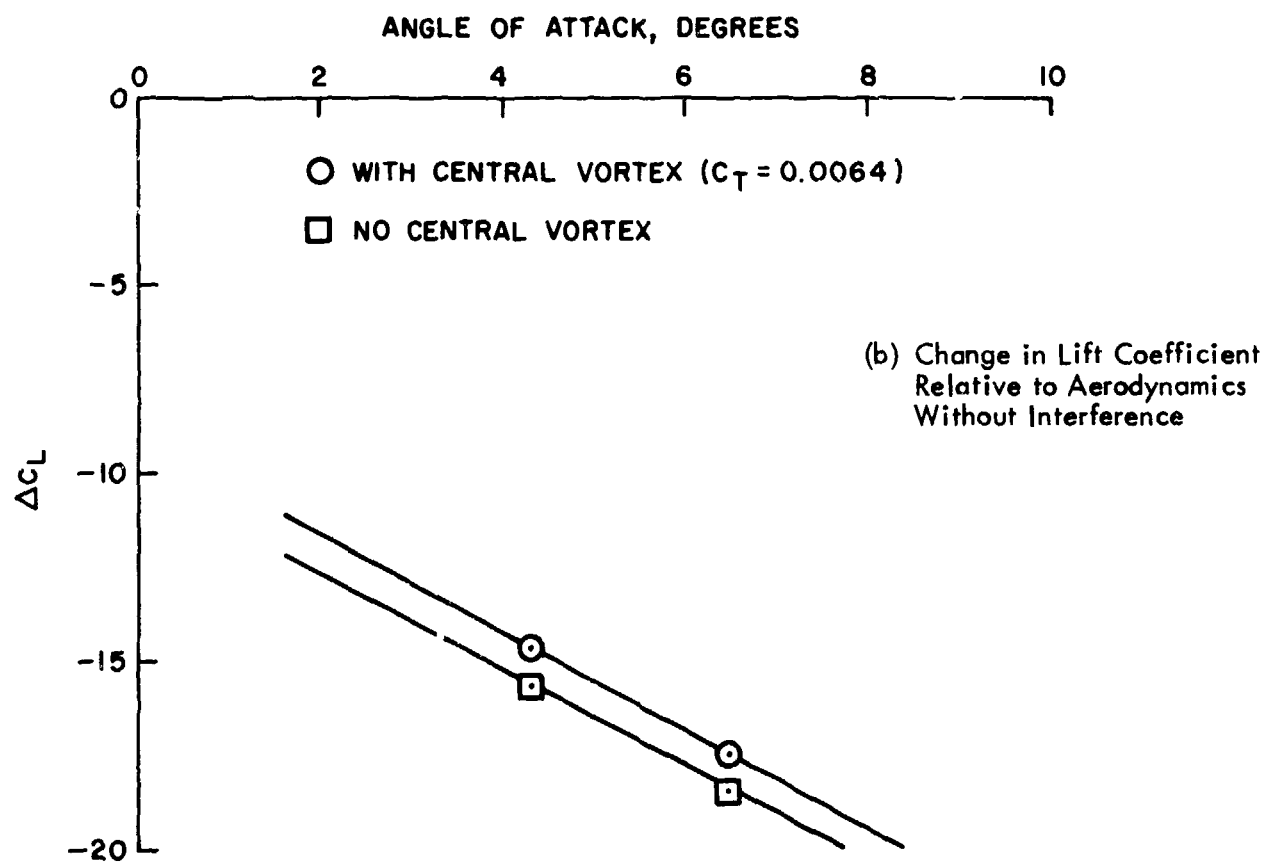
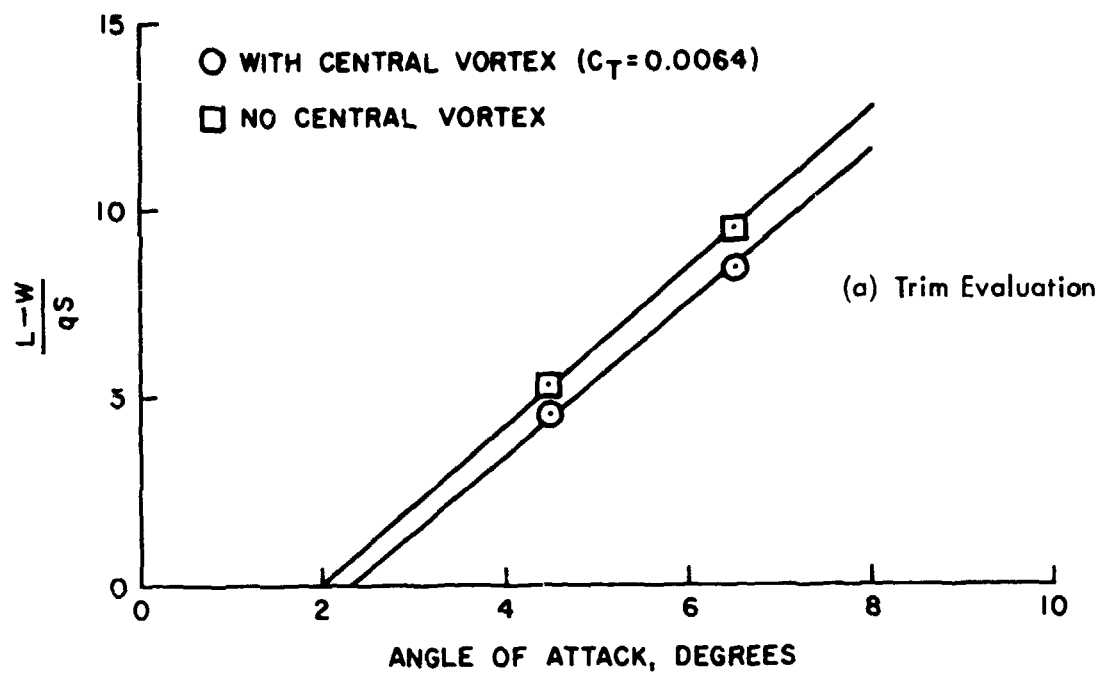
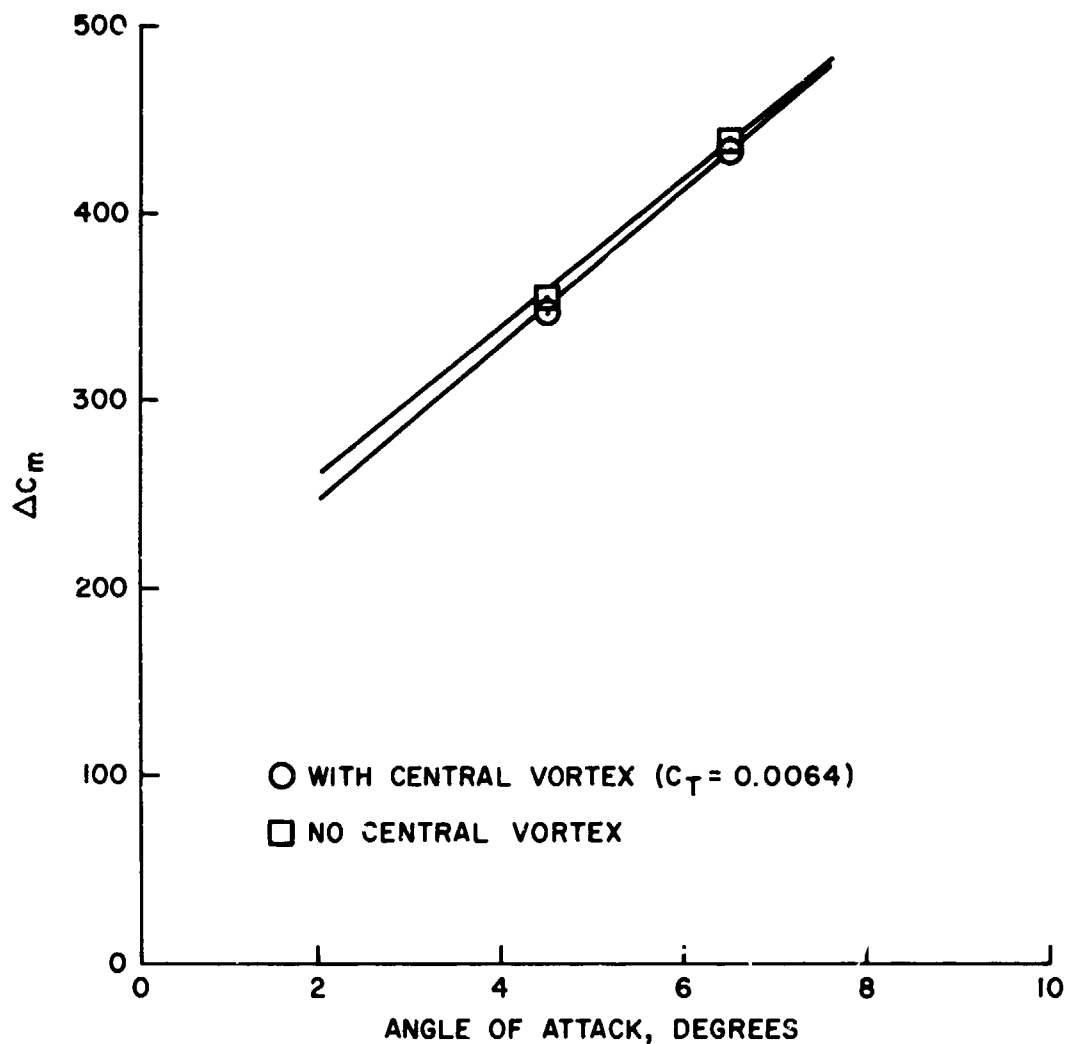


Figure 28. Interference Effects for Conversion Mode, Wing-Tail-Rotor Configuration, Airspeed = 100 kt, Tail Incidence = -1.5° , Nacelle Incidence = 60° , Angular Speed = 565 rpm.



(c) Change in Pitching Moment Coefficient Relative to Aerodynamics Without Interference

Figure 28. Interference Effects for Conversion Mode, Wing-Tail-Rotor Configuration, Airspeed = 100 kt, Tail Incidence = -1.5° , Nacelle Incidence = 60° , Angular Speed = 565 rpm. (Concluded)

ORIGINAL PAGE IS
OF POOR QUALITY

SECTION 10

CONCLUSIONS AND RECOMMENDATIONS

The theoretical methodology and corresponding numerical procedure for the evaluation of rotor-aircraft aerodynamics have been formulated. Results were obtained for a wing-body-rotor configuration of the XV-15 tilting proprotor aircraft at various flight conditions and they are presented in Section 9. Concluding remarks on the present study are summarized in Subsection 10.1. Based on the results obtained, the areas recommended for future research are identified in Subsection 10.2.

10.1 CONCLUSIONS

The purpose of this investigation was to demonstrate the feasibility and flexibility of a computer method to study the rotor-aircraft aerodynamics with special attention given to the rotor wake interference effects on tilting proprotor research aircraft. Due to the preliminary nature of the study, the geometry of the fuselage, engine nacelles, and vertical stabilizers were not included in the analysis. Furthermore, the presence of the viscous drag on the aircraft was not included in the pitching moment calculation.

The numerical technique used in this investigation indicated a good rate of convergence with the possible exception of the pressure on the tail. This was due to the effect of the wing wake on the tail. The subject of coplanar wake interference is treated in great detail in Reference 49. For the flight configurations explored in this study, the effects of the rotor wake interference on the XV-15 tilt rotor aircraft yielded a reduction in the total lift and an increase in the nose-down pitching moment.

In order to extend the existing theoretical formulation to include actuator disk aerodynamics, new concepts were developed. As shown in Appendix B, the tilt rotor aircraft problem yielded a system of algebraic equations with zero determinant.

ORIGINAL PAGE IS
OF POOR QUALITY

REVERSING PAGE BLANK NOT FILMED

It must be emphasized that the problem of zero determinant is encountered whenever the wake separates the flow field into two regimes and is not peculiar to the actuator disk. The problem also occurs with the aerodynamics of blunt fuselage configurations as well as with aerodynamics of buildings. Also, in solving the problem with the actuator disk, the strength of the branch wake, $\Delta \varphi_B$, may assume any value and cannot be determined explicitly in general. In Appendix C it is shown that $\Delta \varphi_B$ can be prescribed as a function of rotor thrust. In addition to exploration of the problem being singular, new boundary conditions for the actuator disk were formulated and discussed in Section 6.

10.2 RECOMMENDATIONS FOR FUTURE RESEARCH

The feasibility and flexibility of a computer method to study rotor wake interference effects on the XV-15 aircraft have been demonstrated. The computer program can easily be extended for analysis of more complex problems such as helicopter and other VTOL configurations. It is emphasized that the only required inputs to the program are the locations of the corner points of the aerodynamic elements and certain specifications to the problem, i.e., Mach number, rotor angular speed, angle of attack, and rotor thrust for the actuator disk. In addition, the geometry of the wake is automatically generated. It is also of particular importance to the user that the program is extremely easy to use because familiarity with the specific method is thus not required. Present outputs available from the computer program include the aerodynamic coefficients, i.e., lift, induced drag, and pitching moment as well as the pressure and velocity flow field around the configuration.

It is emphasized that the use of an actuator disk model for the aircraft rotor allows the study of aerodynamic interference effects on the XV-15 tilting proprotor aircraft, but does not allow the prediction of the lift on the rotor. The Green's formulation for the actuator disk requires the strength of the branch wake on the disk to be

prescribed as an input and this strength is proportional to the lift or thrust on the rotor. Hence, to obtain the lift on the rotor, a formulation with rotor blades can be developed and included in the analysis.

More detailed study on the XV-15 tilt rotor aircraft can easily be undertaken to obtain and assess the following:

- Effects of a rotor-blade model on the aircraft aerodynamic interference.
- Effects of vehicle configuration and speed on the longitudinal trim.
- Sensitivity of the aerodynamic interference effects to variations in aircraft gross weight and power.
- Effects of aerodynamic interference on the aircraft stability and handling qualities and characteristics.

Other areas for future investigation include:

- The case of fully unsteady incompressible flow can be analyzed. This requires a step-by-step analysis in time: at each step a new geometry of the wake is obtained from the tangency condition, while the shed-vorticity intensity is known from preceding time histories. Also, the actual geometry of the tilt rotor aircraft can be implemented. Since the problem is unsteady, the actuator disk model is not required.
- The effect of the compressibility can also be included with special attention given to the analysis of the singular blade problem. This requires an extensive modification of the procedure for incompressible flow.

ORIGINAL PAGE IS
OF POOR QUALITY

REFERENCES

1. DeTore, J. A.; and Sambell, K. W.: Conceptual Design Study of 1985 Commercial Tilt Rotor Transports; Volume I - VTOL Design Summary. NASA CR-2544, May 1975.
2. Maisel, M. (Coordinator): NASA/Army XV-15 Tilt Rotor Research Aircraft Familiarization Document. NASA TM X-62,407, January 1975.
3. Johnson, W.: Dynamics of Tilting Proprotor Aircraft in Cruise Flight. NASA TN D-7677, May 1974.
4. Johnson, W.: Analytical Model for Tilting Proprotor Aircraft Dynamics, Including Blade Torsion and Coupled Bending Modes, and Conversion Mode Operation. NASA TM X-62,369, August 1974.
5. Bell Helicopter Company: V/STOL Tilt Rotor Research Aircraft; Volume 3 - Structural Loads and Dynamics. Report 301-199-003, January 1973.
6. Yasue, M.: A Study of Gust Response for a Rotor-Propeller in Cruising Flight. NASA CR-137537, August 1974.
7. Ludi, I. H.: Composite Aircraft Design. Journal of American Helicopter Society, Vol. 13, No. 1, 1968, pp. 1-13.
8. Wernicke, K. G.: Tilt Proprotor Composite Aircraft, Design State of the Art. Journal of American Helicopter Society, Vol. 14, No. 2, 1969, pp. 10-25.
9. Bell Helicopter Co.: V/STOL Tilt-Rotor Study Task II - Research Aircraft Design. NASA CR-114442, March 1972.
10. Boeing Vertol Co.: V/STOL Tilt-Rotor Aircraft Study, Volume II - Preliminary Design of Research Aircraft. NASA CR-114438, March 1972.
11. Bell Helicopter Company: V/STOL Tilt Rotor Research Aircraft, Volume II - Stability and Control and Handling Qualities Analyses. Report 301-199-002, January 1973.
12. Wilson, J. C.: Powered-Force Wind Tunnel Test of the Bell Helicopter Model C100-F1B Tilt Rotor Aircraft. NASA Langley V/STOL Report 31.
13. Ashley, H.: Some Considerations Relative to the Prediction of Unsteady Air Loads on Lifting Configurations. Journal of Aircraft, Vol. 8, No. 10, October 1971, pp. 741-756.
14. Ashley, H.; Widnall, S.; and Landahl, M. T.: New Directions in Lifting Surface Theory. AIAA Journal, Vol. 3, No. 1, January 1965, pp. 3-16.
15. Ashley, H.; and Rodden, W. P.: Wing-Body Aerodynamic Interaction. Annual Review of Fluid Mechanics, Vol. 4, 1972, pp. 431-472.
16. Hess, J. L.; and Smith, A. M. O.: Calculation of Nonlifting Potential Flow About Arbitrary Three-Dimensional Bodies. ES 40622, Douglas Aircraft Company, 1962.

17. Rubbert, P. E.; and Saaris, G. R.: Review and Evaluation of Three-Dimensional Lifting Potential Flow Analysis Method for Arbitrary Configurations. AIAA Paper No. 72-186, January 1972.
18. Hess, J. L.: Calculation of Potential Flow About Arbitrary Three-Dimensional Lifting Bodies. Report No. MDC J5679-01, Douglas Aircraft Company, 19. 2.
19. Labrujere, T. G.; Loeve, W.; and Sloof, J. W.: An Approximate Method for the Calculation of the Pressure Distribution of Wing-Body Combinations at Subcritical Speeds. AGARD Specialist Meeting on Aerodynamic Interference, Silver Spring, Maryland, September 1970, AGARD Conference Proceedings No. 71.
20. Woodward, F. A.: Analysis and Design of Wing-Body Combinations at Subsonic and Supersonic Speeds. Journal of Aircraft, Vol. 5, No. 6, November-December 1968, pp. 528-534.
21. Albano, E.; and Rodden, W. P.: A Doublet Lattice Method for Calculating Lift Distributions on Oscillating Surfaces in Subsonic Flows. AIAA Journal, Vol. 7, No. 2, February 1969, pp. 279-285.
22. Giesing, J. P.; Kalman, T. P.; and Rodden, W. P.: Subsonic Steady and Oscillatory Aerodynamics for Multiple Interfering Wings and Bodies, Journal of Aircraft, Vol. 9, No. 10, October 1972, pp. 693-702.
23. Carmichael, R. L.; and Woodward, F. A.: An Integrated Approach to the Analysis and Design of Wings and Wing-Body Combinations in Supersonic Flow. NASA TN D-3685, October 1966.
24. Baals, D. D.; Robins, A. W.; and Harris, R. V., Jr.: Aerodynamic Design Integration of Supersonic Aircraft, Journal of Aircraft, Vol. 7, No. 7, September-October 1970, pp. 385-394.
25. Fox, C. H., Jr.; and Breedlove, W. J., Jr.: Application of an Improved Unified Subsonic-Supersonic Potential Flow Method for the Aerodynamic Analysis of Aircraft Configurations. AIAA Paper No. 74-186, January-February 1974.
26. Morino, L.: Unsteady Compressible Potential Flow Around Lifting Bodies Having Arbitrary Shapes and Motions. TR-72-01, Department of Aerospace Engineering, Boston University, June 1972. NASA CR-2464, 1973.
27. Morino, L.: Unsteady Compressible Potential Flow Around Lifting Bodies - General Theory. AIAA Paper No. 73-196, January 1973.
28. Morino, L.; and Kuo, C. C.: Unsteady Subsonic Compressible Flow Around Finite-Thickness Wings. AIAA Paper No. 73-313, March 1973.
29. Morino, L.; and Kuo, C. C.: Subsonic Potential Aerodynamics for Complex Configurations: A General Theory. AIAA Journal, Vol. 12, No. 2, February 1974, pp. 191-197.

30. Chen, L. T.; Suciu, E. O.; and Morino, L.: A Finite Element Method for Potential Aerodynamics Around Complex Configurations. AIAA Paper No. 74-107, January-February 1974.
31. Gaffey, T. M.; and Maisel, M. D.: Measurement of Tilt-Rotor VTOL Rotor Wake-Airframe-Ground Aerodynamic Interference for Application to Real Time Flight Simulation. AGARD CP-143, October 1974.
32. Marr, R. L.; and Roderick, W. E. B.: Handling Qualities Evaluation of the XV-15 Tilt-Rotor Aircraft. Journal of the American Helicopter Society, 20, 2, April 1975.
33. Marr, R. L.; Ford, D. G.; and Ferguson, S. W.: Analysis of the Wind Tunnel Test of a Tilt Rotor Powered Force Model. NASA CR-137529, June 1, 1974.
34. Pruyn, R. R.; and Taylor, R. B.: Design Considerations for Tilt-Rotor VTOL Aircraft to Minimize the Effects of the Recirculating Downwash Environment. Journal of the American Helicopter Society, 16, 4, October 1971.
35. Goldstein, S.: On the Vortex Theory of Screw Propellers. Proc. Royal Society, A, 123, 792, April 1929.
36. Erickson, J. D.; and Ordway, D. C.: A Theory for Static Propeller Performance. CAL/USAAVLABS Symposium Proceedings, Vol. 1, June 1966.
37. Trenka, A. C.: Prediction of the Performance of VTOL Propellers. CAL/USAAVLABS Symposium Proceedings, Vol. 1, June 1966.
38. Davenport, F. J., et al: Analysis of Propeller and Rotor Performance by an Explicit Vortex Influence Technique. Boeing-Vertol Report No. R-372, February 1965.
39. Heyson, H. H.; and Katzoff, S.: Induced Velocities Near a Lifting Rotor with Nonuniform Disk Loading. NACA TR-1319, 1957.
40. Marr, R. L.; and Roderick, W. E. B.: Handling Qualities Evaluation of the XV-15 Tilt Rotor Aircraft. Journal of the American Helicopter Society, 20, 2, April 1975.
41. Gessow, A.; and Myers, G. C.: Aerodynamics of the Helicopter. MacMillan Co., 1952.
42. Drees, J. M.: A Theory of Airflow Through Rotors and Its Application to Some Helicopter Problems. Journal of the Helicopter Association of Great Britain, 3, 2, July-August-September, 1949.
43. Morino, L; and Chen, L. T.: Subsonic and Supersonic Indicial Aerodynamics and Aerodynamic Transfer Function for Complex Configurations. Boston University, ENG-TN-74-01, September 1974.

44. Morino, L.; Chen, L. T.; and Suci, E. O.: Steady and Oscillatory Subsonic and Supersonic Aerodynamics Around Complex Configurations. AIAA Journal, Vol. 13, No. 3, March 1975, pp. 368-374.
45. Morino, L.: A General Theory of Unsteady Compressible Potential Aerodynamics. NASA CR-2464, December 1974.
46. Morino, L.; and Chen, L. T.: Indicial Compressible Potential Aerodynamics Around Complex Aircraft Configurations. Published in Aerodynamic Analysis Requiring Advanced Computers, Vol. II, NASA SP-347 1975, pp. 1067-1110.
47. Noll, R. B.; and Morino, L.: Flight Control Analysis Program (FCAP) for Arbitrary-Configuration Flexible Aircraft with Active Control; Vol. I: Theoretical Analysis. Aerospace Systems, Inc., ASI-TR-75-23, October 1975.
48. Johnson, W.: Analytical Modeling Requirements for Tilting Propeller Aircraft Dynamics. NASA TN D-8013, July 1975.
49. Tseng, K.; and Morino, L.: A New Unified Approach for Analyzing Wing-Body-Tail Configurations with Control Surfaces. AIAA 9th Fluid and Plasma Dynamics, AIAA Paper No. 76-418, July 1976.

APPENDIX A

AERODYNAMIC POTENTIAL PROGRAM SUSSA ACTS

Computer program SUSSA ACTS (Steady and Unsteady Subsonic and Supersonic Aerodynamics for Aerospace Complex Transportation Systems) implements the method of Morino (References 27 to 29 and 43 to 46). This program is very flexible, simple to use, and modular. The geometry is defined in one section, while a second part evaluates the normal wash, the potential, the pressure coefficient, and the aerodynamic coefficients (lift, moment, and generalized-force coefficients). Moreover, the user need not be familiar with the aerodynamic portion of the program, unlike other sophisticated aerodynamic programs in which the choice for the combination of various panels (sources, doublets, vortices) is an art which requires considerable understanding of the method. Another advantage of SUSSA ACTS is that the paneling used for the aerodynamics is completely arbitrary and, therefore, may coincide with the one used for the structural analysis. These attributes of the program make the method extremely efficient from a practical point of view. Finally, the method is both accurate and fast, despite the fact that no effort has yet been made to minimize the computation time (see References 29, 44, and 46). Other important features of SUSSA ACTS are:

- Inclusion of control surface mode shapes (i.e., surface rotation).
 - Option to compute aerodynamic forces caused by turbulence.
 - Computation of downwash from arbitrary modes.
 - Geometry preprocessor for conventional wing-body-tail combination.
- Option to compute low-frequency (quasi-steady aerodynamic coefficients).

A flow diagram of SUSSA ACTS is presented in Figure A-1. The sub-routines which perform the indicated functions are denoted in the appropriate blocks.

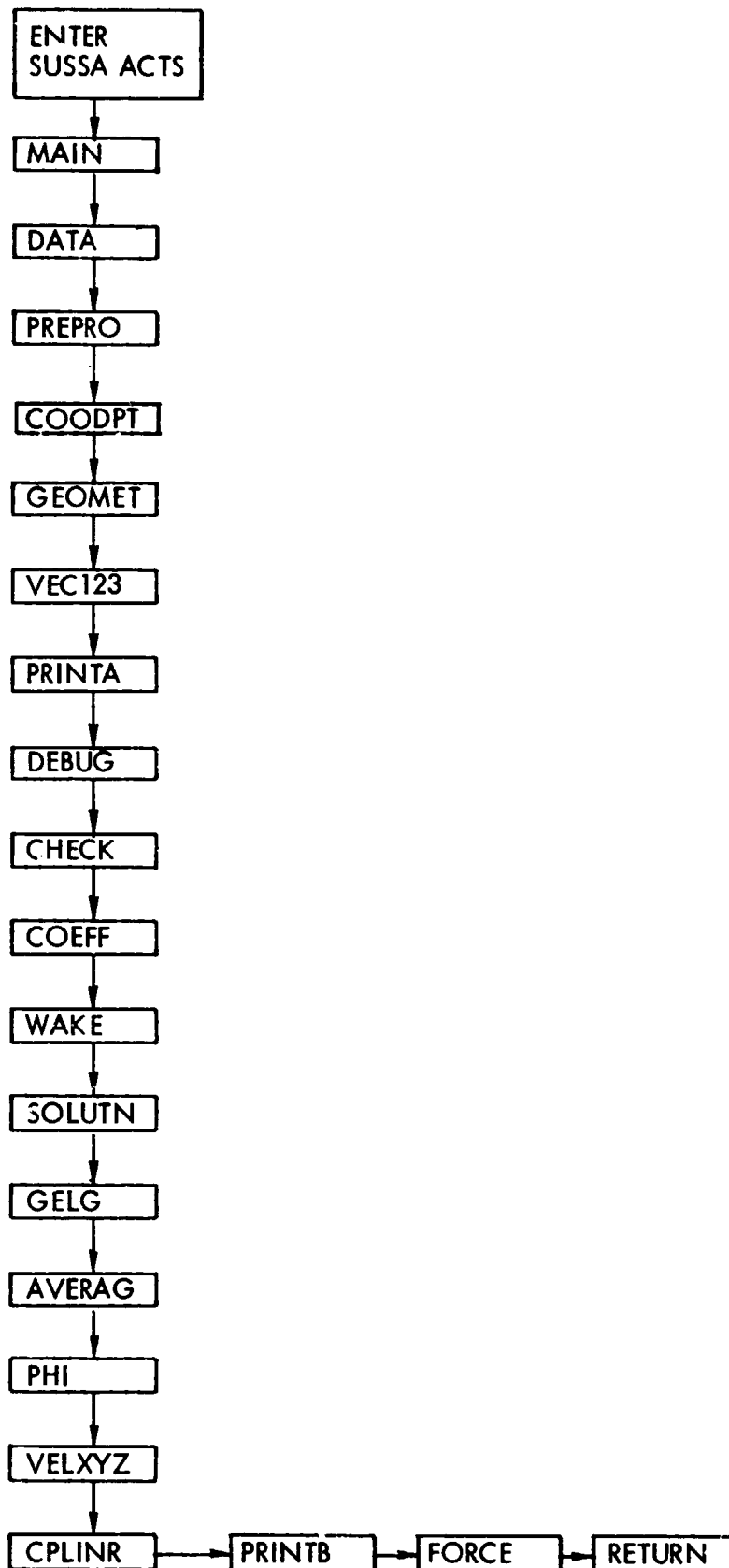


Figure A-1. Program SUSSA ACTS.

Basically, SUSSA ACTS performs two separate functions: one is the definition of the aerodynamic paneling on the aircraft, and the second is the computation of the aerodynamic potential and pressure distributions and the determination of the aerodynamic force coefficients. The aerodynamic paneling can be accomplished manually by inputting the coordinates of the corner points of all selected aerodynamic panels, or by using a geometry preprocessor. A geometry preprocessor for conventional wing-body-tail configurations is incorporated in SUSSA ACTS (Reference 47). Given the aircraft configuration geometry, the preprocessor computes the corner point locations of required aerodynamic panels for the wing-body-tail configuration. Required inputs include:

- Fuselage length.
- Fuselage diameter (assumed circular) - center section.
- Fuselage shape factors for nose and tail sections.
- Wing span.
- Wing sweep angle.
- Horizontal and vertical tail spans.
- Horizontal and vertical tail sweep angles.

This routine eliminates the requirement for the selection of aerodynamic paneling by the user.

The second section of SUSSA ACTS implements the aerodynamic potential computation method of Reference 44. These computations require the aerodynamic panel corner point locations and input rigid-body and flexible-body mode shapes, control surface rotations, and turbulence. The aerodynamic potential is computed first, the pressure coefficient distributions are then determined, and the aerodynamic force coefficients are computed.

ORIGINAL PAGE IS
OF POOR QUALITY

APPENDIX B

INTEGRAL EQUATION FOR ACTUATOR DISK

A general integral equation for actuator disks is presented in Section 6. In this appendix a few mathematical details which are important for the solution of the integral equation are discussed thoroughly. For simplicity the emphasis is placed on an axisymmetric problem, although all the main conclusions are valid for a general configuration as well.

B.1 INTEGRAL REPRESENTATION FOR ACTUATOR DISK

The integral representation of the potential for actuator disks is presented in Section 6. Noting that since the potential difference $\Delta \varphi = \Delta \varphi_B$ is constant on the branch wake, Equation (69) may be rewritten as

$$4\pi E_* \varphi_* = - \oint_{\Sigma_D} \left[\frac{\partial \varphi}{\partial n} \left(\frac{1}{r} \right) - \varphi \frac{\partial}{\partial n} \left(\frac{1}{r} \right) \right] d\Sigma + \iint_{\Sigma_D'} \Delta \varphi \frac{\partial}{\partial n} \left(\frac{1}{r} \right) d\Sigma + \Delta \varphi_B \iint_{\Sigma_B'} \frac{\partial}{\partial n_B} \left(\frac{1}{r} \right) d\Sigma \quad (B-1)$$

If P_* is on Σ_D , the function $E(P)$ assumes the value $E_* = 1/2$ and Equation (B-1) reduces to an integral equation. As mentioned in Section 6, in solving this integral equation, $\Delta \varphi_B$ may assume any value. Therefore, in the actuator disk formulation, $\Delta \varphi_B$ (which is approximately proportional to the thrust) is not an output but an input to the problem. This indicates that the actuator disk integral equation is singular, since the solution is not unique. This point is analyzed further in Subsection B.3.

In addition, even if $\Delta \varphi_B$ is treated as a constant, the integral equation is still singular. The problem exists any time when the wake separates the flow field into

two separate regions, one inside and one outside the wake. It should be noted that this is the only reason for this problem, and therefore is not peculiar to the actuator disk. This problem occurs in the formulation for bodies with a blunt back such as a fuselage with truncated base. A similar problem occurs in the formulation for building aerodynamics. This point is analyzed in detail in Section B.2. In order to emphasize that the problem is not peculiar to the actuator disk formulation, $\Delta \varphi_B$ is assumed to be equal to zero (i.e., there is no vortex emanating from the root of the blades), and this is presented in Section B.2. The extension to the case with $\Delta \varphi_B$ different from zero is considered in Section B.3.

B.2 ACTUATOR DISK WITH $\Delta \varphi_B = 0$

In order to show that the integral equation for the actuator disk is singular even if $\Delta \varphi_B$ is prescribed, it is convenient to obtain Equation (B-1) a new way. Assume $\Delta \varphi_B = 0$. Consider Figure B-1(c), and note that the value $E = 1$ outside the actuator disk may be obtained as the sum of the function E_i for inner flow (i.e., inside the wake) and the function E_o for the outer flow (i.e., outside the wake) or

$$E(P) = E_i(P) + E_o(P) \quad (B-2)$$

Applying Green's theorem to the regions shown in Figures B-1(a) and B-1(b) yields

$$4\pi E_i(P_*) \varphi(P_*) = - \oint \left[\frac{\partial \varphi}{\partial n_i} \left(\frac{1}{r} \right) - \varphi \frac{\partial}{\partial n_i} \left(\frac{1}{r} \right) \right] d\Sigma_i \quad (B-3)$$

and

$$4\pi E_o(P_*) \varphi(P_*) = - \oint \left[\frac{\partial \varphi}{\partial n_o} \left(\frac{1}{r} \right) - \varphi \frac{\partial}{\partial n_o} \left(\frac{1}{r} \right) \right] d\Sigma_o \quad (B-4)$$

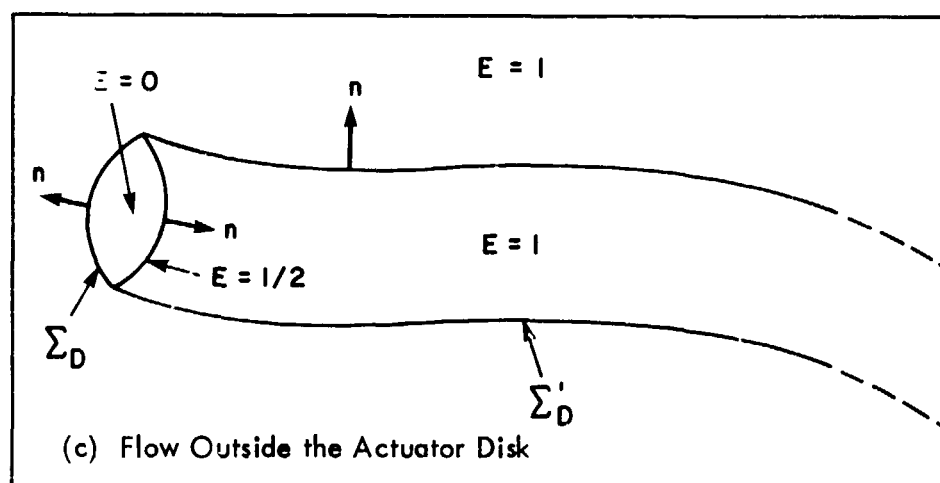
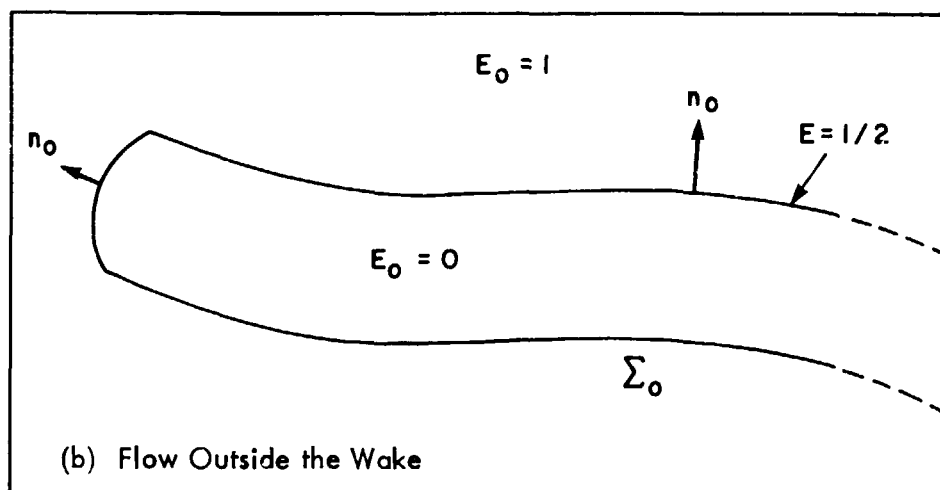
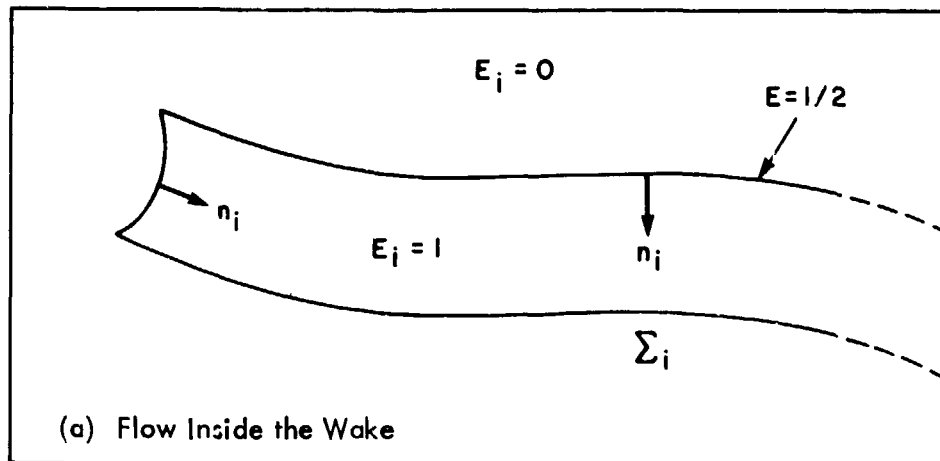


Figure B-1. Geometry for Green's Theorem for Actuator Disk.

Note that

$$\begin{aligned} n_i &= n; n_o = n & \text{on } \Sigma_D \\ n_i &= -n; n_o = n & \text{on } \Sigma'_D \end{aligned} \quad (B-5)$$

Thus, adding Equations (B-3) and (B-4) and using Equations (B-2) and (B-5) yields

$$\begin{aligned} 4\pi E(P_*) \varphi(P_*) &= - \oint\oint_{\Sigma_D} \left[\frac{\partial \varphi}{\partial n} \left(\frac{1}{r} \right) - \varphi \frac{\partial}{\partial n} \left(\frac{1}{r} \right) \right] d\Sigma \\ &+ \oint\oint_{\Sigma'_D} \Delta \varphi \frac{\partial}{\partial n} \left(\frac{1}{r} \right) d\Sigma \end{aligned} \quad (B-6)$$

where $\Delta \varphi \equiv \varphi_o - \varphi_i$. Note that Equation (B-6) coincides with Equation (B-1) with $\Delta \varphi_B = 0$. In order to show that the operator in Equation (B-6) is singular, it is sufficient to show that the homogeneous equation (i.e., with $\partial \varphi / \partial n = 0$)

$$4\pi E(P_*) \varphi(P_*) = \oint\oint_{\Sigma_D} \varphi \frac{\partial}{\partial n} \left(\frac{1}{r} \right) d\Sigma + \oint\oint_{\Sigma'_D} \Delta \varphi \frac{\partial}{\partial n} \left(\frac{1}{r} \right) d\Sigma \quad (B-7)$$

has a nontrivial solution. In order to show this, consider the function

$$\begin{aligned} \varphi(P) &= 0 & P \text{ outside } \Sigma_i \\ &= 1 & P \text{ inside } \Sigma_i \end{aligned} \quad (B-8)$$

If $\partial \varphi / \partial n = 0$ (homogeneous problem), this function is a trivial solution (i.e., $0 = 0$) of Equation (B-4), whereas for Equation (B-3) one obtains (note that $E_i \varphi_{NT} = E_i$)

$$4\pi E_i = \oint\oint_{\Sigma_i} \frac{\partial}{\partial n_i} \left(\frac{1}{r} \right) d\Sigma_i \quad (B-9)$$

which is identically satisfied, since (indicating with Ω the solid angle)

$$\oint_{\Sigma_i} \frac{\partial}{\partial n_i} \left(\frac{1}{r} \right) d\Sigma_i \equiv \Omega = \begin{aligned} &0 \text{ outside } \Sigma_i \\ &= 2\pi \text{ on } \Sigma_i \\ &= 4\pi \text{ inside } \Sigma_i \end{aligned} \quad (\text{B-10})$$

Since φ_{NT} is a nontrivial solution for both Equations (B-3) and (B-4) with $\partial\varphi/\partial n = 0$, it is a nontrivial solution for their sum, Equation (B-7). Hence, the operator in Equation (B-1) (with $\Delta\varphi_B = 0$) is singular; therefore, if φ satisfies Equation (B-1), then

$$\varphi = \hat{\varphi} + C\varphi_{NT} \quad (\text{B-11})$$

(where C is an arbitrary constant) also satisfies Equation (B-1).

Finally note that in the numerical formulation, Equation (B-1) is replaced by Equation (91). However, the doublet integral represents solid angles and the total solid angle is evaluated exactly with the use of the hyperboloidal elements. Thus the discrete form of Equation (B-10) is still valid exactly. Therefore, even the discrete system is singular, i.e., the determinant of the system given by Equation (91) is equal to zero. This implies that the vector

$$\{\varphi_i^{NT}\} = \{\varphi_{NT}(P_i)\} \quad (\text{B-12})$$

is a nontrivial solution for Equation (91) with right-hand-side equal to zero, or that if $\hat{\varphi}_i$ is a solution to Equation (91), then

$$\{\varphi_i\} = \{\hat{\varphi}_i\} + C\{\varphi_i^{NT}\} \quad (\text{B-13})$$

(where C is an arbitrary constant) is also a solution to Equation (91) (i.e., if the solution exists and is not unique).

B.3 ACTUATOR DISK WITH $\Delta \varphi_B \neq 0$

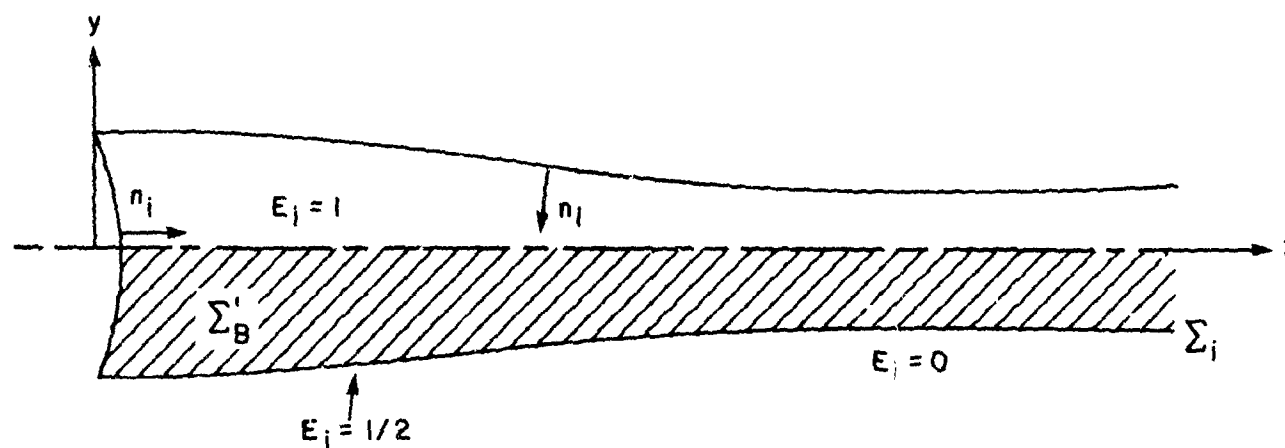
The operator in Equation (B-1) has an additional nontrivial solution; however, this solution does not satisfy Equation (B-6) which is obtained from Equation (B-1) by dropping the branch wake. The implications of this feature are discussed later in the section. An explicit solution for Equation (B-1) is given for an actuator disk in axial flow, i.e., for an axisymmetric case. Then it is shown that the general case has a solution with features similar to the ones of the axisymmetric case.

The geometry for the axisymmetric case is given in Figure B-2, where again it is shown that the complete flow (Figure B-2(c)) may be thought of as the superposition of the flow outside the wake (Figure B-2(b)) plus the one inside the wake (Figure B-2(a)). The shaded area indicates the branch wake (which does not exist for the outer flow, Figure B-2(b)). Applying Green's theorem to the geometries of Figures B-2(a), B-2(b), and B-2(c) yields, respectively

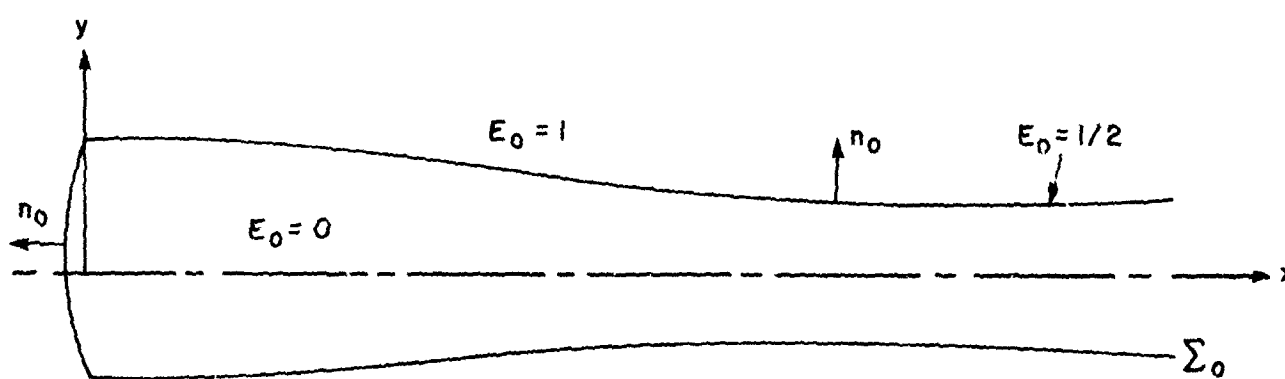
$$4\pi E_i(P_*)\varphi(P_*) = - \oint_{\Sigma_i} \left[\frac{\partial \varphi}{\partial n_i} \left(\frac{1}{r} \right) - \varphi \frac{\partial}{\partial n_i} \left(\frac{1}{r} \right) \right] d\Sigma_i + \Delta \varphi_B \iint_{\Sigma_B} \frac{\partial}{\partial n_B} \left(\frac{1}{r} \right) d\Sigma \quad (B-14)$$

where $\Delta \varphi_B$ is the (constant) potential discontinuity on the branch-wake surface, Σ_B'

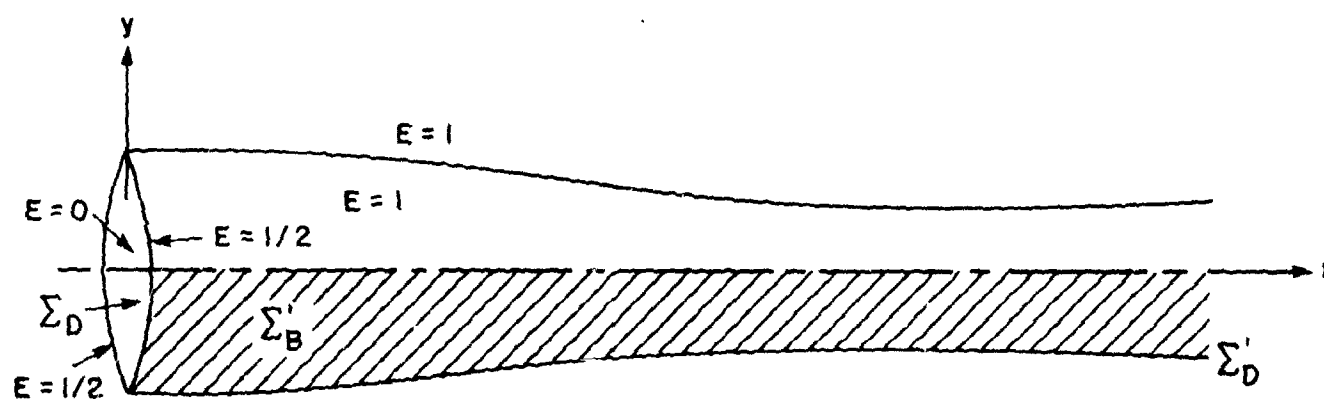
$$4\pi E_o(P_*)\varphi(P_*) = - \oint_{\Sigma_o} \left[\frac{\partial \varphi}{\partial n_o} \left(\frac{1}{r} \right) - \varphi \frac{\partial}{\partial n_o} \left(\frac{1}{r} \right) \right] d\Sigma_o \quad (B-15)$$



(a) Flow Inside the Wake



(b) Flow Outside the Wake



(c) Flow Outside the Actuator Disk

Figure B-2. The Geometry for Axisymmetric Actuator Disk Problem.

ORIGINAL PAGE IS
OF POOR QUALITY

and

$$\begin{aligned}
 4\pi E(P_*)\varphi(P_*) = & - \oint_{\Sigma_D} \left[\frac{\partial \varphi}{\partial n} \left(\frac{1}{r} \right) - \varphi \frac{\partial}{\partial n} \left(\frac{1}{r} \right) \right] d\Sigma \\
 & + \iint_{\Sigma'_D} \Delta \varphi \frac{\partial}{\partial n} \left(\frac{1}{r} \right) d\Sigma \\
 & + \Delta \varphi_B \iint_{\Sigma'_B} \frac{1}{\partial n_B} \left(\frac{1}{r} \right) d\Sigma
 \end{aligned} \tag{B-16}$$

Note that Equation (B-16) may be obtained by adding Equations (B-14) and (B-15).

Consider the nontrivial solution

$$\begin{aligned}
 \varphi_B(P) &= \theta \text{ for } P \text{ inside } \Sigma_i \quad (-\pi \leq \theta \leq \pi) \\
 &= 0 \text{ for } P \text{ outside } \Sigma_i
 \end{aligned} \tag{B-17}$$

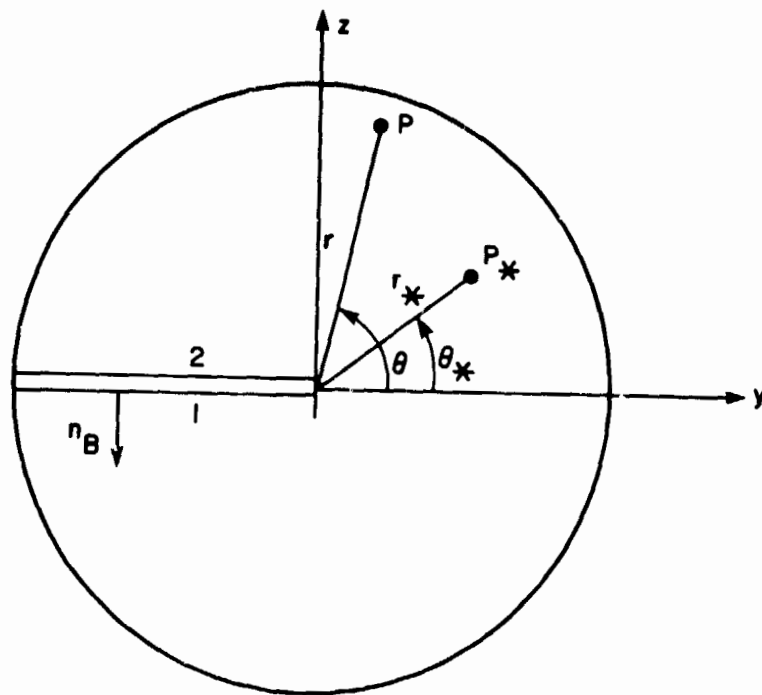
where θ is defined in Figure B-3(a). Note that, by definition of θ , the branch wake is located at $\theta = \pm\pi$. This is not a limitation since, according to Equation (B-14), it is always possible to add a constant to φ_B . Note that in any event

$$\Delta \varphi_B = \varphi_B(P_1) - \varphi_B(P_2) = -2\pi \tag{B-18}$$

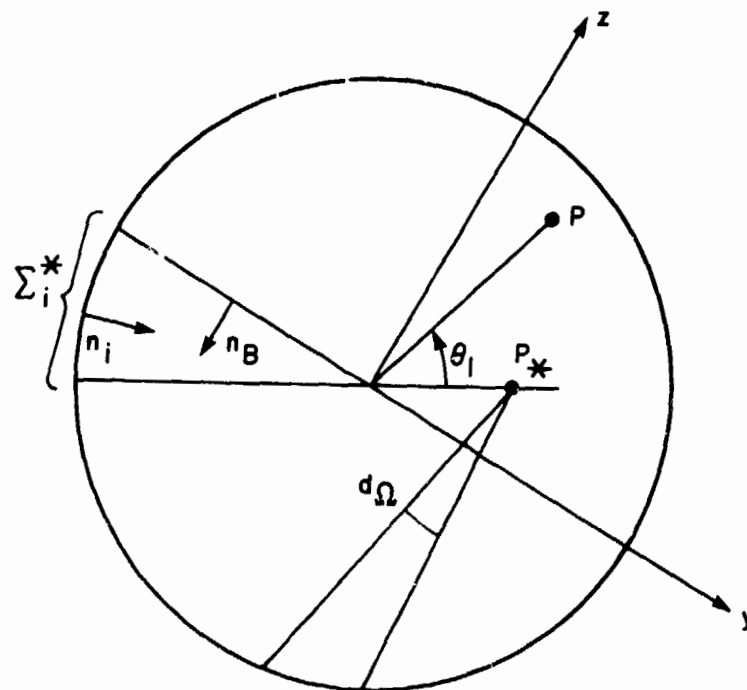
If $\partial\varphi/\partial n = 0$ (homogeneous equation), φ_B satisfies trivially (i.e., $0 = 0$)

Equation (B-15) whereas for Equation (B-14) one obtains

$$\begin{aligned}
 4\pi E(P_*)\varphi(P_*) = & \oint_{\Sigma_i} \theta \frac{\partial}{\partial n_i} \left(\frac{1}{r} \right) d\Sigma_i \\
 & - 2\pi \iint_{\Sigma'_B} \frac{\partial}{\partial n_B} \left(\frac{1}{r} \right) d\Sigma
 \end{aligned} \tag{B-19}$$



(a) Definition of θ



(b) Definition of θ_1

ORIGINAL PAGE IS
OF POOR QUALITY

Figure B-3. Actuator Disk Branch Wake Potential Geometry for Nontrivial Solution.

Note that (see Figure B-4)

$$\begin{aligned} \frac{\partial}{\partial n_i} \left(\frac{1}{r} \right) d\Sigma_i &= -\frac{1}{r^3} (r \cdot n_i) d\Sigma = \frac{d\Sigma \cos \alpha}{r^2} \\ &= \frac{d\Sigma_n}{r^2} = d\Omega \end{aligned} \quad (B-20)$$

is the solid angle for $d\Sigma$ as seen from P_* (positive since $(n \cdot r) < 0$). In order to evaluate the first integral it is convenient to introduce the variable

$$\theta_1 = \theta - \theta_*$$

The function φ_B as a function of θ_1 is given in Figure B-5. Limiting θ_1 to the interval $(-\pi, \pi)$ the function φ_B is given by

$$\varphi_B(P) = \theta_1 + \theta_* - 2\pi H(\theta) \quad (B-21)$$

where (assuming $\theta_* > 0$ for simplicity[†])

$$\begin{aligned} H(\theta_1) &= 0 & -\pi \leq \theta_1 \leq \pi - \theta_* \\ &= 1 & \pi - \theta_* \leq \theta_1 \leq \pi \end{aligned} \quad (B-22)$$

Thus, Equation (B-20) may be rewritten as

$$\begin{aligned} 4\pi E_*(P_*) \varphi(P_*) &= \iint_{\Sigma_i} [\theta_1 + \theta_* - 2\pi H(\theta)] d\Omega \\ &\quad - 2\pi \iint_{\Sigma_B'} d\Omega_B \end{aligned} \quad (B-23)$$

where $d\Omega_B$ is negative since $\bar{n}_B \cdot \bar{r} > 0$.

[†]This hypothesis is not restrictive in view of the axisymmetry of the problem.

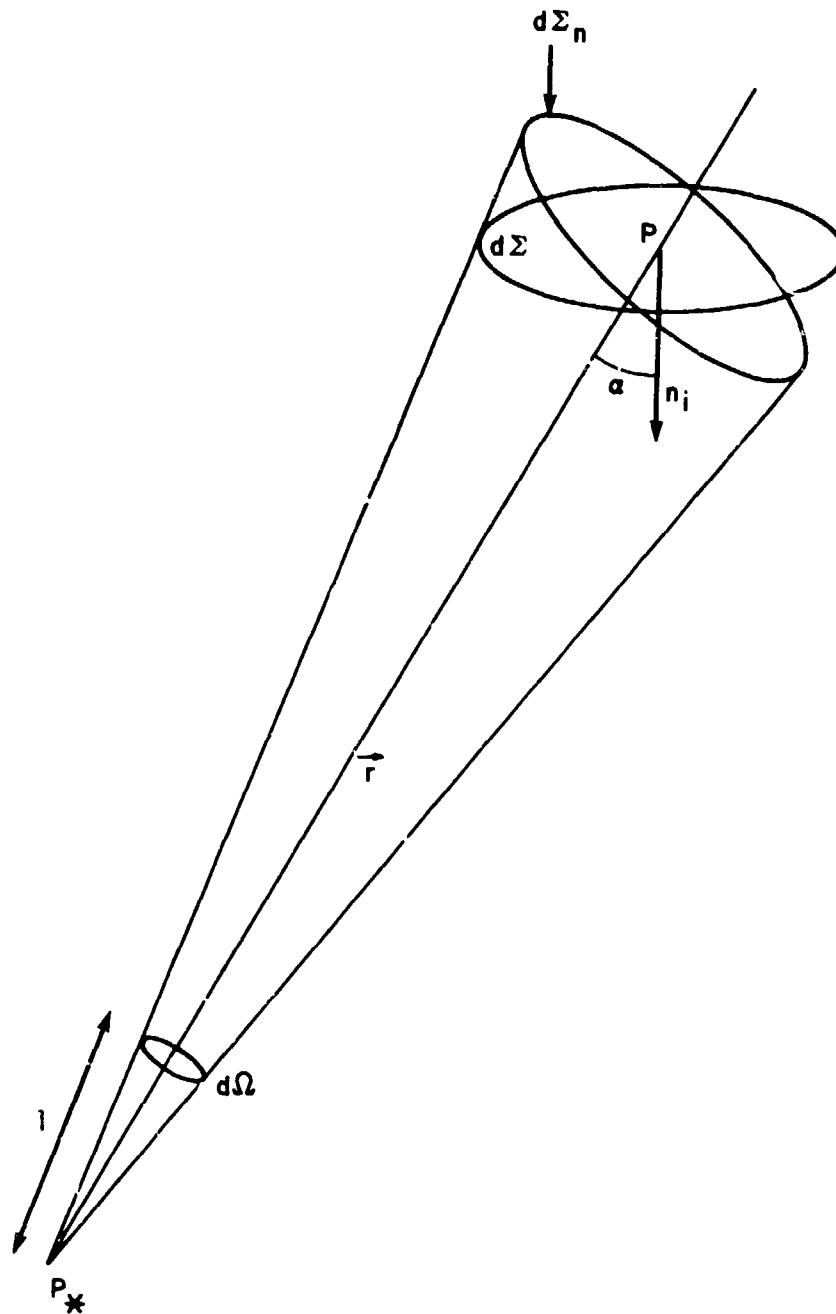


Figure B-4. Solid Angle.

ORIGINAL PAGE IS
OF POOR QUALITY

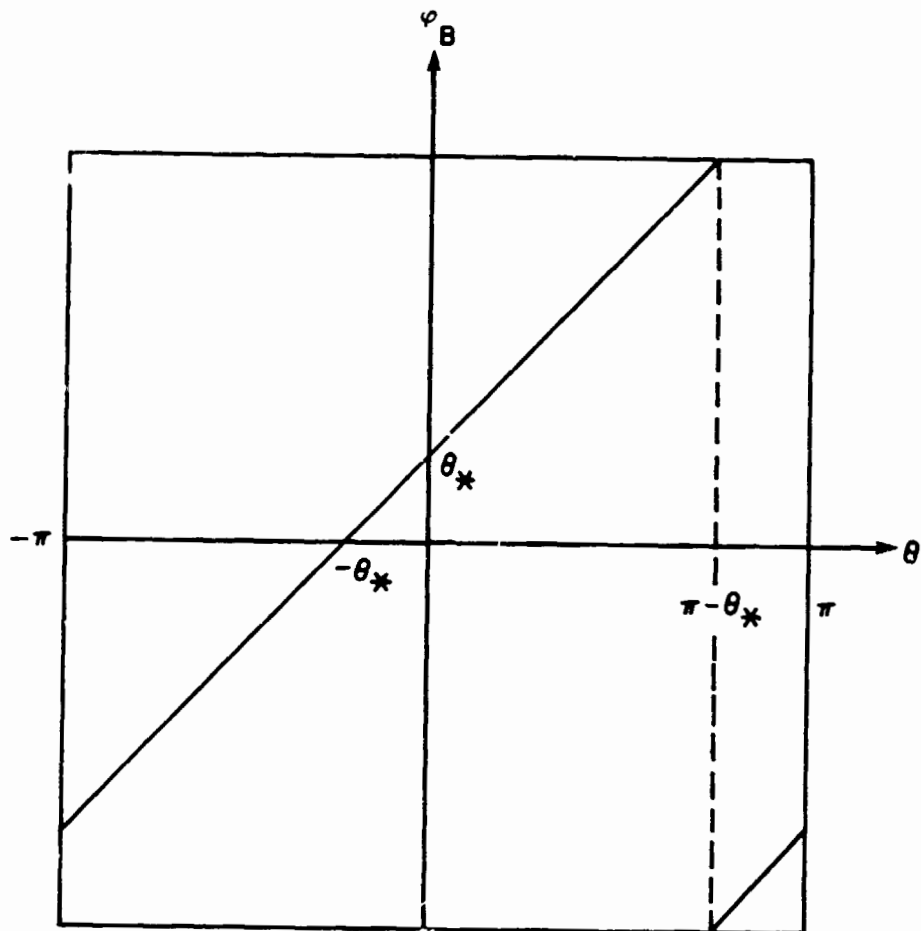


Figure B-5. Variation of φ_B as Function of θ_1 .

Next, note that

$$\iint_{\Sigma_i} \theta_1 d\Omega = 0 \quad (B-24)$$

because of antisymmetry of the integrand, (see Figure B-3(b)). Then, since $d\Omega_B$ is negative,

$$\iint_{\Sigma_i} H(\theta) d\Omega = \iint_{\Sigma_i^*} d\Omega \equiv - \iint_{\Sigma_B'} d\Omega \quad (B-25)$$

Thus, Equation (B-25) reduces to

$$4\pi E_*(P) \varphi_B(P_*) = \theta_* \iint_{\Sigma_i} d\Omega = \theta_* 4\pi E(P_*) \quad (B-26)$$

Since

$$\begin{aligned} \iint_{\Sigma_i} d\Omega &= 4\pi && \text{if } P_* \text{ is inside } \Sigma_i \\ &= 2\pi && \text{if } P_* \text{ is on } \Sigma_i \\ &= 0 && \text{if } P_* \text{ is outside } \Sigma_i \end{aligned} \quad (B-27)$$

Equation (B-27) is equivalent to Equation (B-17). Therefore, φ_B is a nontrivial solution of Equation (B-16) with $\partial\varphi/\partial n = 0$, which indicates that the operator in Equation (B-16) is singular.

Finally, the above results imply that the solution of Equation (B-6) (without branch wake) also satisfies Equation (B-1), since that solution has $\Delta\varphi_B = 0$. Therefore, not only is the determinant equal to zero, but $\Delta\varphi_B$ cannot be determined by Equation (B-1). In order to have a solution with $\Delta\varphi_B \neq 0$, the value of $\Delta\varphi_B$ must be prescribed and the branch wake integral must be treated as a known quantity. This implies that the boundary conditions on $\partial\varphi/\partial n_D$ (Equation (6-11)) are not sufficient to determine the problem, but the value of $\Delta\varphi_B$ (proportional to the lift) must be prescribed as well.

ORIGINAL PAGE IS
OF POOR QUALITY

The above solution could be obtained by noting that the circulation is equal to zero for a contour outside Σ_0 (since the contour may be reduced to zero without intersecting any singular line or surface) whereas the circulation is constant and different from zero if the contour is inside Σ_1 and simply connected with the vortex line emanating from the center of the actuator disk. In other words, for a nonaxisymmetric configuration the nontrivial solution is still equal to zero outside Σ_0 , whereas there is a constant discontinuity on the branch wake.

APPENDIX C

EVALUATION OF THRUST ON THE ROTOR

The rotor thrust perpendicular to the tip path plane can be determined from momentum considerations. For simplicity, only a single rotor blade is explicitly included in the analysis, although the result is valid for multi-blade rotor configurations as well.

Conservation of momentum states that the time rate of increase of momentum within a fixed control volume, V , is equal to the rate at which momentum is changing within V plus the net forces acting on the fluid within V . For the case of steady flow with negligible viscous and body forces, the conservation of momentum is written as

$$\oint_{\Sigma_R + \Sigma_B} p \bar{n} d\Sigma + \oint_{\Sigma_R + \Sigma_B} \rho \bar{V} (\bar{V} \cdot \bar{n}) d\Sigma = 0 \quad (C-1)$$

where the first term represents the forces acting on the control surface due to the normal pressure, p , and the second term represents the change of momentum of the fluid in the control volume. Note that \bar{n} is the unit normal directed positively out from the surface $\Sigma_R + \Sigma_B$. The control surface Σ_D defines an actuator disk which encloses the rotor blade. As shown in Figure C-1, Σ_R is the contour of the rotor blade and, therefore, there is no momentum flux through it.

The fluid enters the control volume at station 1 and leaves at station 2. Note that p_1 , V_1 , and ρ_1 are average values of the pressure, velocity, and density, respectively, upstream of the rotor. Similarly, p_2 , V_2 , and ρ_2 are average values downstream of the rotor. The lateral side of Σ_D can be chosen along streamlines and momentum flows through Σ_D only at stations 1 and 2; hence, any flux through the lateral side of Σ_D is assumed to be negligible. Equation (C-1) can now be written

ORIGINAL PAGE IS
OF POOR QUALITY

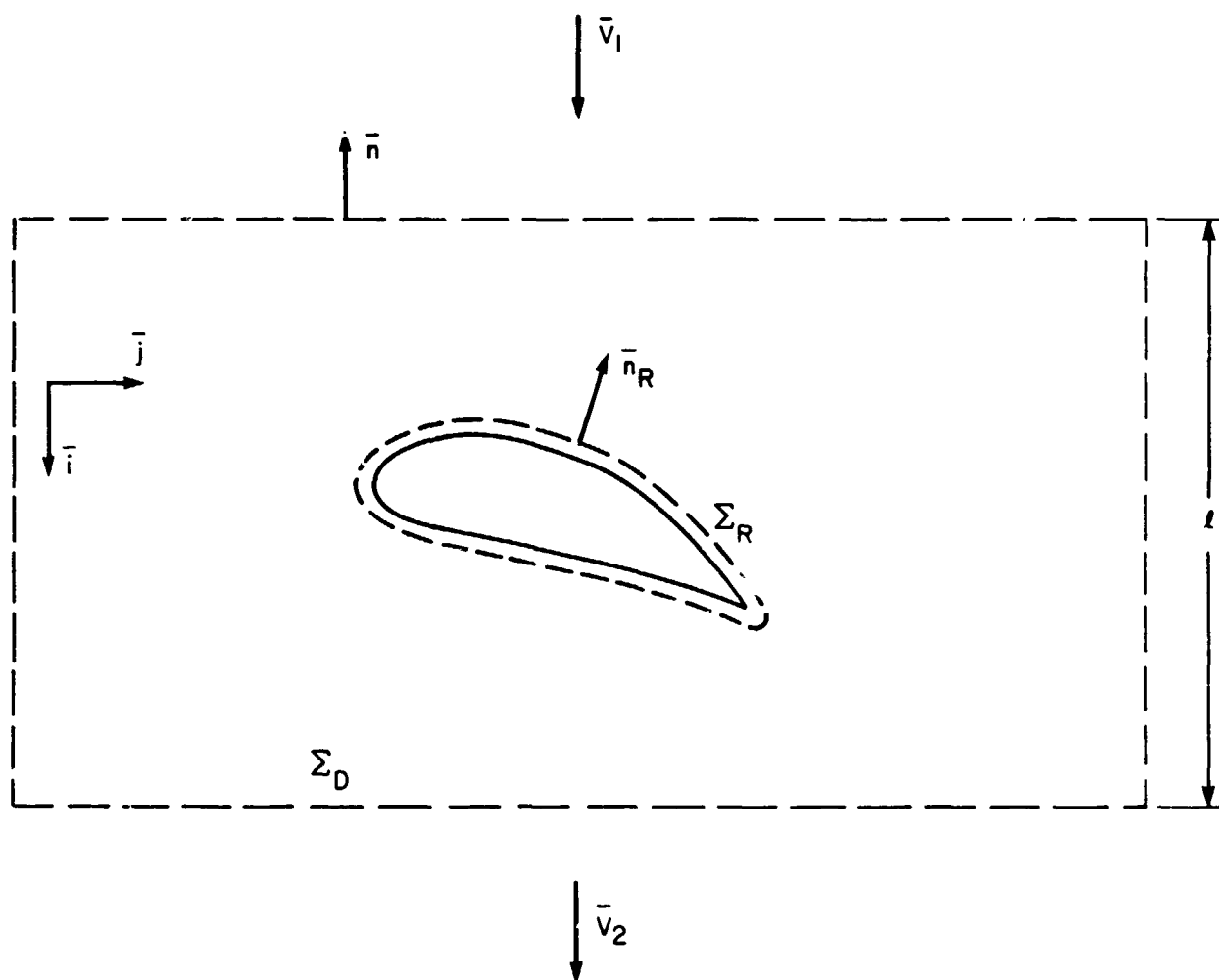


Figure C-1. Control Surfaces Σ_D and Σ_R for Momentum Theorem.

$$\begin{aligned} \oint_{\Sigma_D} p \bar{n} d\Sigma_D + \oint_{\Sigma_R} p \bar{n} d\Sigma_R \\ + \oint_{\Sigma_D} \rho \bar{V} (\bar{V} \cdot \bar{n}) d\Sigma_D = 0 \end{aligned} \quad (C-2)$$

The flux of momentum, \dot{m} , through the control surface is

$$\begin{aligned} \dot{m} &= \oint_{\Sigma_D} \rho \bar{V} (\bar{V} \cdot \bar{n}) d\Sigma_D \\ &= \iint \rho \left[(\bar{V} \cdot \bar{n})_1 \bar{V}_1 + (\bar{V} \cdot \bar{n})_2 \bar{V}_2 \right] d\Sigma \end{aligned} \quad (C-3)$$

Note that the continuity equation yields, in average,

$$(\bar{V} \cdot \bar{n})_1 = -(\bar{V} \cdot \bar{n})_2 \quad (C-4)$$

and noting that

$$\begin{aligned} \bar{n}_1 &= -\bar{i} \\ \bar{n}_2 &= \bar{i} \end{aligned} \quad (C-5)$$

one obtains

$$(\bar{V}_1 - \bar{V}_2) \cdot \bar{i} = 0 \quad (C-6)$$

Therefore, the flux through Σ_D can be written as

$$\dot{m} = - \iint \rho \bar{V}_1 \cdot \bar{i} (\bar{V}_1 - \bar{V}_2) d\Sigma_D \quad (C-7)$$

Let \vec{F} denote the force on the rotor

$$\vec{F} = - \oint_{\Sigma_R} p \vec{n} d\Sigma_R \quad (C-8)$$

Using Equation (C-8) in Equation (C-2) yields

$$\vec{F} = \iint (p_1 - p_2) i d\Sigma_D - \iint \rho \vec{V}_1 \cdot \vec{i} (\vec{V}_1 - \vec{V}_2) d\Sigma_D \quad (C-9)$$

The thrust perpendicular to the rotor tip path plane is, by applying Equation (C-6),

$$T = \iint_{\Sigma_D} (p_1 - p_2) d\Sigma_D \quad (C-10)$$

This is the desired expression which relates the forces acting on the rotor to the forces acting on the actuator disk.

The pressure is obtained from Bernoulli's equation

$$\frac{\partial \varphi}{\partial t} + \frac{p}{\rho} + \frac{1}{2} \nabla \varphi \cdot \nabla \varphi = \text{constant} \quad (C-11)$$

It is assumed that the radial velocity is negligible when compared with circumferential velocity and this yields

$$\begin{aligned} \frac{\partial \varphi}{\partial t} &= \frac{d\theta}{dt} \frac{\partial \varphi}{\partial \theta} \\ &= \Omega \frac{\partial \varphi}{\partial \theta} \end{aligned} \quad (C-12)$$

Equation (C-11) can be written as

$$P_1 - P_2 = -\rho \left(\frac{\partial (\varphi_1 - \varphi_2)}{\partial \theta} \Omega + |\nabla \varphi_1|^2 - |\nabla \varphi_2|^2 \right) \quad (C-13)$$

Combining Equations (C-10) and (C-13) and neglecting higher order terms in Equation (C-13), the thrust on the rotor becomes:

$$\begin{aligned} T &= -\rho \Omega \int_0^R \int_0^{2\pi} \frac{\partial (\varphi_1 - \varphi_2)}{\partial \theta} d\theta r dr \\ &= -\rho \Omega \int_0^R [\varphi_1 - \varphi_2]_0^{2\pi} r dr \end{aligned} \quad (C-14)$$

Note that

$$[\varphi_1 - \varphi_2]_0^{2\pi} = \left[\varphi_1 \right]_0^{2\pi} - \left[\varphi_2 \right]_0^{2\pi} = -\Delta \varphi_B \quad (C-15)$$

because the branch wake surface is on the lower surface of the disk.

Combining Equations (C-14) and (C-15),

$$T = \frac{1}{2} \rho \Omega R^2 \Delta \varphi_B \quad (C-16)$$

which is an expression which relates the discontinuity on the wake branch with the rotor thrust. In terms of the thrust coefficient, Equation (C-16) becomes

$$C_T = \frac{T}{\frac{1}{2} \rho \Omega^2 R^2 \pi R^2} = \frac{\Delta \varphi_B}{\pi \Omega R^2} \quad (C-17)$$

ORIGINAL PAGE IS
OF POOR QUALITY.

where

$\Delta \varphi_B$ = strength of branch wake

R = rotor radius

Ω = rotor speed